Diss. ETH No. 30449

The Bearingless Cross-Flow Fan for Lithography Excimer Lasers

A thesis submitted to attain the degree of

DOCTOR OF SCIENCES
(Dr. sc. ETH Zurich)

presented by

IVANA BAGARIC

MSc ETH
born on 16.06.1995

accepted on the recommendation of

Prof. Dr. Johann W. Kolar, examiner
Prof. Dr. Hans-Peter Nee, co-examiner

2024

Acknowledgments

Mayr and Alejandro Tejero Revelles for many supermarket snack trips, which kept me full and motivated.

A huge thank you goes to the PES team for creating an enthusiastic and engaging atmosphere at the institute, and for making every PES event so enjoyable. I had the great pleasure of supervising laboratory courses with Dr. Rosario Giuffrida, Dr. Pascal Niklaus, Dr. Reto Bonetti and Dr. Yunni Li as well as preparing the mechatronics exam with Dr. Marc Röthlisberger and Dr. Morris Heller - thank you for this enriching experience. A big thanks to Dr. Neha Nain and Dr. Gwendolin Rohner for every conversation and piece of advice, that has contributed to my confidence and growth as a female doctoral student.

Last but not least, I want to express my heartfelt gratitude to my family: my now-husband Adrian, my mom and dad, my sister Katarina, my brother Stipe and my baby nieces Maria and Diana. Your unconditional love and belief in me have been a constant source of strength and support, extending far beyond my doctoral journey. I am thankful to each of you for everything you have done and continue to do for me. *Sve ste mi.*

Hvala! Danke! Thank you!
Zurich, June 2024
Ivana Bagaric

Abstract

COMPONENTS in microelectronics are continually becoming smaller, a trend expected to persist into the future. This necessitates the advancement of fabrication methods, including state-of-the-art deep ultraviolet (DUV) lithography systems that etch features at the nanometer scale. DUV lithography systems commonly employ pulsed gas discharge excimer lasers as their light sources. The laser's pulse rate, the scanning speed of the lithography system, and consequently the chip throughput are constrained by several factors. Among these is the performance of the cross-flow fan (CFF), which is responsible for the continuous circulation of the excimer gas within the laser tube, since the gas in the discharge area between the electrodes must be replaced before the next laser pulse can be created.

State-of-the art CFFs are levitated and rotated inside the laser chamber using conventional magnetic bearings and an additional drive motor, offering advantages such as no lubricants, no friction and wear, and a hermetic encapsulation of the highly corrosive gases. However, these bearings come with several limitations such as requiring significant space and components, facing performance constraints and high torsional loads due to asymmetric drive torque generation, and involving complex air gap geometries and rotor encapsulations. These factors contribute to challenging and costly safety measures, as well as complicated maintenance and installation processes.

This doctoral thesis presents a bearingless CFF for this type of industrial application to address these limitations. The bearingless motor technology, which combines bearing force and drive torque generation in one unit, allows to create a compact, easy hermetically sealable, and conveniently maintainable drive system. By employing identical bearingless motors on both rotor sides, the CFF can achieve high rotational speeds with minimal torsional loads to enhance fluid dynamic performance and thereby increase the overall performance and throughput of such lithography system.

The objectives of this thesis include designing, analyzing and optimizing the bearingless CFF system to achieve high-speed and high-performance operation. This involves evaluating the rotor dynamics and fluid dynamics as well as assessing the impact on the magnetic bearing.

Several designs are investigated using numerical models and experimental measurements to explore the crucial trade-off between rotor dynamic aspects, such as mechanical strength and vibration modes, and fluid dynamic aspects, such as pressure and fluid flow. The lab-scale prototypes feature CFF blades measuring 600 mm in length and 60 mm in outer diameter, and are tested with air under ambient pressure.

A high-stiffness prototype is realized, resulting in stable operation up to 12 000 rpm with a maximum flow rate of ca. 1450 m^3/h and pressure increase of ca. 580 Pa, depending on the operating point. Furthermore, a prototype preferred from the fluid flow perspective is commissioned, reaching rotational speeds of up to 5500 rpm with a maximum fluid flow rate of ca. 1600 m^3/h and pressure increase of ca. 220 Pa . The excitation of the first bending resonance frequency emerges as the speed-limiting factor for both prototypes.

To overcome the performance limitations imposed by the bending resonance frequency, a novel decoupled bearingless CFF rotor capable of operating at supercritical speeds, i.e. beyond the first bending resonance frequency, is proposed. The novel rotor design includes mechanical decoupling elements that mitigate detrimental deformations and enable operation in the supercritical speed region, thereby increasing the maximum achievable rotational speed and fluid dynamic performance. It is demonstrated, that this approach allows the CFF to pass resonance frequencies without blade damage, enabling stable operation at 7000 rpm in the supercritical speed region due to the self-centering effect of the rotor. This represents a 40 % increase in rotational speed, resulting in a measured 28 % higher fluid flow and a 100 % higher static pressure increase compared to the CFF without decoupling elements.

To further increase the fluid dynamic performance of the bearingless CFF, this work conducts a CFD-based optimization of both rotor and static casing wall modifications, validated through various commissioned prototypes. It aims to enhance the mechanical stiffness of the rotor by integrating reinforcing shafts, shifting the speed-limiting bending resonance to a higher frequency, thus allowing for higher rotational speeds. Despite the highest achieved increase of rotational speed of 42 % through a stiffness-reinforcing central shaft, the fluid flow decreases by 61 % due to flow obstructions induced by the reinforcing shaft. For all tested stiffened prototypes, the loss in fluid flow outweighs the gain in rotational speed. Optimizing the casing walls to reduce fluid dynamic losses, however, resulted in a 22 % increase in maximum fluid flow, measuring 1800 m^3/h at 5000 rpm .

Overall, this thesis provides comprehensive analyses and optimizations of bearingless CFF designs, advancing the capabilities for high-speed, high-performance industrial applications. The findings contribute significantly to the understanding and development of next-generation bearingless CFFs.

Kurzfassung

BAUTEILE in der Mikroelektronik werden kontinuierlich kleiner, ein Trend, der voraussichtlich auch in Zukunft anhalten wird. Dies erfordert die Weiterentwicklung von Fertigungsmethoden, einschliesslich hochmoderner Deep-Ultraviolett-(DUV)-Lithographiesysteme, die Strukturen im Nanometerbereich ätzen. DUV-Lithographiesysteme verwenden üblicherweise gepulste Gasentladungsexcimerlaser als Lichtquellen. Die Pulsrate des Lasers, die Scangeschwindigkeit des Lithographiesystems und folglich der Chipdurchsatz werden durch mehrere Faktoren begrenzt. Einer dieser Faktoren ist die Leistung des Querstromlüfters (QSL), der für die kontinuierliche Zirkulation des Excimergases innerhalb der Laserkammer verantwortlich ist, da das Gas im Entladungsbereich zwischen den Elektroden vor dem nächsten Laserpuls ausgetauscht werden muss.

State-of-the-Art QSLs werden innerhalb der Laserkammer mittels konventioneller Magnetlager und einem zusätzlichen Antriebsmotor schwebend gelagert und rotiert, was Vorteile wie keine Schmierstoffe, keinen Verschleiss und eine hermetische Einkapselung der hochkorrosiven Gase bietet. Diese Lager haben jedoch mehrere Einschränkungen, wie erheblichen Platz- und Komponentenbedarf, Leistungseinschränkungen und hohe Torsionsbelastungen aufgrund asymmetrischer Drehmomenterzeugung sowie komplexe Luftspaltgeometrien und Rotoreinkapselungen. Diese Faktoren führen zu anspruchsvollen und kostspieligen Sicherheitsmassnahmen sowie zu komplizierten Wartungs- und Installationsprozessen.

Diese Dissertation stellt einen lagerlosen QSL für diese Art von Industrieanwendung vor, um die vorstehend genannten Einschränkungen zu überwinden. Die lagerlose Motortechnologie, welche Lagerkraft- und Antriebsmomenterzeugung in einer Einheit kombiniert, ermöglicht die Schaffung eines kompakten, leicht hermetisch versiegelbaren und einfach wartbaren Antriebssystems. Durch den Einsatz identischer lagerloser Motoren auf beiden Rotorseiten kann der QSL hohe Drehzahlen bei minimalen Torsionsbelastungen erreichen, was die strömungsdynamische Leistung verbessert und somit die Gesamtleistung und den Durchsatz eines solchen Lithographiesystems erhöht.

Die Ziele dieser Arbeit umfassen das Entwerfen, Analysieren und Optimieren des lagerlosen QSL-Systems, um einen Hochgeschwindigkeits- und Hochleistungsbetrieb zu erreichen. Dies beinhaltet die Bewertung der Rotordynamik und Strömungsdynamik sowie die Untersuchung der Auswirkungen auf das Magnetlager.

Mehrere Designs werden mithilfe numerischer Modelle und experimenteller Messungen untersucht, um den entscheidenden Kompromiss zwischen rotordynamischen Aspekten wie mechanischer Festigkeit und Schwingungsmodi sowie strömungsdynamischen Aspekten wie Druck und Durchfluss zu erforschen. Die Laboraufbauten der Prototypen haben QSL-Schaufeln mit einer Länge von 600 mm und einem Aussendurchmesser von 60 mm und werden mit Luft unter Umgebungsbedingungen getestet.

Ein Prototyp mit hoher Steifigkeit wird realisiert, der einen stabilen Betrieb bis zu 12 000 rpm mit einer maximalen Durchflussrate von ca. 1450 m^3/h und einem Druckanstieg von ca. 580 Pa, je nach Betriebspunkt, ermöglicht. Darüber hinaus wird ein aus strömungstechnischer Sicht bevorzugter Prototyp in Betrieb genommen, der Drehzahlen von bis zu 5500 rpm mit einer maximalen Durchflussrate von ca. 1600 m^3/h und einem Druckanstieg von ca. 220 Pa erreicht. Die Anregung der ersten Biegeeigenfrequenz erweist sich als geschwindigkeitsbegrenzender Faktor für beide Prototypen.

Um die durch die Biegeresonanzfrequenz auferlegten Leistungsbeschränkungen zu überwinden, wird ein neuartiger entkoppelter lagerloser QSL-Rotor vorgeschlagen, der in der Lage ist, bei überkritischen Geschwindigkeiten zu arbeiten. Das neuartige Rotordesign umfasst mechanische Entkopplungselemente, die schädliche Verformungen abmildern und den Betrieb im überkritischen Geschwindigkeitsbereich ermöglichen, wodurch die maximal erreichbare Drehzahl und die strömungsdynamische Leistung erhöht werden. Es wird gezeigt, dass dieser Ansatz ermöglicht, Resonanzfrequenzen ohne Schaufelschäden zu passieren und einen stabilen Betrieb bei 7000 rpm im überkritischen Geschwindigkeitsbereich durch den selbstzentrierenden Effekt des Rotors zu gewährleisten. Dies stellt eine Erhöhung der Drehzahl um 40 % dar, was zu einem gemessenen 28 % höheren Durchfluss und einem 100 % höheren Druckanstieg im Vergleich zum QSL ohne Entkopplungselemente führt.

Um die strömungsdynamische Leistung des lagerlosen QSL weiter zu erhöhen, wird eine CFD-basierte Optimierung sowohl der Rotor- als auch der statischen Gehäusewandmodifikationen durchgeführt, die durch verschiedene in Betrieb genommene Prototypen validiert wird. Ziel ist es, die mechanische Steifigkeit des Rotors durch die Integration von Verstärkungsschäften zu erhöhen, um die geschwindigkeitsbegrenzende Biegeresonanzfrequenz zu einer höheren Frequenz zu verschieben und somit höhere Drehzahlen zu ermöglichen. Trotz der höchsten erreichten Drehzahlerhöhung von 42 % durch einen steifigkeitsverstärkenden Zentralschaft, verringert sich der Durchfluss aufgrund von Strömungshindernissen, die durch den Verstärkungsschaft

verursacht werden, um 61 %. Bei allen getesteten verstärkten Prototypen überwiegt der Verlust an Durchfluss den Gewinn an Drehzahl. Die Optimierung der Gehäusewände zur Reduzierung strömungsdynamischer Verluste führt jedoch zu einer 22 %-igen Erhöhung des maximalen Durchflusses, wobei bei 5000 rpm 1800 m^3/h erreicht werden.

Insgesamt bietet diese Dissertation umfassende Analysen und Optimierungen von lagerlosen QSL-Designs, welche die Leistungsfähigkeit für Hochgeschwindigkeits- und Hochleistungsanwendungen in der Industrie vorantreiben. Die Ergebnisse tragen wesentlich zum Verständnis und zur Entwicklung von lagerlosen QSL der nächsten Generation bei.

Contents

1
Introduction

THE trend of increasing functionality while shrinking the feature size of advanced integrated circuits, as predicted by Moore's Law [1], requires ongoing miniaturization of components in microelectronics. This in turn drives the need for increasingly sophisticated fabrication methods such as improved lithography tools. Highly specialized laser modules, such as short-wavelength deep ultraviolet (DUV) lithography systems, are used to create nanometer-scale features [2–5]. Meeting the technical and economic requirements of fast large-scale production, is closely tied to the performance of these laser modules determined by their power input, repetition rates but also their reliability. The main microlithography requirements are summarized in **Tab. 1.1** in terms of industry requirements, technology demands and the resulting specifications of the laser module [6–10].

Tab. 1.1: Microlithography requirements.

Industry requirement	Technology demand	Laser specification
Higher resolution	Shorter wavelength	248 nm (KrF) - 193 nm (ArF)
	Higher numerical apertures	Narrow spectral bandwidth Wavelength stability
Higher throughput	Faster scan speed	High repetition rate High average laser power Good energy dose control
High yield	Tight process control	Stability of laser parameters On-board metrology
Reduced running cost	Maintenance	Maintainability
	Long lifetime	Long module lifetime
	High uptime	High reliability

Argon fluoride (ArF) or krypton fluoride (KrF) excimer lasers are typically used as the DUV lithography light source [11–15]. The main components of the excimer laser chamber are the electrodes for the electrical discharge, heat exchangers to remove excess heat from the conversion between electrical input power and optical output power, and a cross-flow fan (CFF) with a diameter of up to 150 mm and a length of up to 1500 mm [8, 16–19]. The primary task of the CFF is the forced circulation of the laser gas over the entire length of the electrodes. This circulation allows for the continuous renewal of the laser gas between the electrodes, removes unwanted discharge products, and maintains a high flow rate through the heat exchangers required for the high frequency pulsed laser operation [7, 8, 20]. Due to the highly corrosive and toxic nature of excimer gases, particularly fluorine, it is crucial that the system is absolutely hermetically sealed. Since the gas mixture in the discharge region between the electrodes must be replaced before the next laser pulse can be generated, the maximum achievable repetition rate, and thus, the laser's throughput, depends directly on the flow rate generated by the CFF [21]. This relationship is described by the flow-clearing ratio, C:

$$C = \frac{v}{w \cdot f} \tag{1.1}$$

where v is the gas flow velocity between electrodes, w is the discharge width of the electrodes, and f is the repetition rate of the laser [7, 22]. Clearing ratios of

$$C_{\min} > 2 - 3 \tag{1.2}$$

are required to enable the successful generation of the next laser pulse [7, 8]. The throughput P_{out} is then calculated from the energy per pulse E_{pulse} and the repetition rate f as

$$P_{\text{out}} = E_{\text{pulse}} \cdot f. \tag{1.3}$$

Hence, the throughput, and thus the scanning speed of the system, is, among other factors, limited by the performance of the CFF contained in the laser [6, 23].

The state-of-the-art in this type of DUV excimer laser is the implementation of magnetically supported CFFs. The pioneering patent for a CFF active magnetic bearing system in excimer lasers dates back to 1997 [24], aiming to increase the pulse repetition rate of gas discharge lasers by achieving higher fan speeds through magnetic bearings and more powerful motors, thereby replacing the previously used mechanical ball bearings. The introduction of magnetic bearings has brought several advantages. Magnetic bearings

extend the operational lifespan of the bearings, require less maintenance and by eliminating the presence of lubrication, significantly reduce potential contamination sources. Additionally, active control of the rotor position via magnetic bearings helps manage and eliminate certain vibration modes and enables to operate CFFs in a periodically cycled mode when necessary, to improve gas mixing within the laser chamber. Ultimately, magnetic bearings allow to operate the CFF at higher rotational speeds. Several patents for active magnetic CFF bearing systems in excimer lasers followed [25–29].

Despite these advantages, conventional magnetic bearing systems for excimer lasers still face certain limitations:

▶ *High space and component requirements*: at least two radial bearings and one axial bearing are required to fully stabilize the rotor, alongside a motor to generate the drive torque (see **Fig. 1.1 (a)**).

▶ *Performance constraints*: the one-sided drive torque generation limits the performance and leads to high torsional loads, reducing the lifespan of the fan system. The risk of torsional vibrations exacerbates this issue.

▶ *Design and safety limitations*: the complex air gap geometry and rotor encapsulation (highlighted in **Fig. 1.1 (a)**) limit design compactness and safety and make installations and maintenance of these systems very inconvenient.

This dissertation proposes and investigates a bearingless CFF for the presented excimer laser application, aimed at overcoming the state-of-the-art limitations. With bearingless motors as shown in **Fig. 1.1 (b)**, the drive and magnetic bearing are integrated into one compact unit, which maximizes the air gap, thereby allowing for a simple hermetic sealing structure and better insulation [30–34]. This design reduces space requirements compared to conventional magnetic bearings, now replaced by two compact bearingless motors. Furthermore, drive torque is available on both CFF rotor sides, without requiring additional space or components. By that, high drive power for enhanced speed and performance is available, at minimal torsional loads and torsional vibrations. The bearingless CFF concept allows for a highly compact, hermetically sealed placement of the motors outside the laser chamber. This contributes to improving the safety standard, simplifying new installations and reducing costly maintenance work, and increasing the lifetime of the gas circulation system in an excimer laser.

(a)

Motor Radial magnetic bearing Axial magnetic bearing

one-sided drive torque generation *complex airgap geometry & encapsulation* *poorly exchange-able unit* *complex airgap geometry & encapsulation*

(b)

simple sealing structure

easily exchange-able unit

Bearingless motor 1 Bearingless motor 2
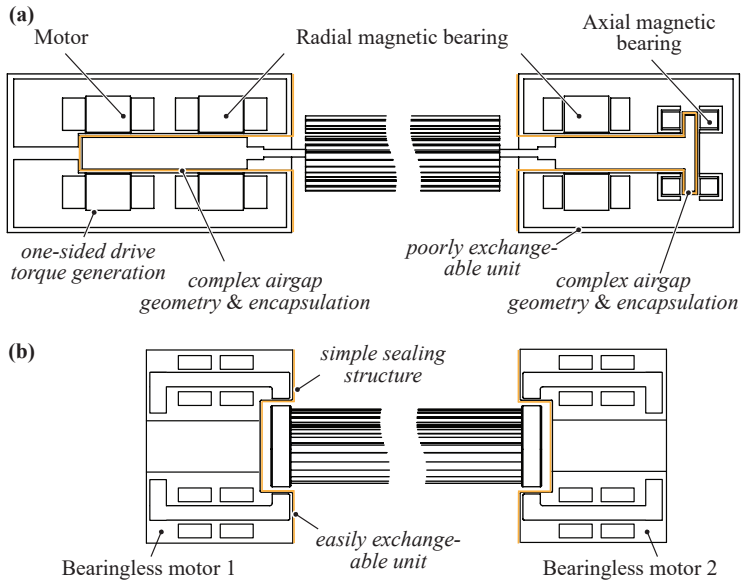
Fig. 1.1: CFF levitated and rotated (**a**) by a magnetic bearing system including two radial magnetic bearings, one axial magnetic bearing, and a drive system [24] and (**b**) by two bearingless motors.

1.1 Challenges

The implementation of a bearingless CFF comes with a number of challenges across various aspects of the mechatronic system, as summarized in the following list:

▶ *Bearingless motor - coupling*: to achieve both levitation and rotation of the CFF blades, a sophisticated control structure is required to enable two bearingless motors to synchronously control the shared CFF rotor.

▶ *Bearingless motor - drive power*: to achieve the desired high-speed and high-performance CFF operation necessitates substantial driving power. It has to be contributed by both bearingless motors simultaneously, to minimize torsional loads to the CFF rotor.

▶ *Bearingless motor - magnetic bearing*: ensuring stable levitation and precise control of the rotor position in both bearingless motors is essential.

This is particularly challenging as the magnetic bearing must withstand rotor dynamic and fluid dynamic forces under varying operational conditions.

▶ *Rotor design*: the CFF blades must be engineered to withstand high-speed operation without incurring structural damage while simultaneously meeting stringent fluid dynamic requirements. This includes ensuring optimal airflow and pressure characteristics to maintain performance efficiency.

▶ *Rotor dynamics*: the CFF must be designed to avoid natural frequencies that could resonate with operational speeds, causing excessive vibrations and possible structural failure. The first bending resonance frequency is particularly critical in this regard.

▶ *Fluid dynamics*: the fluid dynamic performance of the CFF must be optimized through careful design of the CFF blades and static casing walls. Currently, there is no general approach or analytical model to accurately describe the aerodynamic characteristics and loss mechanisms of CFFs, nor to precisely predict their performance. Therefore, numerical methods are required for design and optimization.

▶ *Multidisciplinary approach*: the design and optimization of each aspect of the bearingless CFF are highly interdependent. Trade-offs are inevitable, since design aspects, i.e. favorable from a fluid dynamics point of view may not be favorable from a rotor dynamics design standpoint.

1.2 Aims and Contributions

The aim of this thesis is to introduce the concept of a bearingless cross-flow fan, and to analyze and optimize it with regard to bearingless motor drive and bearing functionality, as well as rotor and fluid dynamic performance, for the proposed industrial application. A summary of the most relevant contributions is provided in the following list:

▶ The bearingless CFF is implemented for the first time in this research project. The proposed system enables the levitation of the CFF rotor using two bearingless motors, each with an independent bearing force control structure. Additionally, it allows for the CFF rotation where each motor contributes half of the required drive torque, evenly distributing the load.

▶ A novel bearingless CFF rotor is presented that operates above its critical bending resonance frequency, i.e. at supercritical operation. This shifts the next speed-limiting resonance to higher frequencies, allowing the CFF to operate at increased rotational speeds and thereby enhancing its fluid dynamic performance.

▶ Several measures are proposed to increase the CFF's mechanical stiffness, enabling its operation at higher rotational speeds. These measures include evaluating the manufacturability of the CFF and exploring various configurations of reinforcing mechanical shafts.

▶ The trade-off between stiffness increasing measures and the resulting influence on fluid dynamic behavior is studied by means of numerical simulations and experimental measurements. This results in several different prototypes aimed for the high-speed and high-performance operation of CFFs.

▶ Design optimizations for the CFF static casting walls are proposed, resulting in increased CFF fluid dynamic performance without altering the rotor or the bearingless motor. These insights can be applied to CFFs beyond the proposed application.

1.3   List of Publications

Key insights presented in this thesis have already been published in international scientific journals, conference proceedings, or presented at workshops. The publications created as part of this thesis are listed below.

1.3.1   Journal Papers

▶ I. Bagaric, D. Steinert, T. Nussbaumer and J. W. Kolar, "CFD Based Optimization of High-Speed and High-Performance Bearingless Cross-Flow Fan Designs," *Machines*, vol. 12(8), no. 513, July 2024. DOI: 10.3390/machines12080513

▶ I. Bagaric, D. Steinert, T. Nussbaumer and J. W. Kolar, "Supercritical Operation of Bearingless Cross-Flow Fan," *Machines*, vol. 12(4), no. 223, March 2024. DOI: 10.3390/machines12040223

▶ I. Bagaric, R. Hu, D. Steinert, T. Nussbaumer and J. W. Kolar, "Comparative Evaluation of High-Speed Bearingless Cross-Flow Fan Designs

for Lithography Excimer Lasers," *Machines*, vol. 11(6), no. 611, June 2023. DOI: 10.3390/machines11060611.

1.3.2 Conference Papers

▶ I. Bagaric, D. Steinert, T. Nussbaumer and J. W. Kolar, "Concept of a Novel Bearingless Three-Pole Motor for Two-Sided Driven Applications," in *Proc. of the 24th International Conference on Electrical Machines and Systems (ICEMS)*, Gyeongju (virtual), Korea, October 2021. DOI: 10.23919/ICEMS52562.2021.9634649.

▶ I. Bagaric, D. Steinert, F. Wassmer, T. Holenstein, T. Nussbaumer and J. W. Kolar, "Design and Characterization of a Bearingless Cross-Flow Fan," in *Proc. of the IEEE/ASME International Conference on Advanced Intelligent Mechatronics (AIM)*, Delft (virtual), Netherlands, July 2021. DOI: 10.1109/AIM46487.2021.9517520.

1.4 Thesis Outline

According to the goals and contributions mentioned above, the content of the thesis is divided into three main chapters and conclusions. All the chapters can be read independently since the interdependencies have been reduced to the strict minimum.

▶ **Chapter 2** introduces the bearingless CFF and analyses the motor's operating principle in terms of the generation of bearing forces and drive torque. Two rotor prototypes are presented, addressing the trade-offs and intricate interactions among mechanical strength, manufacturability, rotor dynamics, and fluid dynamic performance. The impact on magnetic bearings and the limitations related to maximum achievable speed are thoroughly investigated. The methods presented include analytical descriptions as well as a FEM-based modal analysis of the system's dynamic behavior, development and validation of a Computational Fluid Dynamics (CFD) model, and the setup of a test rig for conducting experimental measurements. The bending resonance frequency emerges as the speed-limiting factor for the position control of the bearingless motor as well as the CFF blades from a structural perspective.

▶ **Chapter 3** presents a novel CFF rotor design. The design incorporates additional mechanical elements with low mechanical stiffness between

the CFF blades and rotor magnets (required for the magnetic bearing). This allows the rotor to pass the first bending resonance frequency without structural damage of the CFF blades, enabling supercritical speed operation. The influence of the decoupling elements' stiffness is thoroughly investigated by means of a mass-spring-damper (*mkd*-) model and several commissioned prototypes with different decoupling elements. The influence on the magnetic bearing is analyzed and the self-centering effect of the rotor above the first bending resonance frequency experimentally demonstrated. This CFF design approach shifts the blade-damaging resonance to higher frequencies, allowing for higher rotational speeds and thus higher fluid dynamic performance.

▶ **Chapter 4** conducts a CFD based optimization of the CFF rotor and static casing walls to enhance the fluid dynamic performance of bearingless CFFs. The investigation explores design measures to increase the mechanical strength of the CFF by introducing stiffness-enhancing shafts, thereby shifting the critical bending resonance to higher frequencies. Additionally, design adaptations of the static casing walls are evaluated to reduce fluid dynamic losses, with a focus on the fundamental aerodynamics of the CFF. Higher rotational speeds are achieved with stiffness-increasing shafts, but this comes at the expense of fluid dynamic performance. Consequently, the loss in fluid dynamic performance outweighs the benefits of increased rotational speed. However, an optimized static casing wall structure is proposed, resulting in enhanced fluid dynamic performance, without altering the CFF rotor or the bearingless motor.

▶ **Chapter 5** concludes the thesis by recapitulating the results and contributions and putting them in perspective with an outlook on future work.

▶ Preliminary studies are conducted on the fundamental operating principle of the novel bearingless cross-flow fan. **Appendix A** presents the results on the design and characterization of a first bearingless cross-flow fan demo prototype. **Appendix B** presents the results of a theoretical investigation on a novel bearingless ultra-compact three-pole motor topology for two-sided driven applications.

2

Comparative Evaluation of High-Speed Bearingless Cross-Flow Fan Designs for Lithography Excimer Lasers

This chapters summarizes the most relevant findings regarding the concept, design and realizations of two bearingless high-speed cross-flow fan designs, as also published in:

▶ I. Bagaric, R. Hu, D. Steinert, T. Nussbaumer and J. W. Kolar, "Comparative Evaluation of High-Speed Bearingless Cross-Flow Fan Designs for Lithography Excimer Lasers," *Machines*, vol. 11(6), no. 611, June 2023.

┌─ **Chapter Abstract** ─────────────────────────

This chapter conducts a comparative evaluation of two bearingless cross-flow fan designs. With identical bearingless motors on both rotor sides, it is possible to drive the cross-flow fan symmetrically to high rotational speeds at low torsional loads. The rotor prototypes were optimized, analyzed, and pushed to high-speed operation and evaluated with respect to their rotor dynamic and fluid dynamic performance using finite element methods and experimental measurements. For both prototypes, successful numerical studies were performed, where a modal analysis enabled theoretical predictions of expected resonance frequencies, and a CFD analysis visualized local flow effects and provided cross-flow fan design comparisons. A stable operation of up to 12 000 rpm and 5500 rpm was accomplished for the two elaborated designs.

2.1 Introduction

Components in microelectronics have been becoming increasingly smaller, and this trend will continue in the future. Complex fabrication methods are needed to meet the evolving requirements of current state-of-the-art microchips. **Fig. 2.1 (a)** shows a schematic of a deep ultraviolet (DUV) lithography system used to burn in nanometer-scale features, that typically contains an ArF or KrF excimer laser as its light source [13]. The throughput of these lasers, and thus the scanning speed of the system, is, among other factors, limited by the performance of the cross-flow fan (CFF) contained in the laser [6, 7, 16, 17, 23]. This chapter conducts a comparative evaluation of bearingless CFF designs for such applications. Two designs are analyzed in terms of rotor dynamic and fluid dynamic performance using finite element methods (FEM) and experimental measurements and pushed to high-speed operation.

The cross-section of such a laser is shown in **Fig. 2.1 (b)**, where the main components are electrodes for the electrical discharge, heat exchangers to remove excess heat, and the CFF. The main task of the CFF is the continuous renewal of the laser gas between the electrodes. Since the gas mixture in the discharge region has to be replaced before the next laser pulse can be generated, the maximum achievable repetition rate, and thus, the throughput of the laser, depends directly on the flow rate generated by the cross-flow fan [7]. High repetition rates f at moderate pulse energies E_{pulse} are demanded, resulting in high scan speeds, good energy stability, and compact designs [13]. Increasing the repetition rate leads to further improvements in these properties, which can be accomplished by increasing the CFF's rotational speed, thereby increasing the flow velocity. This means that a high-speed CFF is a direct enabler of improved laser performance. The microelectronics industry, technology, and laser requirements are summarized in **Fig. 2.1 (c)**.

The bearingless CFF concept was first presented by the authors in [35] for a conceptual prototype up to 3500 rpm. The challenges in implementing a bearingless high-speed and high-performance CFF lie particularly in the rotor and fluid dynamic behavior, the influence on the magnetic bearing, and the high power demand for the driving motors. The rotor has to be mechanically designed for high speeds and high flows simultaneously, while the magnetic bearing has to be able to withstand these forces. The goal of this chapter is to design, optimize, and analyze two prototypes and to push them to high rotational speeds. The rotor designs shall be evaluated in terms of rotor and fluid dynamic behavior by means of FEM simulations and experimental measurements within a constructed test rig.

(a)

Rear optics module

Pulse power module (PPM)

Excimer laser tube

Front optics module

Proposed bearingless motors

Support modules (water and gas), gas pressure & flow meters, power supply etc.

Control cabinet

(b)

Electrodes

PPM

$$C = \frac{v}{w \cdot f}$$

C: flow clearing ratio
v: gas flow velocity
w: discharge width
f: repetition rate

Cross flow fan (CFF)

Heat exchanger

(c)

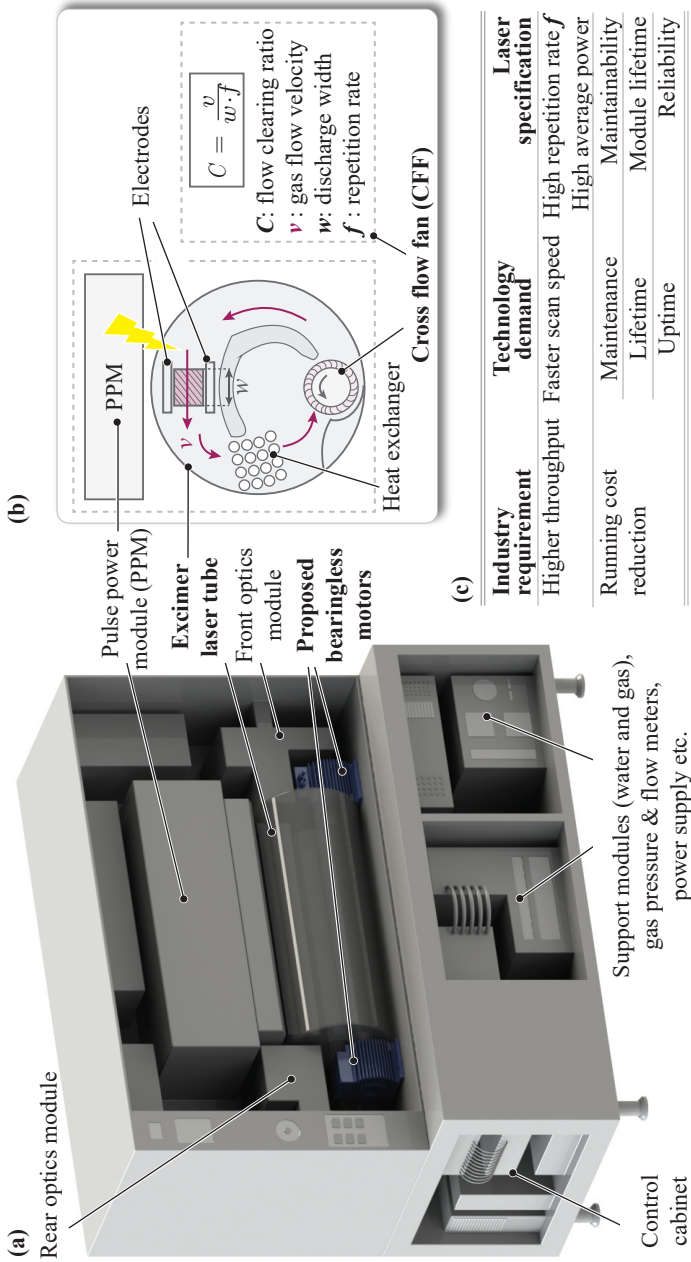| Industry requirement	Technology demand	Laser specification
Higher throughput	Faster scan speed	High repetition rate f
		High average power
Running cost reduction	Maintenance	Maintainability
	Lifetime	Module lifetime
	Uptime	Reliability

Fig. 2.1: **(a)** Conceptual drawing of a deep ultraviolet (DUV) lithography system with an ArF or KrF excimer laser as the light source. **(b)** Cross-section of an excimer laser chamber with the electrodes, heat exchangers, and the CFF as its main components. **(c)** Summary of key industry requirements, technology demands, and laser specification.

In **Sec. 2.2**, the bearingless motor and its operating principle are described. Subsequently, two rotor prototypes, where one is a single-body aluminum rotor with straight fan blades and the other is a multi-body stainless-steel rotor with curved fan blades, are presented in **Sec. 2.3** and are compared in **Sec. 2.4** with respect to their rotor dynamic behaviours. A detailed numerical study of the fluid dynamic aspects of both rotors follows in **Sec. 2.5**. Finally, the designed test rig and the experimental results are presented in **Sec. 2.6**.

2.2   Bearingless Motor Topology

The bearingless motor topology proposed for the high-speed and high-performance CFF application is illustrated in **Fig. 2.2 (a)**. Magnetic bearing and drive forces are transmitted via a common iron circuit to the rotor, which features a one-pole-pair permanent magnet on each side. Due to this so-called temple design, the magnetic field is generated outside the rotor planes, resulting in a very compact shape of the motor. The simple air gap geometry enables a conveniently maintainable, compact, and hermetically sealed implementation of the drives outside the laser chamber. The presented concept with bearingless motors used on both sides is also characterized by the high power available and low torsional load on the cross-flow fan blades. The most important motor data are summarized in **Fig. 2.2 (b)**.

The operating principle of the bearingless motor can be explained with **Fig. 2.2 (c),(d)** and is described in detail in [36]. By applying equal currents (in magnitude and sign) to opposite bearing coils (see **Fig. 2.2 (d)**), a two-pole-pair stator field is created, which, together with the rotor field, generates radial forces. By applying currents to opposite drive coils with the same magnitude but opposite sign, a single-pole-pair stator field is generated, which is 90° ahead of the rotor field. These tangential forces create a rotor torque. Stabilization in the axial z-direction is achieved by passive reluctance forces between the magnet and the surrounding iron yoke; hence, no additional axial bearing is necessary.

Fig. 2.2 (c) shows how the control of a common CFF rotor via two bearingless motors has been implemented. Bearingless motor (BM) 1 and BM2 control the bearing forces independently using a cascaded PID control structure. The torque is generated by both motors by passing a reference torque current from BM1 ("primary") to BM2 ("secondary"), i.e., each motor contributes half of the required drive torque, such that the load is evenly distributed. The control of the drive phase currents is handled by each motor separately using its own angular sensor system. The speed control is handled by BM1 through

Description	Value
AC voltage	$200 - 240\,\text{V}_{\text{rms}}$
Power input	$2\,\text{kW}$
Speed range	$\pm 15\,\text{krpm}$
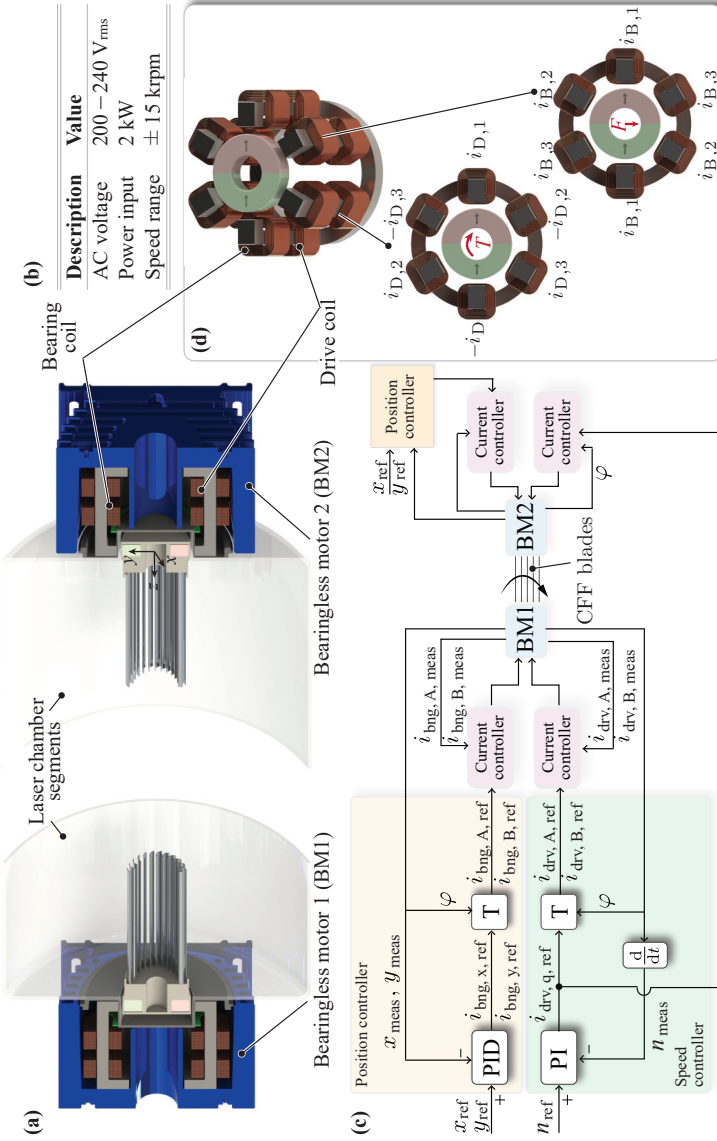
Fig. 2.2: **(a)** Schematic cross-section of the bearingless CFF system in a DUV laser chamber. **(b)** Key parameters of the motor. **(c)** Control concept of the bearingless drives, where motor 1 (BM1) and motor 2 (BM2) control the bearing forces individually. Both bearingless motors receive a reference drive torque current from a single speed controller, which is implemented here in the "primary" motor BM1. Thereby, each motor generates half of the required drive torque, and the load is evenly distributed among BM1 and BM2s since they share a common rotor. Each motor handles the control of the drive phase currents separately, using its own angular sensor system. **(d)** Required coil currents for bearing force and drive torque creation. By applying equal currents (in magnitude and sign) to opposite bearing coils, radial forces are created. By applying currents to opposite drive coils with the same magnitude but opposite sign, tangential forces are generated, resulting in rotor torque.

13

a PI controller. This means that high drive forces are available on both rotor sides, which massively reduces torsional loads on the rotor.

For the intended high-speed application, the bearingless CFF system presented here is an ultra-compact, conveniently exchangeable and maintainable, and safe option designed for high performance.

2.3   High-Speed Rotor Prototypes

The goal of this chapter is firstly to select CFF rotor designs that allow high rotational speeds due to their high mechanical strength, that are manufacturable, and that generate high flow rates and to then investigate them by means of FEM simulations and experimental measurements. The focus lies on the rotor dynamic and fluid dynamic behavior. The challenge is to find a trade-off between mechanical strength and fluid performance since, on the one hand, designs that increase strength come at the expense of fluid inlet area or disrupt the flow through the fan, resulting in a reduction in fluid performance. On the other hand, thin fan blades allow for high fluid performance, but from a mechanical point of view, they limit the achievable rotational speed.

The two chosen prototypes are shown in **Fig. 2.3**, and their main mechanical characteristics are summarized in **Tab. 3.3**. Prototype 1 (PT1) is a CFF rotor milled from a full cylinder of aluminum, which is mechanically robust and stiff. To limit the manufacturing complexity, the blade surface geometry is kept straight, and the thickness of the individual blades is relatively high at 1.4 mm, to the disadvantage of the fluid inlet area.

Tab. 2.1: Table with key parameters of the investigated CFF prototypes.

	Prototype 1	Prototype 2
Material	Aluminum	Stainless steel
Mass of CFF blades	890 g	740 g
Total length L_{tot}	680 mm	680 mm
Fluid inlet length L_{fluid}	400 mm	590 mm
Outer diameter d_o	60 mm	60 mm
Inner diameter d_i	44 mm	44 mm
Cross-sectional blade profile	Straight	Curved
Blade thickness	1.4 mm	0.5 mm
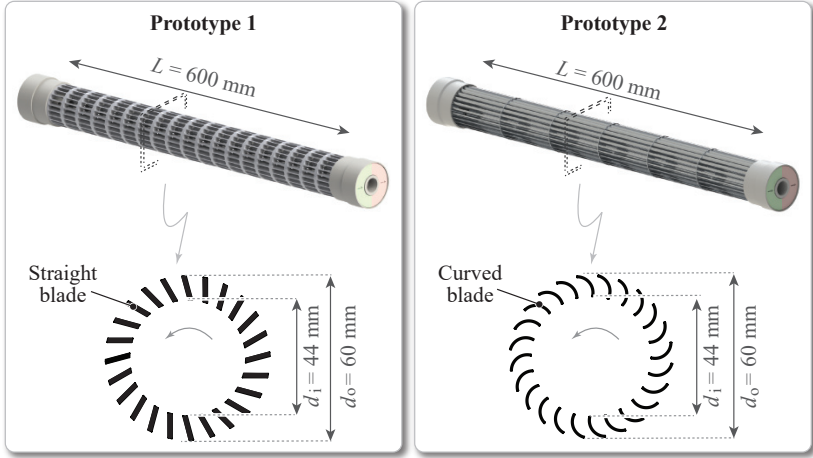
Fig. 2.3: Renderings of the investigated prototypes (PTs). Single-body PT1 consists of 1.4 mm thick, straight aluminum blades, and the multi-body PT2 consists of 0.5 mm thin, curved, stainless-steel blades.

Having the same external dimensions, Prototype 2 (PT2) consists of individual 0.5 mm thin, curved, stainless-steel blades connected to separation plates. While this design is advantageous for fluid performance, its mechanical stiffness is heavily reduced, and some uncertainty occurs when modeling the multi-body fan.

The selected PTs with respect to high-speed and high-performance applications were evaluated through simulations and experiments and compared in terms of their rotor dynamic and fluid dynamic behavior. The applied methods are described in detail in the next sections.

2.4 Rotor Dynamical Analysis

The rotor dynamic behavior of the system was investigated to achieve the desired CFF speed range since the magnetic bearing can only handle forces and allow displacements to a limited extent. The aim was to design a rotor that is mechanically robust for high speeds and whose destabilizing dynamic forces can be controlled by the magnetic bearing.

2.4.1 Analytical Description

The Jeffcott rotor model was used for the mathematical description and explanation of important rotor dynamic effects. This model of rotor dynamics can be extended from a rigid, mechanically supported system to a two-sided, magnetically levitated elastic rotor. For the investigated case of a two-sided, magnetically levitated elastic CFF, the model of the Jeffcott rotor shown in **Fig. 2.4 (b)** was used, which is explained in more detail in [37]. The model consists of a disc with mass m_R and mass eccentricity ϵ, two magnets in the magnetic bearing (MB) with mass m_B, and a massless shaft with bending stiffness k_{shaft}. If the magnets in the MB are attributed their own degrees of freedom $w_R(t)$ and $w_B(t)$ and the magnetic bearing is assumed to be rotationally symmetrical, then the radial displacement of the bearing magnets $r_B(t)$ and radial displacement of the geometric disc center $r_R(t)$ can be expressed in a complex manner, as follows:

$$\begin{aligned} r_R(t) &= w_R(t) + jv_R(t) \\ r_B(t) &= w_B(t) + jv_B(t). \end{aligned}$$

(2.1)

This relationship is illustrated in **Fig. 2.4 (a)**. The following equations of motion are obtained for this system:

$$\mathbf{M}\begin{Bmatrix} \ddot{r}_R \\ \ddot{r}_B \end{Bmatrix} + \mathbf{D}\begin{Bmatrix} \dot{r}_R \\ \dot{r}_B \end{Bmatrix} + \mathbf{K}\begin{Bmatrix} r_R \\ r_B \end{Bmatrix} = \epsilon m_R \Omega^2 \begin{Bmatrix} e^{j\Omega t} \\ 0 \end{Bmatrix}.$$

(2.2)

The mass matrix $\mathbf{M}$ is composed of the disc mass m_R and the two magnet masses m_B according to

$$\mathbf{M} = \begin{bmatrix} m_R & 0 \\ 0 & 2 \cdot m_B \end{bmatrix}.$$

(2.3)

The damping

$$\mathbf{D} = \begin{bmatrix} 0 & 0 \\ 0 & 2 \cdot D \cdot k_i \end{bmatrix}$$

(2.4)

and stiffness matrices

$$\mathbf{K} = \begin{bmatrix} k_{shaft} & -k_{shaft} \\ -k_{shaft} & k_{shaft} + 2(P \cdot k_i - k_s) \end{bmatrix}$$

(2.5)

include the PD control parameters of the active magnetic bearing with position-proportional feedback (P-element)

$$P = \frac{k_{bng} + k_s}{k_i}$$

(2.6)

and velocity-proportional feedback (D-element)

$$D = \frac{d}{k_i}. \tag{2.7}$$

The parameters P and D are determined by setting appropriate values for stiffness k and damping d of the closed-loop system [38]. Moreover, the radial bearing stiffness (force/displacement factor) is represented by k_s, and the active bearing force constant (force/current factor) is represented by k_i. Introducing the abbreviations:

$$
\begin{aligned}
v &= m_B/m_R & &\text{mass of bearing magnet/mass of disc,} \\
a = k_{bng}/k_{shaft} &= 2(P \cdot k_i - k_s)/k_{shaft} & &\text{relation between magnetic bearing,} \\
& & &k_{bng} \text{ and elastic shaft stiffness } k_{shaft}, \\
b &= 2 \cdot D \cdot k_i/m_R \cdot \omega_{Jeffcott} & &\text{related damping,} \\
\omega_{Jeffcott} &= \sqrt{k_{shaft}/m_R} & &\text{reference frequency,}
\end{aligned}
\tag{2.8}
$$

the eigenvalues of the homogeneous solution of the differential equation, **Eq. (3.3)**, can be calculated as a function of the stiffness ratio a. The detailed derivation can be found in [37]. The most relevant conclusions about the relationship between resonance frequencies and magnetic bearing stiffness can be drawn from **Fig. 2.4 (c)** with exemplary values of $v = 0.2$ and $b = 0.5$. For an elastic bearing with $a < 0.5$, the first natural frequency ω_1 represents the rigid body mode, and the second natural frequency ω_2 represents that of the free-free resonating shaft, i.e., the first bending resonance frequency. In the middle part, ω_1 and ω_2 are two "elastic" vibrations. The case of $1/a$ approaching 0 represents a rigid bearing, with ω_1 as the first bending resonance frequency and ω_2 as the vibration at which m_B oscillates in a manner almost not influenced by the shaft stiffness k_{shaft} on the magnetic bearing stiffness $P \cdot k_i - k_s$.

In summary, two vibrational modes are derived with this model, whose natural frequencies depend on the magnetic bearing stiffness. For the CFF rotors investigated in this work, the Jeffcott assumption of the massless shaft with an eccentric disc deviates from reality. Nevertheless, the lower rigid and higher bending mode natural frequencies shown in **Fig. 2.4 (c)** are expected to occur depending on the magnetic bearing's stiffness. The Jeffcott model enables the qualitative explanation of important rotor dynamic phenomena for the case of an elastic rotor in active magnetic bearings. For quantitative conclusions, a 3D FEM analysis was performed. In the next section, the
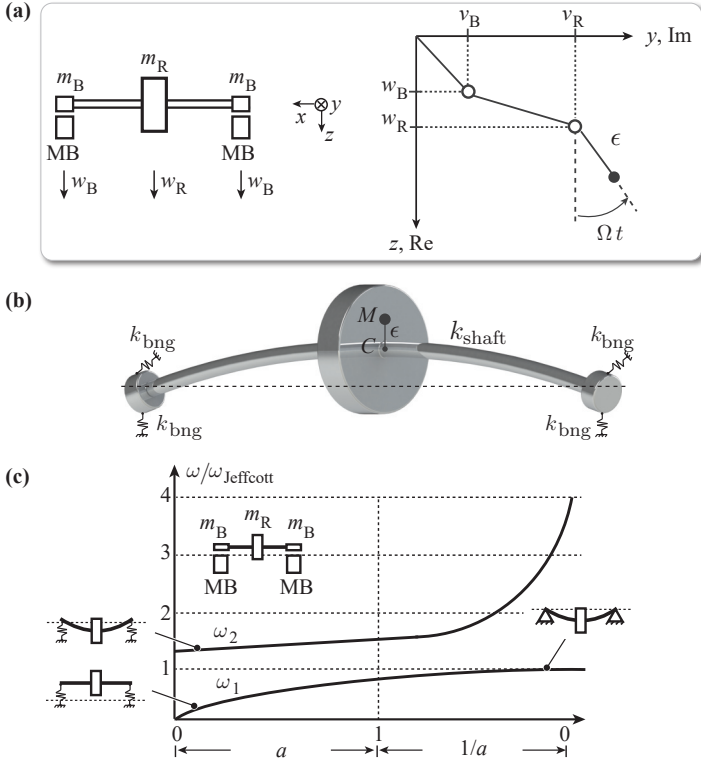
Fig. 2.4: (a) Degrees of freedom of the two-sided magnetically levitated, elastic Jeffcott
rotor model. (b) Rendering of the elastic Jeffcott rotor model in a magnetic bearing
system. (c) Relationship of the system's natural frequencies ω_1 and ω_2 with the
stiffness ratio $a = k_{bng}/k_{shaft}$, where k_{bng} is the magnetic bearing stiffness and k_{shaft}
is the shaft stiffness. In the region $0 < a < 1$, the magnetic bearing is weaker than the
shaft, whereas in region $1 < 1/a < 0$, the magnetic bearing is stiffer than the shaft. For
the elastic rotor at hand ($0 << k_{shaft} << \infty$), $a = 0$ means $k_{bng} = 0$, which represents
a free–free-supported elastic rotor, whereas having $1/a = 0$ means $k_{bng} \rightarrow \infty$, which
represents a rigidly supported elastic rotor.

implemented modal analysis is described, and a direct comparison of both prototypes is drawn.

2.4.2 Simulated Modal Analysis

The goal of the modal analysis was to determine the system's expected natural frequencies up to the first bending resonance frequency. The radial position of the proposed CFF system was controlled separately and independently in BM1 and BM2. In order to enable an assessment of this control method for different vibration types, a modal analysis was, therefore, important to estimate the expected resonance frequencies.

Modal analysis is, by definition, an analysis of linear dynamics based on the equation of motion with unknown displacement, velocity, and acceleration. It is assumed that in the equation of motion the external load equals 0 since natural frequencies and mode shapes are independent of the load. In addition, damping effects are neglected; hence, a free and undamped system is assumed, resulting in the eigenvalue problem

$$(\mathbf{K} - \omega_i^2 \mathbf{M})\left\{\phi\right\}_i = \left\{0\right\} \tag{2.9}$$

with eigenvalues ω_i and eigenvectors ϕ_i. This system of equations is subjected to the performed 3D FEM model to determine the mode shape $\left\{\phi\right\}_i$ and the associated frequency $f_i = \omega_i/(2\pi)$.

The Campbell diagrams resulting from the modal analysis are shown in **Fig. 2.5 (a)** for PT1 and in **Fig. 2.5 (b)** for PT2; they show the expected vibration modes and possible excitation orders up to the first bending resonance frequency. The unbalance excitation is of the first order. Three types of vibration modes are obtained, namely, the rigid body modes (cylindrical and conical), the torsional mode, and the first bending mode. The natural frequencies of the rigid body modes are given for both prototypes at speeds of about 1500–2000 rpm since these vibration modes are an interaction of the magnetic bearing stiffness and the rotor inertia and both prototypes have nearly similar masses (see **Tab. 3.3**) and the same magnetic bearing stiffness k_s. The radial bearing stiffness k_s was determined by simulation to be $k_s = 20 \, \text{N/mm}$.

The natural frequency of the torsional mode for PT1 lies between the natural frequencies of the solid and the first bending mode. For PT2, the torsional mode is just below the first bending mode.

The unbalance excitation of the first bending mode is expected to occur at 16 000 rpm for PT1 and at 8000 rpm for PT2. This suggests a significantly higher rotor stiffness of PT1 ($k_{\text{shaft,PT1}} > k_{\text{shaft,PT2}}$), as they have similar rotor

masses. Additionally, the mode shape analysis shows that vibrational nodes
are not located at the rotor shaft ends where the active magnetic bearing
controls the rotor position for both PT1 and PT2. Therefore, the first bending
resonance frequency will cause radial displacements within the bearings and
thus be observable for the magnetic bearing in both prototypes.
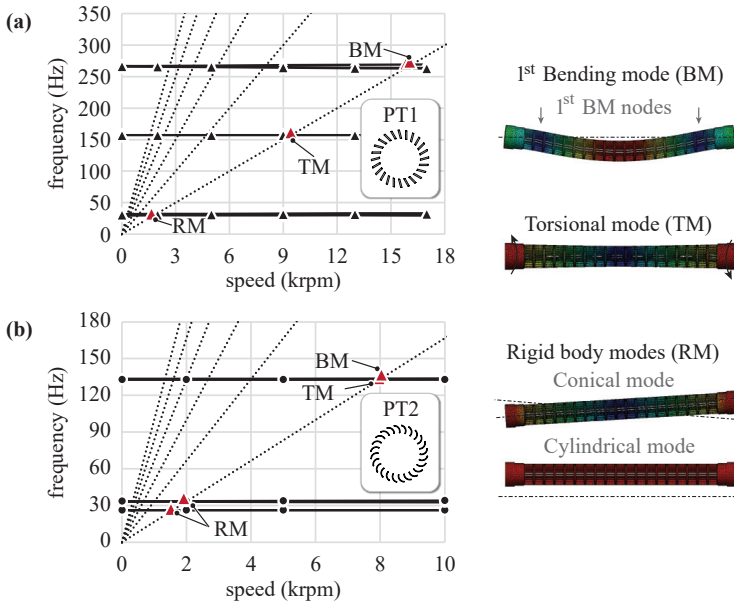
Fig. 2.5: Simulated Campbell diagrams of (**a**) PT1 and (**b**) PT2.

From the modal analysis, it can be concluded that rigid, torsional and
bending vibration modes can be excited in the targeted speed range and can
exert destabilizing forces on the magnetic bearing. The critical first bending
mode will lead to radial displacements in the magnetic bearing of PT1 and PT2,
whereby the stiff design of PT1 shifts the excitation to significantly higher
speeds due to mass unbalance.

20

2.5 Fluid Dynamic Analysis

The goal of this section is to gain an understanding of the fluid dynamic properties of the CFF and the effects of design changes for the high-speed speed range using CFD simulations.

From a fluid dynamic point of view, the CFF is characterized by its complex, non-axisymmetric flow profile. It is defined by a double passage of air through the rotating blades and the formation of an eccentric vortex within the impeller [39–45]. In the literature, CFFs are referred to as "low-pressure fans" or "velocity generators", as they do not generate high static pressure [46]. Generally, the energy increase created by a fan can be expressed as the sum of the increase in dynamic and static pressure

$$\Delta p_{\text{th}\infty} = \frac{\rho}{2} \big[\overbrace{(c_2^2 - c_1^2)}^{\text{dynamic}} + \overbrace{(w_1^2 - w_2^2) + (u_2^2 - u_1^2)}^{\text{static}} \big] \tag{2.10}$$

as the first form of Euler's fluid machine equation, where c is the absolute, u the circumferential, and w the relative velocity. Since the geometric sum of the circumferential and relative velocity gives the absolute velocity, the second form of Euler's fluid machine equation [46] is obtained as

$$\Delta p_{\text{th}\infty} = \rho(u_2 \cdot c_{2u} - u_1 \cdot c_{1u}). \tag{2.11}$$

For a CFF, the fluid inlet and outlet are at the same rotor diameter ($u_1 = u_2 = u$), such that the theoretical pressure increase can be written as

$$\Delta p_{\text{th}\infty} = \rho \cdot u \cdot \Delta c_u, \tag{2.12}$$

where Δc_u is the theoretical velocity deflection for an infinite number of blades. The total pressure increase is achieved by the deflection of the absolute velocity. How the velocity deflection occurs depends strongly on the impeller and casing geometry and is significantly influenced by the position, size, and intensity of the resulting eccentric vortex [47–49]. Analytical models are not able to accurately capture these aerodynamic features and loss mechanisms, so characteristic pressure–flow curves cannot be predicted. There are no conventional design procedures for CFFs; hence, the use of numerical methods is essential.

Therefore, a 2D simulation model was implemented that is robust in terms of numerical mesh and time step settings and provides a good compromise between computation time and resolution. The CFD model is described in the next section.
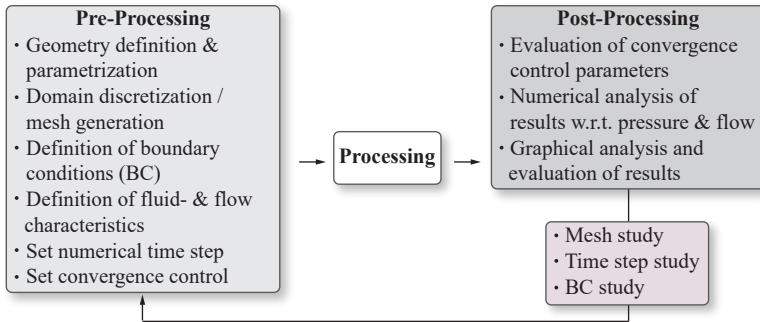
Fig. 2.6: Summary of the conducted pre-processing, processing, and post-processing steps for the development of the CFF CFD model.

2.5.1 Numerical Method

The challenge in developing the CFD model lies particularly in the physics of the transient CFF flow. A sufficiently high resolution of the domain and the numerical time step was needed to reproduce the CFF flow, which is strongly dependent on the rotor and casing geometry. Furthermore, we determined that a comprehensive mesh and time step convergence study of the transient simulation should be conducted.

Fig. 2.6 summarizes the implemented steps for the creation and execution of the CFD simulations. Due to the uniform flow profile along the length of the CFF, cross-sectional planar 2D simulations were performed [48].

Three-dimensional effects are neglected due to the predominantly tangential flow fields. Moreover, the air (in a first step at room temperature, with a density $\rho = 1.225 \, \text{kg/m}^3$ and viscosity $\mu = 1.7894 \cdot 10^{-5} \, \text{kg/(m} \cdot \text{s))}$ was modeled as incompressible since the expected Mach numbers are below 0.3 (subsonic) and the CFF generates low pressures. Only high-flow operating points were simulated since the incompressible modeling of the air causes strong pressure fluctuations at low-flow operating points and thus does not represent the physical conditions well enough [48]. The sliding mesh method was used as the calculation approach, and the $k - \omega$ SST model was used as the turbulence model.

Several mesh configurations, N, have been evaluated according to **Fig. 2.7 (a)**. The focus is placed on refinements in the rotating region, at the interface between rotating and static domain, and at the walls in order to sufficiently resolve velocity gradients. From mesh 4 onward, an independent and robust
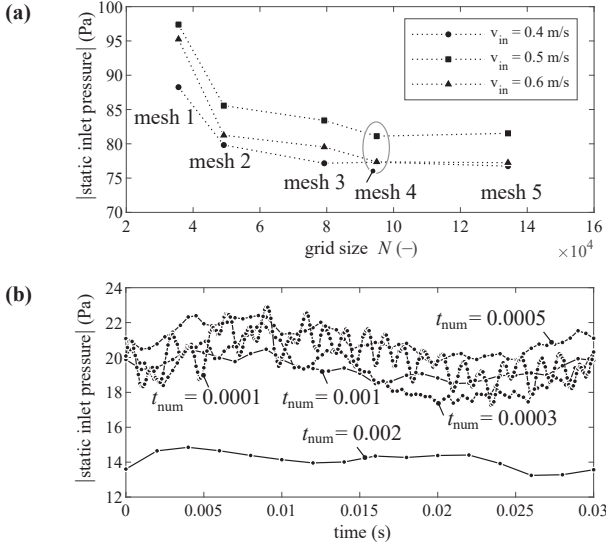
Fig. 2.7: Results of the **(a)** mesh and **(b)** time step sensitivity study.

mesh is obtained, with physical quantities remaining constant even with further increases in grid size, N. **Fig. 2.8** shows the discretized 2D domain in the CFF region. Furthermore, the boundary conditions reflect the relationship between the numerical simulation and the physical environment with a velocity inlet condition v_{in} and a static outlet pressure of $p_{stat,out} = 0\,\text{Pa}$ (relative to the ambient pressure). By varying the velocity inlet condition, different operating points can be simulated.

A detailed sensitivity study with respect to the numerical time step t_{num} was performed, which is shown in **Fig. 2.7 (b)**. It resulted in a speed-dependent time step of 0.015 rotor turns, e.g., for 3000 rpm, the time step was set to 0.0003 s.

In summary, the resulting 2D simulation model is robust in terms of numerical mesh and time step settings and offers a good trade-off between computation time and resolution. It can be used to simulate various rotor geometries at different speeds and operating points.

Fig. 2.8: Image of the resulting discretized domain in CFF region.

2.5.2   Results of Simulation

Fig. 2.9 (a) shows the velocity and pressure profiles resulting from the CFD
simulation for PT1, and those for PT2 are shown in **Fig. 2.9 (b)**. The velocity
vectors show the inflow and outflow regions and the characteristic non-
axisymmetric flow profile of both PTs. As expected, the air passes each fan
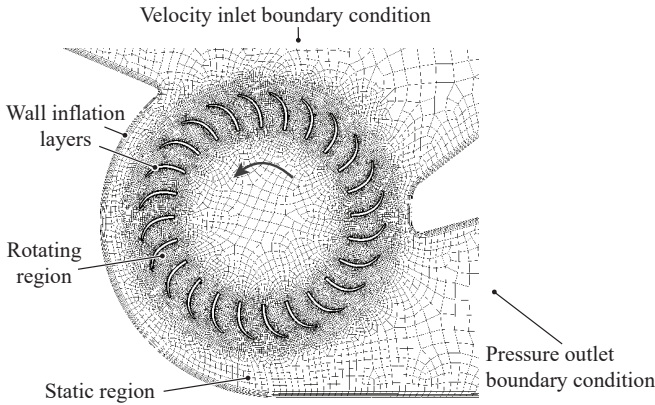blade twice, first as it enters the fan impeller and then again as it exits. The
eccentric vortex is shown in the pressure profiles for both PTs. Thus, the
implemented CFD simulation allows a successful visual representation of the
CFF pressure and flow characteristics. The comparison of straight (PT1) and
curved (PT2) blades show that at the same rotational speed and at a high-flow
operating point, the velocities at the outlet of PT2 are significantly higher.

Furthermore, **Fig. 2.10 (a),(b)** illustrates the absolute value of the static
inlet pressure versus the number of conducted numerical time steps (for the
same operating point as in **Fig. 2.9 (a),(b)**). This demonstrates a successful
convergence after approximately six turns, as a 360° rotation of the fan blades
corresponds to 66.67 time steps.

In **Fig. 2.11 (a),(b)**, different operating points are simulated for different
speeds and compared with those experimentally determined (see **Sec. 2.6**). To
obtain the flow rate from the 2D simulation, the inlet velocity was multiplied
by the effective fluid inlet length (see L_{fluid} in **Tab. 3.3**) and the height of the
channel (see h_{channel} in **Sec. 2.6**). For the high flow speed curves of PT2 in
Fig. 2.11 (b), the simulated and measured points agree very well. However, in

Fig. 2.11 (a), it can be seen that the simulated speed curves of PT1 are higher than the measured ones.
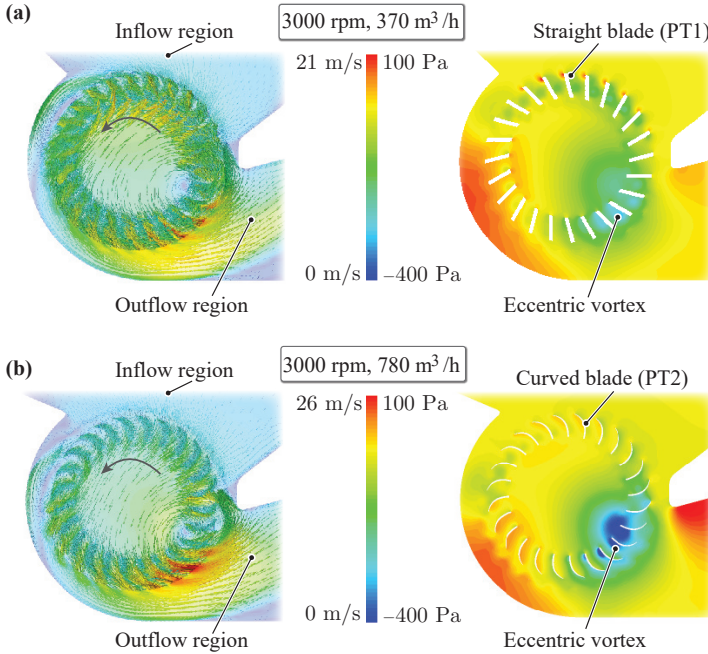
Fig. 2.9: CFD-simulated velocity and pressure profile of (**a**) PT1 and (**b**) PT2 for a high-flow operating point at 3000 rpm. The characteristic flow features are shown for both PTs.

This deviation could originate from wall boundary conditions and loss mechanisms that occur at the flow inlet and outlet of PT1, which consist of several individual inlet surfaces in the axial direction but are not represented in the planar 2D simulation. Furthermore, it could stem from manufacturing tolerances as the CFF's performance is strongly dependent on the slope of the fan blades.

Different blade slopes have been simulated for the milled PT1 for a blade thickness of 1.4 mm, as predefined by the manufacturing process. The simulated high-flow operating points for a slope of 14°, 16° (PT1), and 18° are shown in **Fig. 2.12 (c)**. The velocity and pressure profiles for blades with a slope of 14° (steeper than PT1) are shown in **Fig. 2.12 (a)** and of 18° (flatter than PT1)

(a) static inlet pressure | (Pa), 3000 rpm, 370 m³/h, 1 turn = 66.67 time steps, PT1, t_{num} = 0.0003 s, number of time steps (−)

(b) static inlet pressure | (Pa), 3000 rpm, 780 m³/h, 1 turn = 66.67 time steps, PT2, t_{num} = 0.0003 s, number of time steps (−)
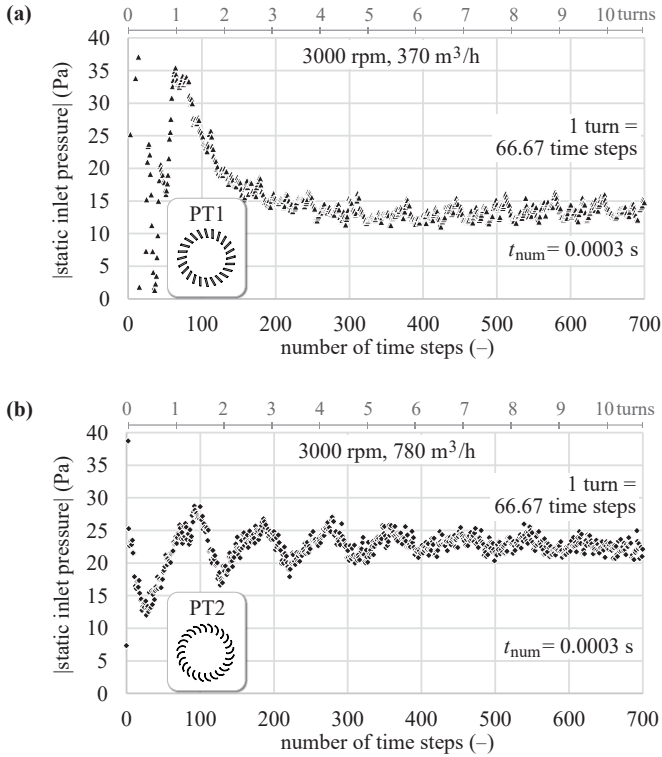
Fig. 2.10: Convergence study evaluating the control points (absolute value of static inlet pressure) over the number of numerical time steps for PT1 in (**a**) and for PT2 in (**b**).
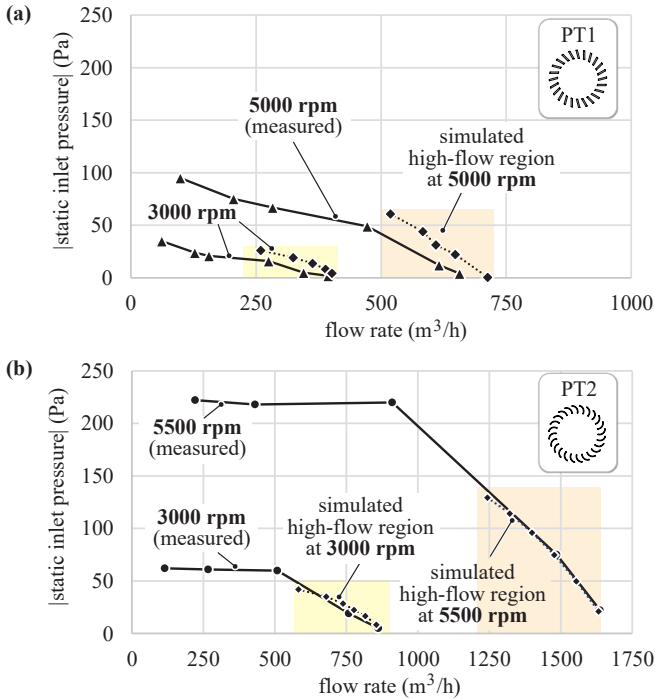
Fig. 2.11: Comparison of the experimentally and simulatively determined pressure–flow characteristics for PT1 in (**a**) and for PT2 in (**b**).

in **Fig. 2.12 (b)**. An influence of the blade angle on the velocity and pressure distributions can be seen.

The simulations have shown that if the blade slope is too steep, there is a higher impact pressure on the blades at the inlet side (pressure loss), resulting in a reduced deflection of the absolute velocity on the outlet side. If the blade slope is too flat, the air supply into the fan is blocked more on the inlet side, which has negative consequences on the dynamic pressure supplied to the flow on the outlet side. The geometry of PT1 resulted from iteratively varying the slope of the blades for a given inner diameter d_i, outer diameter d_o, and blade thickness t_{PT1} and has shown the best flow characteristics for 16°.

27

(a)

3000 rpm, 260 m³/h

21 m/s ▮ 140 Pa

0 m/s ▮ −310 Pa

14° (steeper than PT1)

(b)

3000 rpm, 350 m³/h

21 m/s ▮ 140 Pa

0 m/s ▮ −310 Pa

18° (flatter than PT1)

(c)

3000 rpm

16° (PT1)

14°
(steeper than PT1)

18° (flatter
than PT1)

|static inlet pressure| (Pa)

flow rate (m³/h)

Fig. 2.12: Velocity and pressure profiles for straight blades with slope of **(a)** 14° and
(b) 18°. **(c)** Simulative comparison of straight blades with three different slopes.

2.6   Experimental Analysis

For the experimental CFF study, all measurements were performed with air under ambient pressure. For other operating conditions, e.g., higher gas density i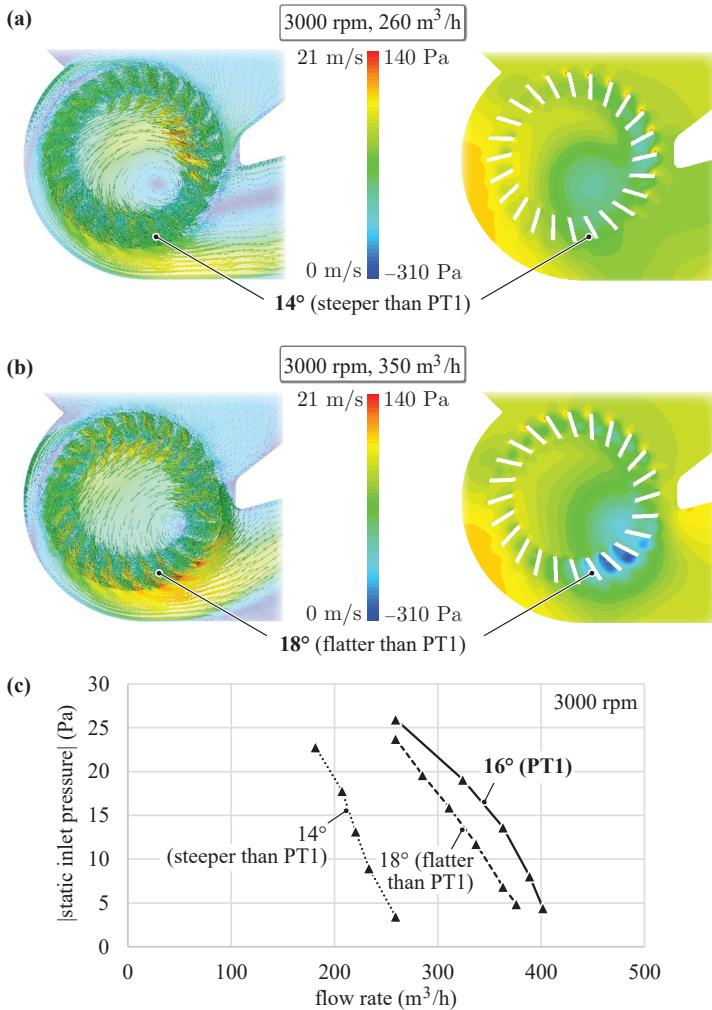n an excimer laser chamber, a conversion would be possible using the linear relationship between pressure difference and density as $\Delta p_{\text{excimer}} \propto \Delta p_{\text{air}} \cdot \rho_{\text{excimer}}/\rho_{\text{air}}$. The test rig that is shown schematically in **Fig. 2.13 (c)** was designed, while an image of the entire high-speed bearingless CFF system with PT1 is shown in **Fig. 2.13 (a)**. The flow into the CFF was guided through a 4.5 m long ventilation duct, with free flow exiting the CFF. At the duct inlet, an exchangeable grid set the load curve, i.e., it defined a certain operating point. A flow straightener then ensured that the flow was directed and the velocity measurement was accurately measured by the thermal flow sensor. The static pressure measurement took place before the fan.

To investigate the velocity distribution in the ventilation duct, the velocity was measured across the width at different locations. The velocity profile can be seen in **Fig. 2.13 (b)**. From this, the profile factor of the flow could be calculated according to

$$\text{PF} = \frac{v_{\text{avg}}}{v_{\text{s}}}, \tag{2.13}$$

where v_{s} is the velocity at the sensor in the center of the duct and v_{avg} is the mean velocity. The flow rate then resulted from multiplying v_{s} by the profile factor and the duct area with

$$Q = v_{\text{s}} \cdot \text{PF} \cdot h_{\text{channel}} \cdot b_{\text{channel}}. \tag{2.14}$$

For this test rig, a profile factor of 0.92 was obtained.

2.6.1   Position Measurements of Rotor Magnets

The magnetic bearing must be able to withstand the rotor and fluid dynamic forces, as discussed in **Sec. 2.4**. The aim of these measurements was to determine which maximum rotational speeds could be achieved with the independent position control structure of BM1 and BM2 and what the present limitations were. The displacements of the rotor magnet in the magnetic bearing were evaluated and were measured via built-in sensors in the bearingless motor.

Fig. 2.14 (a) shows the measured radial displacements of the rotor magnet for BM1 and BM2 at different speeds of PT1, and those of PT2 are shown

(a)

(b)

(c)

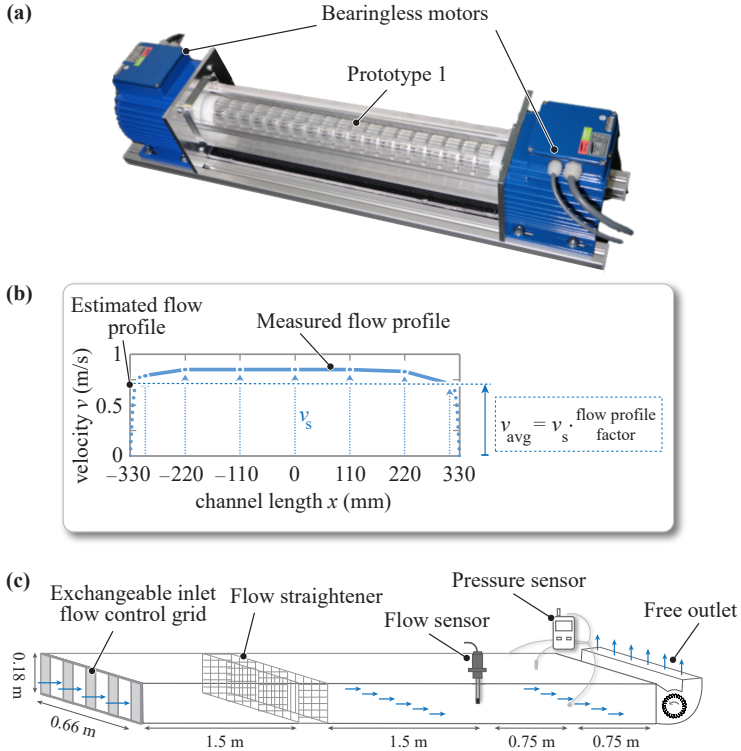**Fig. 2.13:** **(a)** Image of the entire high-speed bearingless CFF system with PT1. **(b)** Velocity profile measured with the flow sensor in the center of the ventilation duct at different channel width positions. **(c)** Schematic of the designed test rig with inlet grid, flow straightener, flow sensor, and pressure sensor. The flow into the CFF is ducted, while the flow exits freely from the fan into the environment.

in **Fig. 2.14 (b)**. The measurements were carried out for each speed for two operating points, namely at maximum ("max flow") and minimum ("no flow") flow. The rigid body modes simulated in **Fig. 2.5** did not pose a problem for the magnetic bearing since a "force-rejection" algorithm was implemented in the position control [38]. This unbalanced control strategy can be interpreted as a generalized notch filter. This shifted the axis of rotation of an unbalanced rotor from the geometric center of gravity to the center of mass, such that the rotor rotated in a completely force-free manner. Thus, no rigid body modes could be excited by the unbalance. Furthermore, the forces generated by the air flow (no-flow versus max flow points in **Fig. 2.14 (a),(b)**) had no measurable/no significant influence on the rotor displacement in the magnetic bearing. Therefore, we considered them to be neglectable. The predicted torsional mode was also not excited during the measurements and did not lead to any destabilizing forces.
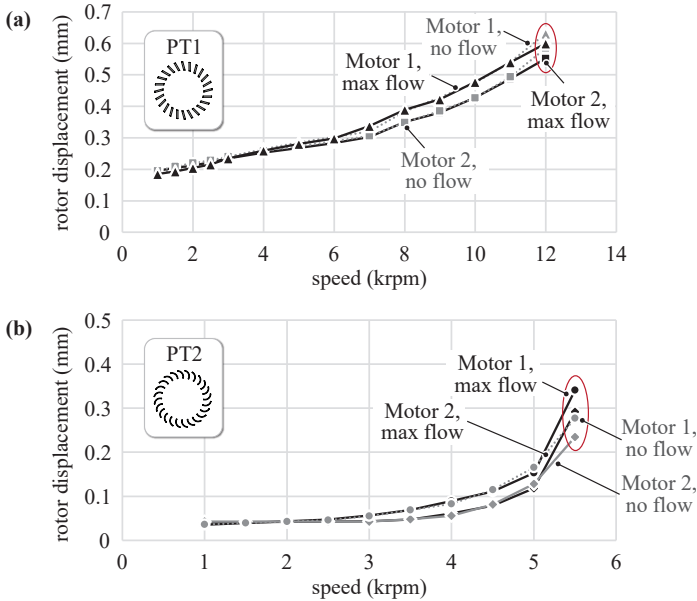

Fig. 2.14: Measured radial rotor displacements in the magnetic bearing of **(a)** PT1 and **(b)** PT2.

In contrast, the first bending mode occurred for both rotors. In **Fig. 2.14 (b)**, the quickly increasing radial displacements of the less stiff CFF are clearly

31

visible. Stroboscopic measurements optically confirmed the bending of the rotor. With the present control structure, the first bending resonance frequency could not be passed, meaning that PT2 could only operate subcritically—but stably—up to 5500 rpm. The critical speed of the first bending mode of 8000 rpm simulated in **Fig. 2.5 (b)** most likely overestimates the mechanical stiffness due to the multi-body nature of the prototype and the imperfectly bonded connections between the individual components, which is why the first bending resonance frequency occurs earlier in the measurement.

PT1 was successfully operated up to 12 000 rpm (see **Fig. 2.14 (a)**). Due to the large air gap offered by the bearingless motor (as explained in **Sec. 2.2**), large displacements, and thus, high speeds, can be allowed with the "force-rejection" algorithm. The simulated bending resonance frequency of 15,500 rpm from **Fig. 2.5 (b)** also occurred earlier with PT1 and could not be passed.

The higher displacements of PT1 compared to PT2 at low speeds indicated a higher mass unbalance. Although balancing can reduce the displacements up to the resonance frequency, it is still not possible to pass the critical speed. In addition, it can be concluded from both diagrams that the radial displacements are approximately the same at maximum and minimum flow, which means that the rotor dynamic forces dominate over the fluidic forces.

For both PTs, the first bending resonance frequency currently represents the limit for the magnetic bearing of the bearingless motor, which is why both PTs could only be operated subcritically.

2.6.2   Pressure–Flow Curves

Fig. 2.15 (a) shows the characteristic pressure–flow curves of PT1. This CFF reached a maximum speed of 12 000 rpm with a maximum flow rate of approximately 1450 m^3/h. **Fig. 2.15 (b)** shows the pressure–flow characteristics of PT2, resulting in a flow of approximately 1600 m^3/h at the maximum achieved speed of 5500 rpm. The comparison of PT1 and PT2 shows experimentally that the robust design of PT1 allows for high speeds, but there is a loss in flow rate. This results from the shorter effective fluid inlet length (see **Tab. 3.3**) in combination with the straight blade profiles.

Comparing the fluid performance (the multiplication of pressure increase and flow rate) at maximal speed for PT1 and PT2, PT1 generates a higher performance for operating points with higher resistance. Depending on the resistance of the heat exchangers in the excimer laser application, this can be advantageous.

Overall, PT2 performs better from a maximal flow point of view, but the low shaft stiffness and the excitation of the first bending resonance frequency do not allow higher speeds than 5500 rpm, while the robust design of PT1 allowed rotational speeds up to 12 000 rpm and thereby led to a fluid performance increase for operating points with higher resistance, e.g., from the heat exchangers.
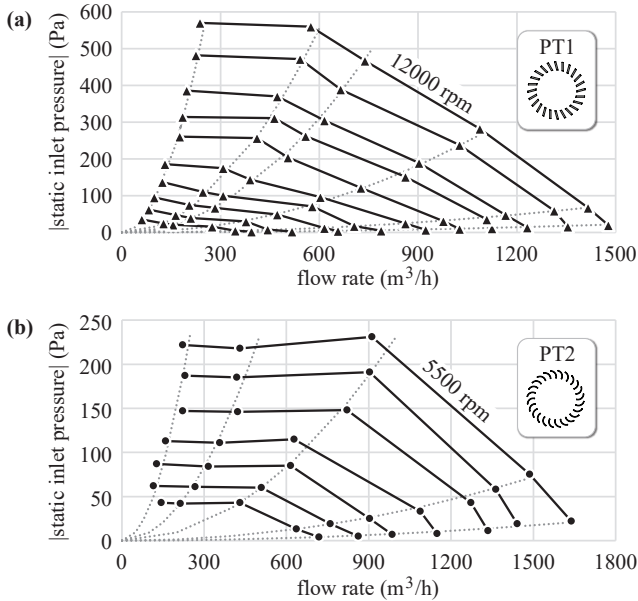
Fig. 2.15: Pressure–flow curves measured in the presented test rig for **(a)** PT1 at increments of 1000 rpm up to 12 000 rpm and **(b)** PT2 at increments of 500 rpm up to 5500 rpm.

2.7 Summary

In this chapter, a comparative evaluation of two bearingless cross-flow fan designs was performed. Two prototypes were designed, optimized, and analyzed in terms of their rotor dynamic and fluid dynamic performance and pushed towards high-speed and high-performance operation. For the target application in DUV lithography excimer lasers, the bearingless CFF concept allows for a simple, hermetically sealed and conveniently maintainable and

33

exchangeable placement of the drives outside the laser chamber. An increase
in CFF speed and thus flow has a direct impact on the throughput and scan
speeds of these systems.

This chapter addresses the trade-off and complex interactions between
the mechanical strength, fluid dynamic performance, and manufacturability
of the CFF rotor and the consequent impact on the magnetic bearing and max-
imum achievable speed. For this purpose, two prototypes were successfully
commissioned and investigated by FEM and experimental measurements. The
performed modal analysis allowed an estimation of expected vibration modes,
particularly the critical speed of the first bending mode and its node location.
With the presented CFD simulation, a visualization of local flow effects along
the blade geometries, as well as a CFF design comparison, was accomplished.

PT1 represents an easily manufacturable and stiff rotor that could be
operated up to 12 000 rpm. This demonstrated that stable operation up to the
first bending resonance frequency in this high-speed range is possible with
the current position control structure. At maximal speed, PT1 resulted in
higher fluid power for operating points with higher resistance compared to
PT1. However, the robust design comes at the expense of a limited fluid flow.

PT2 performs much better from a fluid dynamic point of view, but the
more flexible design limits the maximum achieved speed to 5500 rpm due to
the excited first bending resonance frequency.

It can be concluded that the magnetic bearing can only handle forces
and allow deflections to a limited extent and that the first bending resonance
frequency currently limits the position control of the bearingless motor pre-
sented here. Future research will focus on passing the critical speed to obtain a
better trade-off between rotational speed and fluid performance with the same
unique technical advantages that the bearingless CFF technology currently
offers.

3

Supercritical Operation of Bearingless Cross-Flow Fan

This chapter summarizes the most relevant findings regarding the novel decoupled bearingless cross-flow fan, which enhances the performance of CFFs, as also published in:

▶ I. Bagaric, D. Steinert, T. Nussbaumer and J. W. Kolar, "Supercritical Operation of Bearingless Cross-Flow Fan," *Machines*, vol. 12(4), no. 223, March 2024.

Chapter Abstract

This chapter presents a decoupled bearingless cross-flow fan (CFF) that operates at a supercritical speed, thereby increasing the maximum achievable rotational speed and fluid dynamic power. The novel CFF rotor features additional mechanical decoupling elements with low bending stiffness between the fan blades and the rotor magnets. Thus, the unbalance forces primarily deform the soft decoupling elements, which enables them to pass resonances without CFF blade damage and allows rotor operation in the supercritical speed region due to the self-centering effect of the rotor. The effects of the novel rotor design on the rotor dynamic behavior are investigated by means of a mass-spring-damper model. The influence of different decoupling elements on the magnetic bearing is experimentally tested and evaluated, from which an optimized decoupled CFF rotor is derived. The final prototype enables a stable operation at 7000 rpm in the supercritical speed region. This corresponds to a rotational speed increase of 40 %, resulting in a 28 % higher, validated fluid flow and a 100 % higher static pressure compared to the previously presented bearingless CFF without decoupling elements.

3.1   Introduction

Cross-flow fans (CFFs) installed in the semiconductor industry are exposed to harsh environmental conditions due to toxic and corrosive gases and are subject to stringent standards. No wear, friction or contamination, and a rotor inside a hermetically sealed process chamber are crucial and lead to the highest performance requirements for the implemented drives. Bearingless motors enable wear-free, practically maintenance-free, and continuous operation of CFFs under these extreme conditions. In [50], the authors presented the bearingless high-speed CFF for applications in deep ultraviolet (DUV) excimer laser, which are commonly used as the light source in industrial lithography systems [7]. The fluid dynamic performance of the CFF is an important factor that limits the gas exchange rate of the lasers in a given, constrained installation space of complex manufacturing devices. Increasing the CFF rotational speed and therefore the fluid performance is a key enabler for improving the laser performance, the scanning speed of lithography systems, and finally, the chip throughput [8, 18, 20, 22].

The maximum achievable rotational speed of current bearingless CFFs is restricted by the plastic deformation of the CFF rotor at the critical bending resonance frequency. The operation is therefore limited to subcritical speeds. This chapter presents a bearingless CFF rotor, which is operated supercritically to increase the fluid dynamic performance. The CFF rotor features additional mechanical elements with low stiffness (hereafter referred to as "decoupling elements"), which connect the rotor magnets and the CFF blades according to **Fig. 3.1**. The influence of the decoupling elements on the rotor dynamic behavior (vibration modes) is examined by a mass-spring-damper model and the influence on the magnetic bearing is tested with different prototypes. Additionally, the effects on the CFF's fluid dynamic performance are evaluated.

CFF rotors have a distinctive large length-to-diameter ratio and consist of several thin blades arranged in a circular manner to achieve the optimal fluid dynamic performance [45, 51, 52]. The long and thin blades result in a low mechanical bending stiffness. Consequently, the CFF rotor plastically deforms under the unbalance forces, which increase quadratically with the rotational speed, at the critical bending resonance frequency. The use of magnetic bearings amplifies this problem due to the rotor magnets on both ends of the CFF rotor, which add significant mass but minimal contribution to the overall rotor bending stiffness. The CFF rotor presented in [50] consists of two rotor magnets, which are rigidly mounted to the CFF blades as depicted in **Fig. 3.2 (a)**.
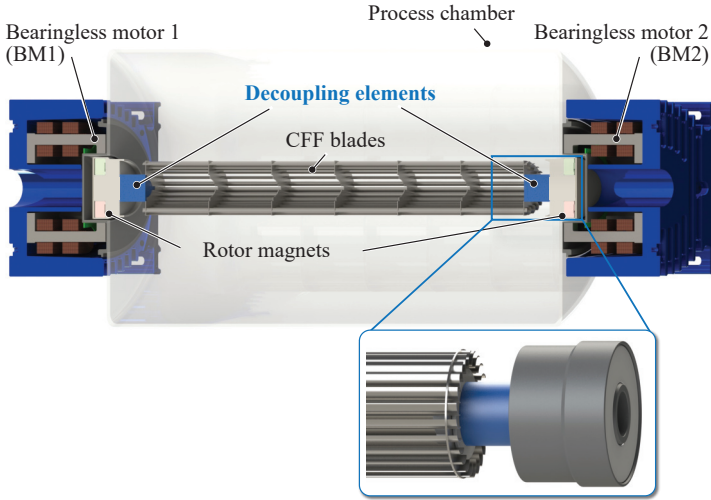
Fig. 3.1: Schematic cross-sectional view of the bearingless CFF system in a hermetically sealed process chamber. The CFF rotor consists of CFF blades, which are decoupled from the rotor magnets by decoupling elements. By adding components with low mechanical stiffness, i.e., $k_{dE} < k_{CFF\,blades}$, the rotor dynamical behavior is influenced such that the resonance frequency, which bends the CFF blades, is shifted to higher rotational speeds.

The maximum achievable speed is limited by the bending resonance frequency. The low bending stiffness of the CFF blades causes plastic deformation of the blades near the bending resonance frequency, which prevents its surpassing, as shown in **Fig. 3.2 (a)** with $\omega_{2,CFF_{fix}}$. Thus, the CFF is limited to subcritical operation.

In the literature, different control approaches for the active magnetic bearing system to dampen, pass or eliminate resonance frequencies are proposed [53–66]. Complex position control methods are presented to pass the bending resonance frequency of a flexible test rotor. However, these methods consider massive shafts and Jeffcott rotors with mass distributions and bending stiffnesses that are not comparable to the CFF rotor, of which the mechanical design is restricted by the fluid dynamical requirements. Therefore, the proposed control algorithms are not directly applicable to the problem at hand.

In this chapter, however, a rotor design approach is explored to shift the CFF's critical resonance frequencies and rotor bending to higher rotational

speeds. Additional mechanical elements with a low stiffness decouple the CFF blades from the rotor magnets. The vibration behavior is influenced such that an additional, third resonance frequency occurs as visualized in **Fig. 3.2 (b)**.
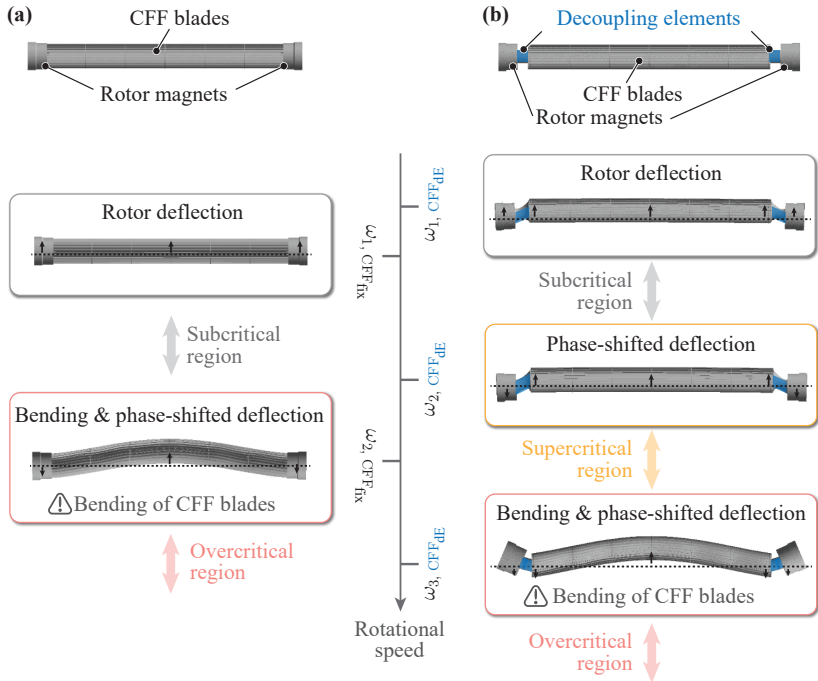
Fig. 3.2: Designs of bearingless CFF rotors: **(a)** The rotor magnets are directly mounted to the CFF blades (CFF$_{fix}$), causing plastic deformation at the first critical bending resonance. This limits the maximum achievable rotational speed. **(b)** The CFF blades are separated from the magnets by additional series elastic elements with low mechanical stiffness (CFF$_{dE}$). This enables the passing of the first and second bending resonance frequency and shifts the critical bending resonance $\omega_{3,\mathrm{CFF}_{dE}}$ to higher rotational speeds.

The decoupling elements are deformed under the unbalance forces at the first two resonance frequencies $\omega_{1,\mathrm{CFF}_{dE}}$ and $\omega_{2,\mathrm{CFF}_{dE}}$, which results in a deflection and small, non-plastic deformation of the CFF blades. The two-mode shapes differ in the phase shift between rotor magnets and the CFF rotor. The region above the first two resonance frequencies is referred to as the supercritical region since the CFF rotor centers itself with respect

38

to the rotational axis [38, 67]. The third resonance frequency, $\omega_{3,\mathrm{CFF_{dE}}}$, is characterized by the detrimental bending of the CFF blades, similar to the second resonance frequency of the non-decoupled CFF, which again leads to plastic deformation of the CFF blades. However, $\omega_{3,\mathrm{CFF_{dE}}}$ is shifted to higher frequencies than $\omega_{2,\mathrm{CFF_{fix}}}$ of the non-decoupled rotor. Hence, the new rotational speed limit can be increased.

The design of the multi-component rotor is critical. The decoupling elements must have a low enough mechanical stiffness to enable effective mechanical decoupling and therefore prevent the bending of the blades. But the stiffness cannot be too low such that the fluid dynamic forces acting on the rotor lead to high deflections and instabilities. Furthermore, the magnetic bearing must be able to withstand the forces that result from passing through the resonance frequencies $\omega_{1,\mathrm{CFF_{dE}}}$ and $\omega_{2,\mathrm{CFF_{dE}}}$.

This chapter aims to address these challenges by first modeling the bearingless CFF rotor with a mass-spring-damper model in **Sec. 3.2**, to analyze the influence of the introduced decoupling element. Various decoupling elements are then experimentally tested, to evaluate their influence on the magnetic bearing and compared with the mass-spring-damper model in **Sec. 3.3**. Finally, the fluid dynamic performance of the CFF rotor with the optimal decoupling element is investigated in **Sec. 3.4**.

3.2 Modeling of CFF Resonance Frequencies

The goal of this section is to gain an understanding of the vibration modes of bearingless CFF rotors with and without decoupling elements by means of a mass-spring-damper (*mkd*)-model. The focus lies on the comparison of the resonance frequencies and mode shapes of CFF rotors with rigidly mounted rotor magnets to the newly introduced, decoupled rotors, particularly to investigate the modes associated with the bending of the CFF blades, since these are speed and performance-limiting. The influence of the decoupling element stiffness is investigated and the effect of shifting the critical bending resonance frequency to higher frequencies explained.

3.2.1 *mkd*-Model of Bearingless CFF Rotor

The bearingless CFF rotor is modeled using *mkd*-elements as shown in **Fig. 3.3**. The rotor is assumed symmetrical; thus, only symmetrical vibration modes are studied. The rotor magnets with mass m_B are coupled to the fixed reference frame via the magnetic bearing, which is modeled by the stiffness k_B and

damping value d_B. The parameters k_B and d_B can be influenced by the PD position control parameters of the magnetic bearing according to

$$k_\mathrm{B} = P \cdot k_\mathrm{i} - k_\mathrm{s} \tag{3.1}$$

and

$$d_\mathrm{B} = D \cdot k_\mathrm{i} \tag{3.2}$$

where P is the position-proportional and D the velocity-proportional feedback element of the PD control, k_i the force/current and k_s the force/displacement constant of the drive [38].

The CFF blades are represented in a simplified manner with a measured mass m_CFF, bending stiffness k_CFF and internal damping $d_\mathrm{i,CFF}$, while $d_\mathrm{i,CFF} \ll d_\mathrm{B}$. The mass of the CFF blades is modeled using three mass elements to represent the connection between the rotor magnets and blades as well as to clearly characterize vibration modes leading to rotor bending. The decoupling element, connecting the rotor magnets and CFF blades, is modeled as a spring with stiffness k_dE. Its mass and internal damping are assumed to be negligible. The systems' mass unbalance is modeled such that it is concentrated in the CFF center mass element and that it is created by the small offset ϵ. It denotes the offset of the mass center from the axis of rotation, which only influences the resonance amplitude and is set to a finite small value for this analysis.

Thus, the following equations of motion are obtained for the modeled CFF system

$$\mathbf{M} \begin{Bmatrix} \ddot{x}_\mathrm{B} \\ \ddot{x}_\mathrm{CFF,e} \\ \ddot{x}_\mathrm{CFF,c} \end{Bmatrix} + \mathbf{D} \begin{Bmatrix} \dot{x}_\mathrm{B} \\ \dot{x}_\mathrm{CFF,e} \\ \dot{x}_\mathrm{CFF,c} \end{Bmatrix} + \mathbf{K} \begin{Bmatrix} x_\mathrm{B} \\ x_\mathrm{CFF,e} \\ x_\mathrm{CFF,c} \end{Bmatrix} = \begin{Bmatrix} 0 \\ 0 \\ F_\mathrm{u}(t)/2 \end{Bmatrix}. \tag{3.3}$$

This results in the unbalance force excitation

$$F_\mathrm{u}(t) = m_\mathrm{CFF}/4 \cdot \epsilon \cdot \omega^2 \mathrm{e}^{\mathrm{j}\omega t}, \tag{3.4}$$

with ϵ being the mass eccentricity rotating at frequency ω [37, 68–72]. The mass matrix $\mathbf{M}$ is defined as

$$\mathbf{M} = \begin{bmatrix} m_\mathrm{B} & 0 & 0 \\ 0 & m_\mathrm{CFF}/4 & 0 \\ 0 & 0 & m_\mathrm{CFF}/4 \end{bmatrix}, \tag{3.5}$$

the damping matrix $\mathbf{D}$ as

$$\mathbf{D} = \begin{bmatrix} d_\mathrm{B} & 0 & 0 \\ 0 & d_\mathrm{i,CFF} & -d_\mathrm{i,CFF} \\ 0 & -d_\mathrm{i,CFF} & d_\mathrm{i,CFF} \end{bmatrix} \tag{3.6}$$
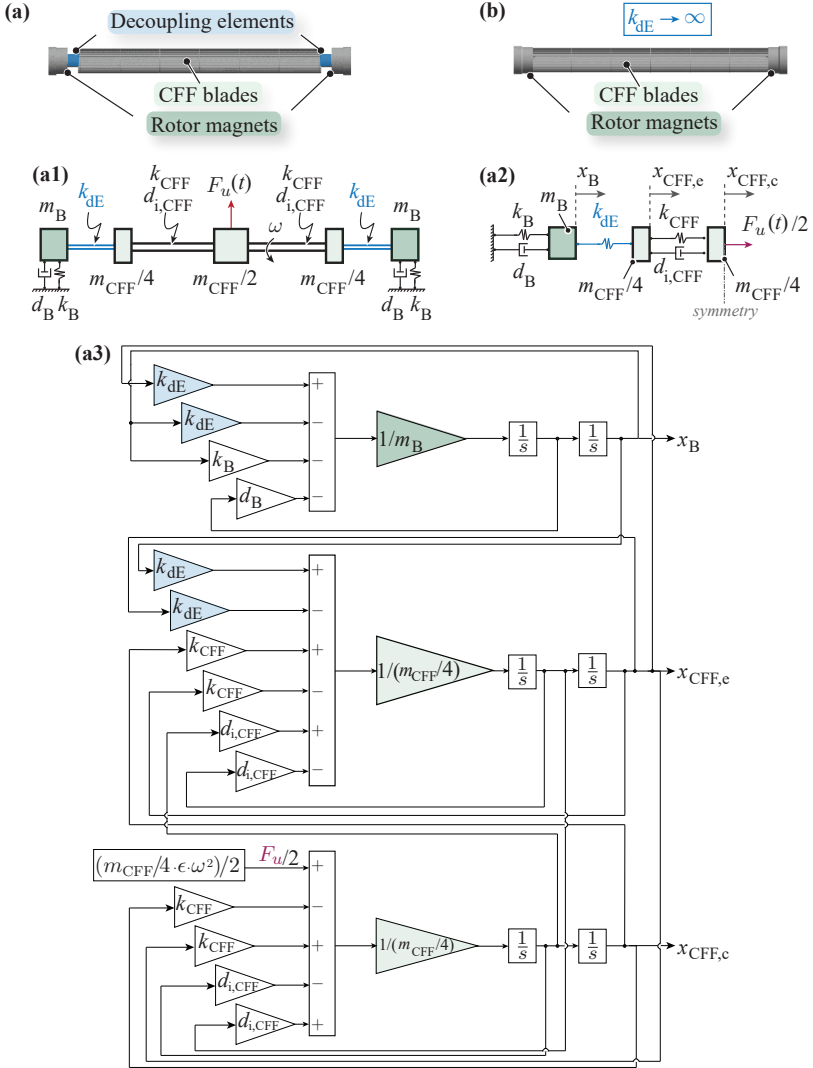
Fig. 3.3: Models of bearingless CFF rotors. **(a)** The decoupled CFF rotor is shown, where **(a1)** presents the mechanical and **(a2)** the simulation *mkd*-model including elements for the magnetic bearing (k_B, d_B), CFF blades (k_{CFF}, $d_{i,CFF}$, m_{CFF}) and decoupling element (k_{dE}), while **(a3)** shows the algorithm scheme of the implemented simulation model. **(b)** The CFF rotor with rigidly mounted rotor magnets, which is simulated with $k_{dE} \rightarrow \infty$.

and stiffness matrix $\mathbf{K}$ as

$$\mathbf{K} = \begin{bmatrix} k_{dE} + k_B & -k_{dE} & 0 \\ -k_{dE} & k_{CFF} + k_{dE} & -k_{CFF} \\ 0 & -k_{CFF} & k_{CFF} \end{bmatrix}. \tag{3.7}$$

To simulate the CFF rotor with rigidly mounted rotor magnets, the spring constant of the decoupling element can be set to $k_{dE} \to \infty$. Alternatively, for a decoupled CFF rotor, k_{dE} is set to a finite, variable value. An unbalance force F_u is then applied and the following amplitudes are evaluated: magnetic bearing deflection $\hat{x}_B$, the CFF blades' edge deflection $\hat{x}_{CFF,e}$ and CFF blades' center deflection $\hat{x}_{CFF,c}$.

3.2.2 Unbalance Response of CFF with Rigidly Mounted Rotor Magnets

The simulated resonance frequencies are evaluated with respect to the ratio between the magnetic bearing stiffness k_B and CFF blades stiffness k_{CFF} and the results shown in **Fig. 3.4 (a)**. In general, the case $k_B/k_{CFF} \to 0$ represents a free-free supported rotor ($k_B \to 0$), with ω_1 being the rigid body mode frequency that approaches 0 and ω_2 the free-free resonating rotor, i.e., the bending resonance frequency. For the other extreme edge case of $k_{CFF}/k_B \to 0$ the bearing is assumed to be rigid ($k_B \to \infty$). The bending resonance frequency corresponds to ω_1 while $\omega_2 \to \infty$ represents the resonance of the rotor magnet masses m_B on the magnetic bearing, which is virtually uninfluenced by the blades' stiffness k_{CFF}.

The parameters of the rigid CFF rotor listed in **Tab. 3.1** are applied to the *mkd*-model, resulting in the rigid body mode at $\omega_1 = 1920$ rpm and the bending resonance mode at $\omega_2 = 6130$ rpm (see **Fig. 3.4 (b)** and **Fig. 3.4 (c)**).

Tab. 3.1: *mkd*-model parameters of the CFF rotor.

		Bearing (B)		CFF rotor (CFF)
mass (kg)	m_B	0.4	m_{CFF}	0.22
stiffness (N/m)	k_B	21'000	k_{CFF}	20'000
damping (Ns/m)	d_B	10	$d_{i,CFF}$	0.01

The mode shape of ω_1 is illustrated in **Fig. 3.4 (d)**, which represents the resonance frequency of the magnetic bearing, i.e., the rigid body mode, where

the rotor would deflect from its rotational axis without bending. The rigid body mode does not pose a problem for the operation of the CFF due to the implementation of a force-rejection algorithm in the position controller of the drive, which prevents the unbalance force from exciting this mode [50].

The mode shape of ω_2 depicts the bending of the CFF blades. The CFF blades with heavy rotor magnets mounted on each end can lead to displacements big enough to cause plastic deformation of the CFF blades. This results in permanent damage of the rotor, which strictly limits the directly coupled CFF rotor to subcritical use below ω_2.

3.2.3 Unbalance Response of CFF with Decoupled Rotor Magnets

For the CFF rotor with mechanically decoupled rotor magnets, the resonance frequencies are evaluated depending on the ratio between the decoupling element stiffness k_{dE} and CFF blades stiffness k_{CFF}. For the simulation, the magnetic bearing stiffness k_B, which according to **Eq. (3.1)** depends on the force/current and force/displacement constants, defined by the motor topology, and the variable position control parameter P, is set to a fixed value, which results in stable motor operation.

The system response is shown in **Fig. 3.5** and the measured CFF rotor parameters are listed in **Tab. 3.2**. The stiffness ratio $k_{CFF}/k_{dE} \to 0$ represents the case $k_{dE} \to \infty$, which is again the rigidly mounted CFF rotor with $\omega_1 = 1920$ rpm, $\omega_2 = 6130$ rpm and $\omega_3 \to \infty$ from **Sec. 3.2.2**.

To simulate the decoupling between CFF blades and rotor magnets, the stiffness ratio of $k_{dE}/k_{CFF} = 0.5$ is applied to the *mkd*-model. The amplitude and phase of deflection of an unbalance excitation to this system are then evaluated at the magnetic bearing $\hat{x}_B$, the CFF blades edge $\hat{x}_{CFF,e}$ as well as center $\hat{x}_{CFF,c}$ (see **Fig. 3.6 (a)–(c)**) and result in mode shapes of **Fig. 3.6 (d)**.

The simulation results reveal, that the resonance frequencies of $\omega_1 = 1770$ rpm and $\omega_2 = 3270$ rpm shift downwards, compared to the resonance frequencies from the CFF rotor from **Sec. 3.2.2**.

At ω_1, the rotor magnets and CFF blades deflect (in phase) from their initial position, whereby the CFF blades remain almost undeformed throughout their length. The mode shape of ω_2 differs in the phase-shift between the deflection of the rotor magnets and CFF blades. At these rotational speeds, the unbalance forces cause high elastic deformation of the decoupling elements and much lower elastic deformation of the CFF blades, since the decoupling elements possess a lower mechanical stiffness ($k_{dE} < k_{CFF}$). Hence, the critical
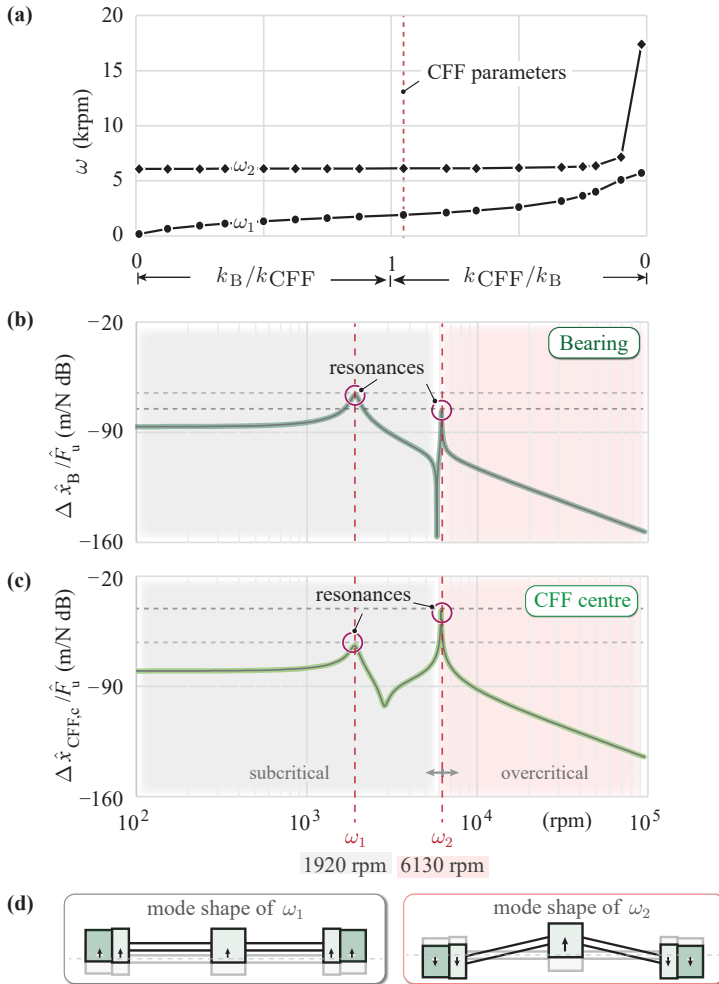
Fig. 3.4: Unbalance response of CFF$_{\text{fix}}$. **(a)** From the rigidly mounted CFF *mkd*-model ($k_{\text{dE}} \to \infty$) resulting systems' resonance frequencies ω_1 and ω_2 depending on the stiffness ratio between the magnetic bearing k_B and CFF blades stiffness k_{CFF}. Unbalance force response of the rotor to an unbalance force excitation $F_u(t)$ evaluated at **(b)** the magnetic bearing $\hat{x}_B$ and **(c)** CFF center $\hat{x}_{\text{CFF}}$. The bending mode ω_2 is determined at 6130 rpm. **(d)** Conceptual drawings of the mode shapes show the bending of the CFF blades at ω_2, which is the limiting factor for high-speed operation.

Tab. 3.2: *mkd*-model parameters of the CFF rotor with decoupling elements.

	Bearing (B)		Decoupling element (dE)		CFF rotor (CFF)	
mass (kg)	m_B	0.4	–		m_{CFF}	0.22
stiffness (N/m)	k_B	21 000	k_{dE}	10 000	k_{CFF}	20 000
damping (Ns/m)	d_B	10	–		$d_{i,CFF}$	0.01
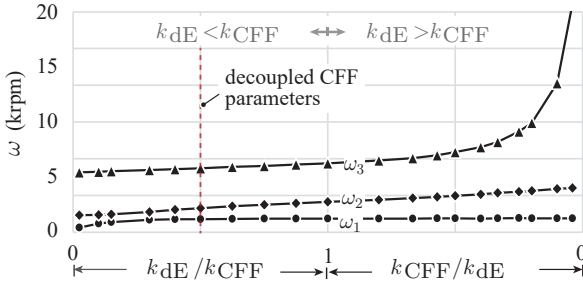
Fig. 3.5: From the decoupled CFF *mkd*-model resulting systems' resonance frequencies ω_1, ω_2 and ω_3 depending on the stiffness ratio between the decoupling element stiffness k_{dE} and the CFF blades stiffness k_{CFF}.

resonance frequencies ω_1 and ω_2 can be passed. The speed range above these frequencies is considered supercritical, since the CFF rotor self-centers and allows a stable operation up to the third resonance frequency.

The third resonance frequency ω_3 occurs at 8700 rpm and is associated with the detrimental bending of the CFF blades. It is mainly driven by the stiffness k_{CFF}, which cannot be further modified than what the fluid dynamic design requirements to the blade geometry allow for. Since plastic deformation only occurs when approaching ω_3, the new speed limit is increased by 42 % compared to ω_2 of the rotor with rigidly mounted rotor magnets.
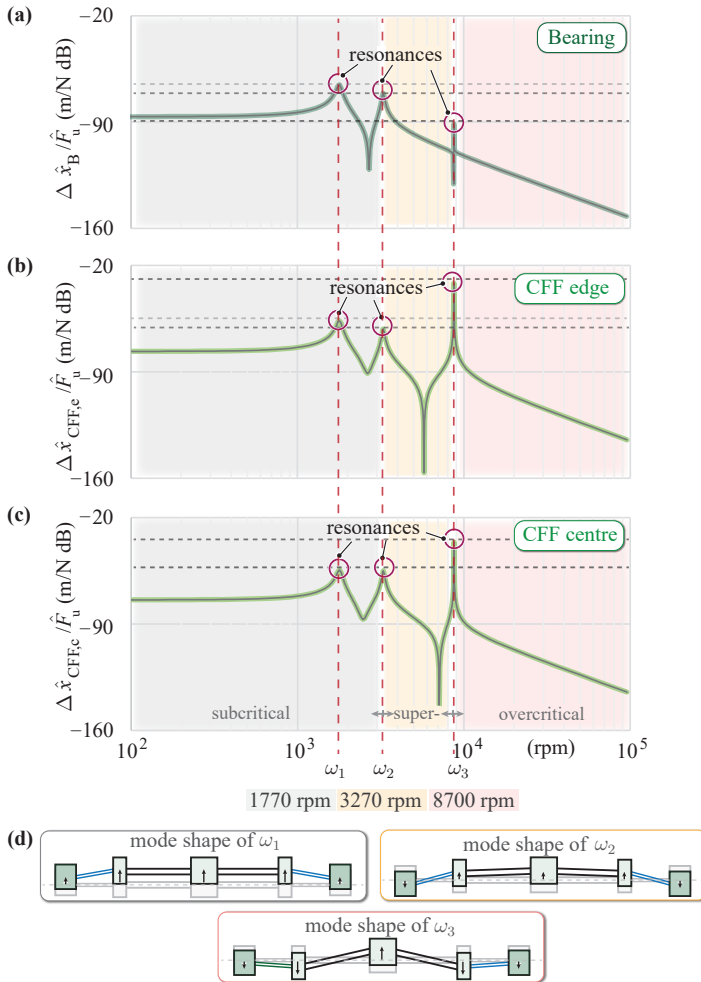
Fig. 3.6: Unbalance force response of the rotor to an unbalance force excitation $F_u(t)$ evaluated (**a**) at the magnetic bearing $\hat{x}_B$, (**b**) CFF edge $\hat{x}_{CFF,e}$ and (**c**) CFF center $\hat{x}_{CFF}$. The resonance frequency at which the CFF blades bend is determined at 8700 rpm. (**d**) Conceptual drawings of the mode shapes show the bending of the CFF blades at ω_3, which is the limiting factor for high-speed operation.

3.3 Experimental Investigation of Decoupling Elements

The experimental investigation is conducted for different decoupling elements between the CFF blades and the rotor magnets, to examine their influence on the magnetic bearing, which can only compensate for forces and allow displacements to a limited extent. The aim is to determine with which decoupling element the rotor can be operated at the highest rotational speeds. Moreover, the performed rotor dynamic measurements are compared with the simulation results. These measurements are conducted without the influence of any fluid dynamic loads; therefore, the CFF blades are covered. The rotor magnet displacements in the magnetic bearing are measured using built-in sensors in the bearingless motor 1 (BM1) and 2 (BM2). For the CFF blade displacements $\hat{x}_{CFF,e}$ and $\hat{x}_{CFF,c}$, laser-based distance sensors S1, S2, and S3 are employed to verify the expected mode shapes.

3.3.1 Influence of the Decoupling Elements on Resonance Frequencies

Seven different decoupling elements are characterized and tested, which leads to the parameters and measured resonance frequencies summarized in **Tab. 3.3**. The respective bending stiffnesses $k_{dE,i}$ are determined by a force-displacement measurement. All decoupling elements consist of the same rubber material and solely vary in their diameter and length.

Tab. 3.3: Characteristic parameters and measured resonance frequencies of the tested decoupling elements dE_1 to dE_7.

	i (−)	$k_{dE,i}$ (N/mm)	$m_{dE,i}$ (g)	$\frac{k_{dE,i}}{k_{CFF}}$ (−)	$\frac{k_{dE,i}}{k_{CFF}}\frac{m_{CFF}/4}{m_{dE,i}}$ (−)	$\omega_{1,dE,i}$ (rpm)	$\omega_{2,dE,i}$ (rpm)	$\omega_{3,dE,i}$ (rpm)
(a)	−	−	−	−	−	−	5800	−
(b)	1	16	35	0.80	1.26	3000	6100	−
(c)	2	12.5	51	0.63	0.67	2300	4600	−
(d)	3	10.5	94	0.53	0.31	1900	3500	7400
(e)	4	9.4	60	0.47	0.43	1900	3700	8400
(f)	5	9	43	0.45	0.58	2000	4300	8300
(g)	6	4.9	37	0.25	0.36	1700	3600	8000
(h)	7	4.4	54	0.22	0.22	1400	2800	7600

The measured radial rotor displacements in the magnetic bearing for the CFF with rigidly mounted rotor magnets are shown in **Fig. 3.7 (a)** and serve as a reference measurement. The rigid body mode does not pose a problem for the magnetic bearing. However, a rapidly increasing radial displacement is measured for BM1 and BM2 when approaching the bending resonance frequency. The unbalance forces lead to a plastic deformation of the CFF blades, therefore it is not possible to pass approximately 5800 rpm.

The rotor dynamic measurements are performed for seven decoupled CFF rotors (**Fig. 3.7 (b)–(h)**). Auxiliary touch-down bearings prevent a possible collision between the CFF blades and the static CFF casing walls when passing the first two resonance frequencies.

The aim is to find the decoupling element with the best trade-off between a low enough stiffness k_{dE}, such that the CFF blades do not plastically bend at the second resonance frequency, but a high enough stiffness to shift ω_3 to higher frequencies. Additionally, the mass of the decoupling element should be low to prevent extra mass in the rotor, which leads to a reduction in ω_3. Furthermore, a high enough k_{dE} is required for the rotor to withstand the fluid dynamic forces created by the CFF blades.

The results from **Fig. 3.7 (b),(c)** show that with decoupling elements dE_1 and dE_2 the target of supercritical operation is not achieved, because their stiffnesses $k_{dE,1}$ and $k_{dE,2}$ are too high. The magnetic bearing is not able to compensate for the forces when approaching the resonance frequencies $\omega_{2,dE,1}$ and $\omega_{2,dE,2}$.

The remaining decoupling elements are successfully operated in the supercritical speed region (**Fig. 3.7 (d)–(h)**). It can be seen that decoupling element dE_3 has the lowest resonance frequency ω_3; therefore, it reached the lowest maximum speed. This can be justified by its large mass, which is almost 40 % higher compared to the second heaviest supercritically operated element.

The measurements further show that decoupling element dE_4 reaches the highest rotational speed. It offers the best trade-off between a low enough stiffness $k_{dE,4}$ to successfully operate in the supercritical region, and at the same time a high enough stiffness and low mass $m_{dE,4}$, which leads to the highest frequency of ω_3 in this study.

3.3.2   Influence of Decoupling Elements on Mode Shapes

The different mode shapes and the supercritical self-centering effect of the decoupled CFFs are further verified with laser distance measurements on the CFF blades, which are summarized in **Fig. 3.8**. The results of the CFF
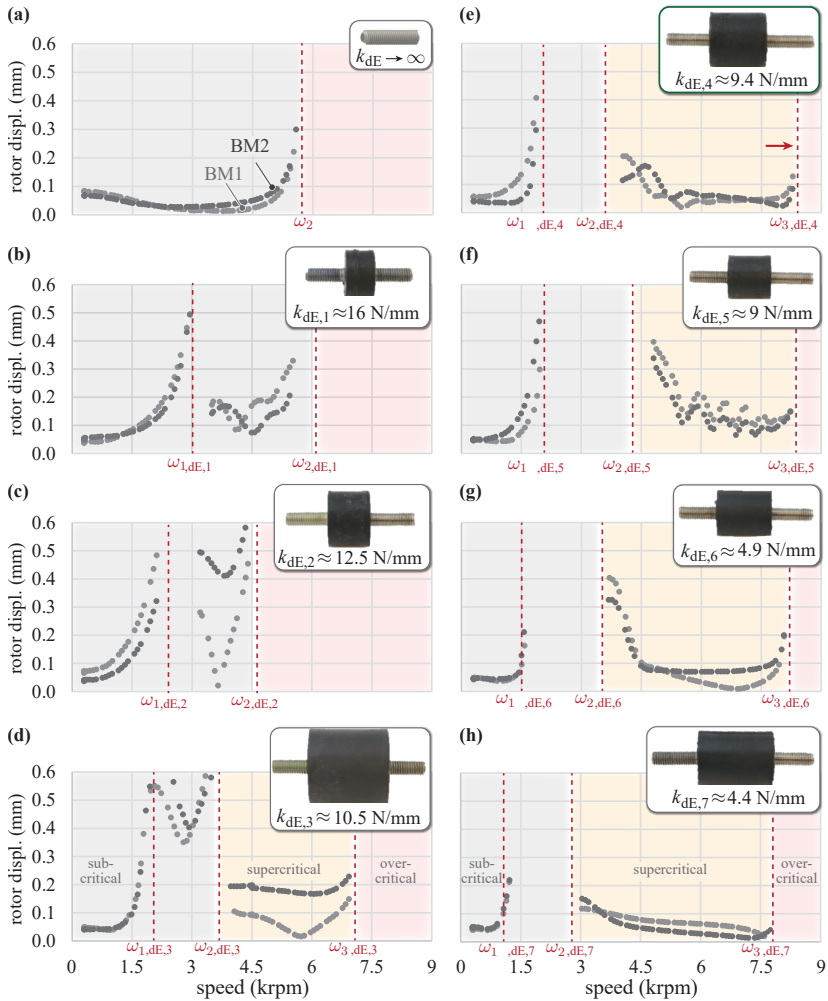
Fig. 3.7: The measured radial rotor displacements in the magnetic bearing are shown in (**a**) for the CFF rotor with rigidly mounted rotor magnets and in (**b**–**h**) for different decoupled CFF rotors. The decoupling element dE$_4$ from measurement (**e**) results in the highest speed increase of 45 % compared to (**a**).

with rigidly mounted rotor magnets confirm that the CFF blades start to bend with increasing speed. In the vicinity of the bending resonance frequency, the low bending stiffness of the CFF blades allows the unbalance forces to cause plastic deformation of the blades up to 6 mm (see **Fig. 3.8 (a)**), thus preventing the passing of the resonance frequency.

The displacements of the CFF rotor with decoupling element dE_4 are measured with the same sensor setup at different rotational speeds. The CFF blades deflect in-phase and out-of-phase with respect to the rotor magnets close to the first and second resonance frequencies, respectively. Additionally, an elastic deformation is measured after the second resonance is passed. The plastic deformation of the CFF blades occurs towards the third resonance frequency ω_3 (see **Fig. 3.8 (b)**).

Furthermore, the bearing currents are evaluated at subcritical speeds of 1500 rpm (close to ω_1), at 4200 rpm (shortly after ω_2) and at 6000 rpm (supercritical operation) as seen in **Fig. 3.8 (b1),(b2),(b3)** . The phase shift of 180° between the bearing currents at 1500 rpm and 4200 rpm demonstrates that the force on the magnetic bearing acts in opposing directions. This confirms the phase-shifted deflections of mode shapes ω_1 and ω_2. From the bearing current at 6000 rpm, a stable supercritical speed operation is detected, clearly showing the self-centering effect of the rotor from ω_2 onward.

3.3.3 Comparison and Verification of the *mkd*-Model

The measured resonance frequencies of the rotors fitted with decoupling elements dE_1 to dE_7 are plotted on the simulation results from **Sec. 3.2.3** with respect to the stiffness ratio of the decoupling element stiffness and the CFF bending stiffness ($k_{dE,i}/k_{CFF}$) in **Fig. 3.9 (a)**. To eliminate the effect of the decoupling element's mass, which has been neglected in the *mkd*-model, the measured resonance frequencies are plotted with respect to the mass-compensated stiffness ratio $k_{dE,i}/k_{CFF} \cdot \frac{m_{CFF}/4}{m_{dE,i}}$ in **Fig. 3.9 (b)**. Comparing the experimental data with the simulation results, it can be seen that the resonance frequencies ω_1, ω_2 and ω_3 increase with increasing decoupling element stiffness $k_{dE,i}$ for both the experimental data and the simulation results. The resonance frequency ω_3 features the lowest slope. The mass compensation method leads to a better fit between the theory and measurements according to **Fig. 3.9 (b)**. The deviation between simulated and measured resonance frequencies is explained by the approximated model parameters, e.g., the stiffness values have been measured by simplified force-displacement measurements. Additionally, the measured resonance frequencies have to be
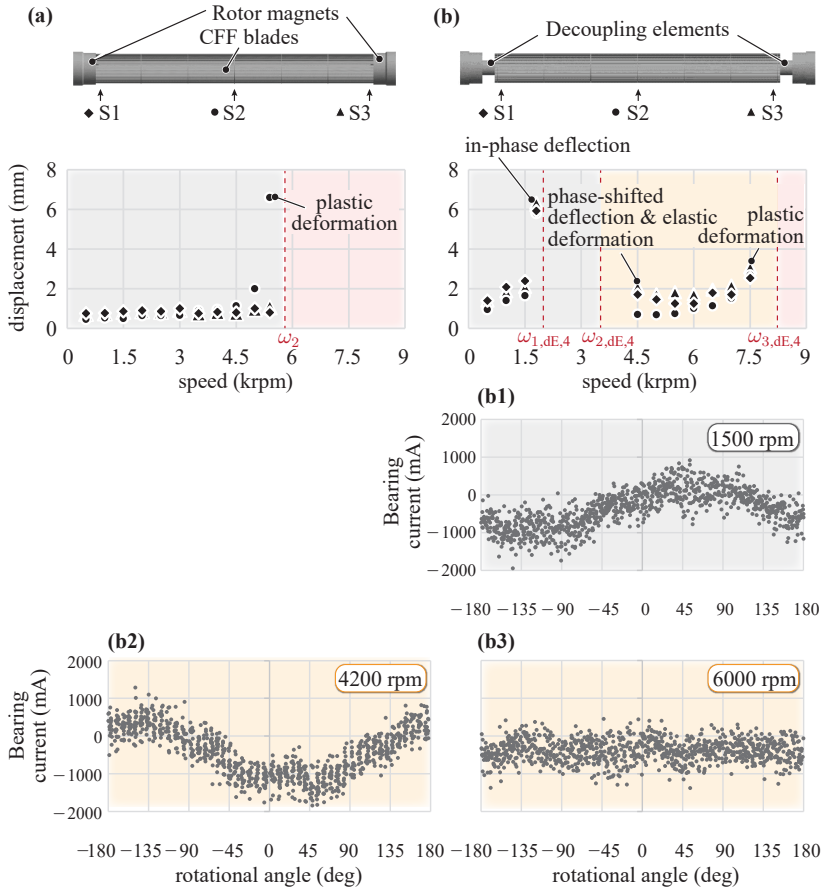
Fig. 3.8: Laser distance sensor measurements of (**a**) the CFF rotor with rigidly mounted rotor magnets and (**b**) the CFF rotor with decoupling element dE4. Measured bearing currents at (**b1**) subcritical speed 1500 rpm and (**b2**) supercritical speeds 4200 rpm and (**b3**) 6000 rpm, respectively. The 180° phase-shift between the sub- and supercritical bearing currents shows the phase-shifted deflections of mode shape ω_1 and ω_2. The self-centering effect can be seen from the decrease in the bearing current's amplitude from 4200 rpm to 6000 rpm.
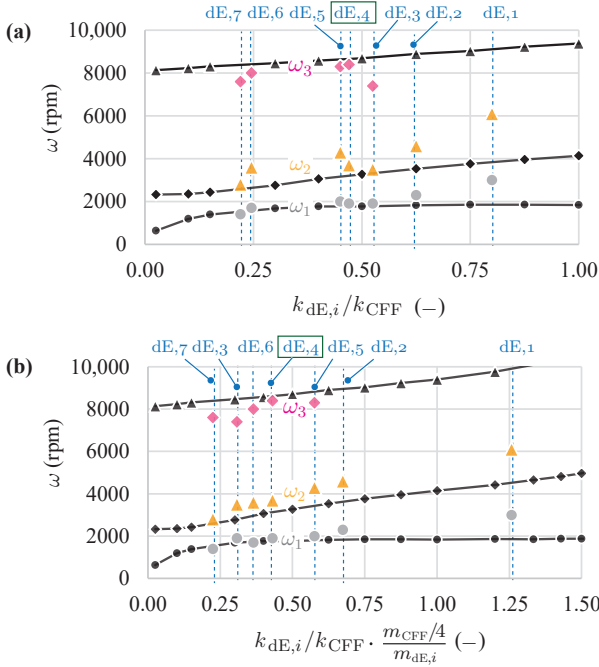
Fig. 3.9: Measured and simulated resonance frequencies of CFF rotors with decoupling element dE_i plotted with respect to the **(a)** stiffness ratio $k_{dE,i}/k_{CFF}$ and **(b)** mass-compensated stiffness ratio $k_{dE,i}/k_{CFF} \cdot \frac{m_{CFF}/4}{m_{dE,i}}$.

estimated in their vicinity, since the rotor cannot be operated in the resonance itself due to resulting mechanical damages.

In summary, this section demonstrates the validity of the rotor dynamical study for CFF rotors with rigidly mounted rotor magnets as well as the introduced, decoupled rotors. A stiffness ratio between k_{dE}/k_{CFF} of 0.47, i.e., dE_4, leads to the highest achievable rotational speed of the tested decoupling elements. It offers the best trade-off between a "soft" enough decoupling, to be able to penetrate the supercritical region and at the same time a "stiff" enough decoupling element, to shift the third resonance frequency to higher rotational speeds. This leads to an increase in the critical bending resonance frequency from 5800 rpm (rigidly mounted rotor magnets to CFF blades) to 8400 rpm (decoupled rotor with dE_4), which is an increase of 45 %. The CFF rotor with decoupling element dE_4 assures a stable operation with low mag-
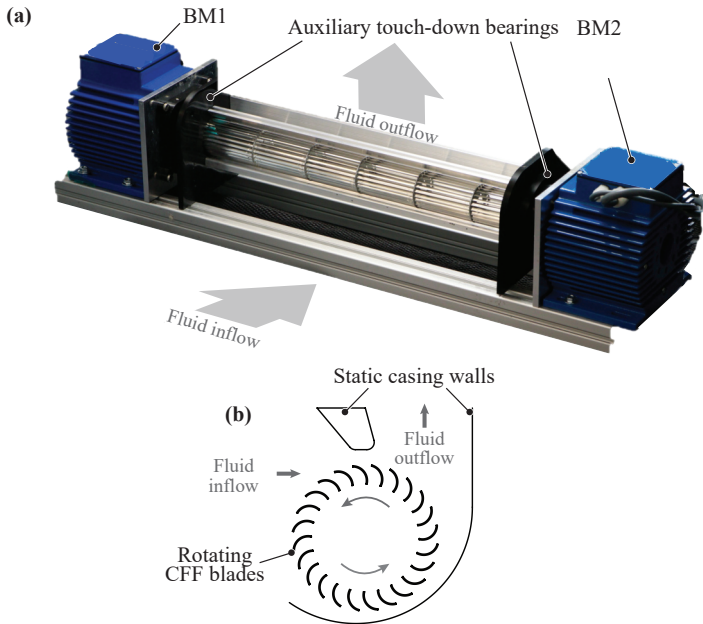
Fig. 3.10: The bearingless CFF for fluid dynamic operation: **(a)** Image of decoupled, bearingless CFF system including auxiliary touch-down bearings. **(b)** Schematics of CFF with rotating CFF blades and static casing walls, where the gap between them should be small for an optimized fluid dynamic performance, however, large enough to prevent contact even at the maximum blades' deflection.

netic bearing currents in the supercritical speed region up to 7000 rpm with a safety margin of 17 % from the critical resonance frequency ω_3.

3.4 Pressure-Flow Characteristics of Decoupled CFF-Rotor

The influence of decoupling the CFF rotor on the fluid dynamic performance is presented in this section. Due to the decoupling elements, the rotor can be operated in the supercritical region of rotational speed up to 7000 rpm. Air flow and pressure measurements in this expanded operation range are performed with the decoupled CFF rotor.

Fig. 3.10 (a) shows the image of the decoupled, bearingless CFF system and **Fig. 3.10 (b)** the cross-sectional view of the CFF. The rotating CFF blades are surrounded by static casing walls. They are placed close to the rotating fan blades for optimal fluid dynamic performance, but the gap is large enough such that the blades avoid contact with the housing even at the maximum deflection. To prevent a possible collision between the blades and the casing walls when passing the first two resonance frequencies, touch-down bearings are installed in the casing wall on each side of the rotor.

Fig. 3.11 (a) shows the resulting pressure-flow curves of the decoupled, supercritically operated rotor $CFF_{dE,4}$ and the subcritically operated CFF with rigidly mounted rotor magnets, which have been performed on a standardized test setup [50]. The measurements marked in blue show the performance at the speed maximum of 7000 rpm, 17 % below the third resonance frequency expected at 8400 rpm. The previously highest rotational speed of the directly coupled CFF at 5000 rpm is marked in gray, which is 14 % below the expected bending resonance frequency of 5800 rpm.

Comparing the performance at 5000 rpm of the directly coupled and decoupled CFF, a decrease in flow rate of 10 % is noticed (light blue arrow). This can be justified with a reduced active CFF blade length since for the decoupled CFF, auxiliary touch-down bearings are installed as a safety measure. Therefore, the 40 % increase in rotational speed results in an overall increase in fluid flow of 28 % and an increase in pressure of 100 %.

Analyzing the measured radial rotor displacements in the magnetic bearing of the CFF rotor under fluid dynamic loads (**Fig. 3.11 (b)**), it can be concluded that a stable operation is possible up to 7000 rpm due to the self-centering effect of supercritical operation and that the fluid dynamic forces only cause small displacements in the magnetic bearing.
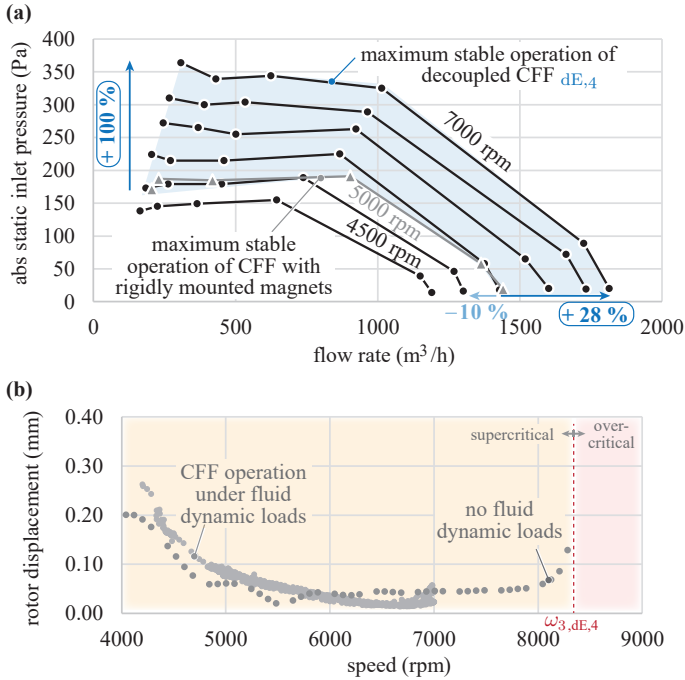
(a)

(b)

Fig. 3.11: Experimental measurements of bearingless CFF during fluid dynamic operation. **(a)** Pressure-flow curves for decoupled, supercritically operated rotor $CFF_{dE,4}$ and subcritically operated CFF with rigidly mounted rotor magnets. The maximum achieved performance is marked in blue for the decoupled and in gray for the coupled rotor, respectively. **(b)** Measured radial rotor displacements in the magnetic bearing of the magnets of BM1 for $CFF_{dE,4}$ under fluid dynamic loads and without any fluid dynamic loads. The fluid dynamic forces only cause small displacements in the magnetic bearing. The CFF is operated up to 7000 rpm with a safety margin of 17 % from the critical resonance frequency ω_3.

3.5 Summary

The presented method of decoupling the rotor magnets of bearingless CFFs with mechanical elements of lower bending stiffness compared to the CFF blades, results in an increase in rotational speed and fluid dynamical performance. It is shown, that the blade damaging resonance is shifted to higher frequencies, enabling higher rotational speeds due to the self-centering effect

55

of the rotor. This results in a 40 % speed increase and leads to an increase in fluid flow of 28 % and an increase in pressure of 100 % compared to the previously presented bearingless CFF without decoupling elements.

To achieve a high-speed and high-performance bearingless CFF, the challenge is to increase the rotational speed with measures, that do not negatively impact the fluid dynamic performance.

Methods to increase the rotors' mechanical stiffness and thus the achievable speed, e.g., through design adaptations such as thicker blades or axial rods for rotor stiffening, mostly result in lower fluid performance. Nevertheless, our approach still allows us to expand the CFF design with measures to increase the CFF blades' stiffness.

To the authors' knowledge, there is no comparable control strategy for bearingless motors to pass the bending resonance frequency without the risk of damaging the CFF blades, especially due to their unique mass distribution and bending stiffness. In comparison, the presented approach shifts the blade damaging resonance frequency to higher rotational speeds, hence ensuring that the rotor does not have to be operated in its vicinity or even to pass it.

In summary, the presented method offers a space-saving, simple yet effective mechanical design approach to increase the bearingless' CFFs fluid dynamic performance.

<div style="text-align: right; font-size: 3em;">4</div>

CFD Based Optimization of High-Speed and High-Performance Bearingless Cross-Flow Fan Designs

This chapter summarizes the most relevant findings on optimizing the CFF rotor and static casing walls to enhance the performance of CFFs, as also published in:

▶ I. Bagaric, D. Steinert, T. Nussbaumer and J. W. Kolar, "CFD Based Optimization of High-Speed and High-Performance Bearingless Cross-Flow Fan Designs," *Machines*, vol. 12(8), no. 513, July 2024.

Chapter Abstract

To enhance the fluid dynamic performance of bearingless cross-flow fans (CFFs), this chapter presents a CFD-based optimization of both rotor and static casing wall modifications. The goal for the investigated rotor modifications is to enhance the CFF's mechanical stiffness by integrating reinforcing shafts, which is expected to increase the limiting bending resonance frequency, thereby permitting higher rotational speeds. Additionally, the effects of these rotor modifications on the fluid dynamic performance are evaluated. For the casing wall modifications, the goal is to optimize design parameters to reduce losses. Several numerical simulations are conducted and validated using various commissioned prototypes, each measuring 600 mm in length and 60 mm in outer diameter. The results reveal that integrating a central shaft increases the rotational speed by up to 42 %, from 5000 rpm to 7100 rpm, due to enhanced CFF stiffness. However, the loss in fluid flow amounts to 61 % and outweighs the gain in rotational speed. Optimizing the casing walls results in a 22 % increase in maximum fluid flow reaching 1800 m^3/h at 5000 rpm.

4.1   Introduction

Cross-flow fans (CFFs) as a type of fan turbomachinery, are characterized by their large length-to-diameter ratio and ability to generate a primarily uniform flow along their length at low rotational speeds and low noise emission. Therefore, they are predominantly employed in heating, ventilation, and air conditioning (HVAC) systems. However, the application scope of CFFs extends to industrial applications such as highly specialized laser modules in the semiconductor industry. These applications require high CFF performance to maintain consistent and high-quality laser output through the gas circulation system. In [50], the authors presented the bearingless CFF, which allows for wear- and friction-free CFF operation inside a hermetically sealed chamber with high-speed capability, supported by high drive power available on both rotor sides. To enhance the fluid dynamic performance of bearingless CFF's within a given, constrained installation space (as shown in **Fig. 4.1 (a)**), this chapter conducts a Computational Fluid Dynamics (CFD) based design optimization supported and verified by measurements. On the one hand, design measures are investigated to increase the CFF's mechanical strength through introducing stiffness increasing shafts. This shifts the critical bending resonance frequency, which currently limits the maximum achievable rotational speed, to a higher frequency, thus enabling stable CFF operation at increased rotational speeds. On the other hand, design changes of the CFF casing walls are evaluated to improve its fluid dynamic performance, particularly to reduce recirculation losses between the rotating blades and the static casing walls. The investigated design measures are depicted in **Fig. 4.1 (b)**.

In industrial applications such as deep ultraviolet (DUV) lithography systems, CFFs are part of the gas circulation system. DUV lithography systems use short-wavelength ultraviolet (UV) light, typically provided by an argon fluoride (ArF) or krypton fluoride (KrF) excimer laser, to project intricate patterns onto silicon wafers for the precise fabrication of semiconductor devices. CFFs, with their cylindrical shape and tangential flow direction, are compactly integrated within the limited space constraints of the excimer laser to uniformly circulate and cool the laser gas [8, 18, 20]. Increasing the CFF's performance can positively impact various aspects of laser performance, including cooling efficiency, gas circulation, flow stability and reliability, which contributes to achieving consistent and high-quality laser output. Hence, increasing the CFF's performance is a direct enabler for improving the excimer laser's performance.
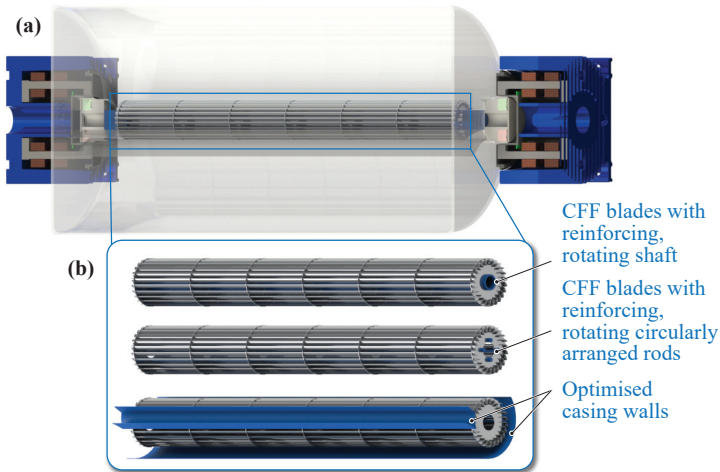
Fig. 4.1: (a) Schematic view of the bearingless CFF system in a hermetically sealed laser chamber. **(b)** Investigated measures to increase the CFF's performance through additional mechanical elements (shaft and circularly arranged rods) to increase its mechanical strength and thereby its rotational speed and through optimization of the casing walls.

To increase the CFF's performance by increasing its rotational speed, the bending resonance frequency emerges as a critical factor, since CFFs typically consist of long, slender blades that are prone to bending vibrations. When the rotational speed approaches or exceeds the bending resonance frequency, it can lead to significant structural vibrations and potentially cause mechanical damage to the CFF blades. In [73], the authors proposed a method to shift the detrimental bending resonance frequency to higher frequencies through the design of a novel CFF rotor. The rotor features additional mechanical decoupling elements with low bending stiffness, allowing resonance frequencies to be surpassed without causing damage to the CFF blades and enabling rotor operation at a 40 % higher rotational speed. Moreover, with magnetic bearings, it becomes feasible to implement complex control algorithms to actively control specific vibration modes. This offers the capability to dampen, bypass, or eliminate resonance frequencies, such as the bending resonance frequency. In literature, different approaches are investigated, typically for massive shafts and Jeffcott rotors. In [55], an optimum compensator control design method is proposed to obtain the minimum resonance peak of the rotor when passing the first bending critical speed. To operate a maglev motor

59

above the bending critical speed, [74] designed a μ−synthesis controller and experimentally verified that the rotor passes through the first bending mode frequency. A μ−synthesis controller was designed by [75] as well, to achieve active damping of the rotor's bending mode and pass through its critical speed. Using a mixed PID control method based on mode separation, [76] showed by simulation that the flexible rotor can pass the first bending critical speed.

This chapter examines two additional methods for enhancing the CFF's performance that can be implemented alongside the previously mentioned damping techniques. From a fluid dynamical point of view, the CFF's non-axisymmetric flow profile is defined by the transverse, double passage of the fluid through the rotating blades and the formation of an eccentric vortex within the impeller. There is not yet a general approach or analytical description to accurately model the aerodynamic features and loss mechanisms of CFFs, nor to precisely predict their performance. Several different investigations about CFFs were conducted using analytical modeling, numerical simulation and experimental data. To analytically determine the CFF performance curves for a given geometry, [42, 77, 78] used the mean streamline analysis with empirical data. Numerous numerical and experimental studies have been conducted, to analyze the influence of the CFF blades' [44, 79] and casing walls geometry [80–83] on the CFF performance. A particular focus lies on visualizing the complex flow patterns by means of CFD and to analyze the velocity vectors and pressure gradients, to draw conclusions about CFF performance, efficiency and loss mechanisms [51, 52, 84]. In [85], Stereo Particle Image Velocimetry (SPIV) is presented as an experimental flow visualization technique to examine the influence of CFF casing geometries. In a recently published review paper on the performance and efficiency of CFFs [86], it is concluded that optimizing and enhancing their performance remains a challenging task. To boost the CFF's efficiency, it is crucial to improve their structural characteristics, aerodynamic properties, and acoustic behavior.

Increasing the performance of bearingless CFFs presents several challenges concerning fluid dynamics, rotor dynamics (mechanical strength and rotor vibrations) and the influence on the magnetic bearing. The fluid forces can lead to displacements of the magnetically levitated rotor, requiring measures to prevent collisions with the static casing walls by maintaining a certain safety distance. The goal of this chapter is to optimize the CFF performance in terms of output pressure and flow, while considering the different effects on the bearingless motor system.

The chapter is organized as follows: **Sec. 4.2** presents the methods used for the CFF rotor and casing wall optimization including the fundamental aerodynamics, implemented CFD model, simulated modal analysis and measurement setup. **Sec. 4.3** reveals and discusses the results for the different rotor and static casing walls design modifications. **Sec. 4.4** summarizes the main conclusions.

4.2 Methods for CFF Analysis

4.2.1 Fundamental Aerodynamics

This section explains the operating principle of CFFs from a fluid dynamical point of view, particularly to underline the loss mechanisms associated with the characteristic eccentric vortex. The goal of this analysis is to explore methods for enhancing the performance of the CFF by modifying both the rotor and static casing walls within given space constraints. Regarding the rotor modifications, the primary focus is on increasing mechanical stiffness through the integration of reinforcing shafts and evaluating their impact on fluid dynamic performance. In terms of the static casing walls, the emphasis is on optimizing the eccentric vortex region to reduce recirculation losses.

Generally, the energy increase of a fan turbomachinery represents the change in energy of the fluid passing through the fan from the inlet to the outlet side, i.e. from the suction to the discharge region. This energy increase is typically defined in terms of total pressure $\Delta p_{\text{th}\infty}$ and can be expressed as the sum of both static and dynamic pressure components as the first form of Euler's fluid machine equation

$$\Delta p_{\text{th}\infty} = \frac{\rho}{2} [\overbrace{(c_2^2 - c_1^2)}^{\text{dynamic}} + \overbrace{(w_1^2 - w_2^2) + (u_2^2 - u_1^2)}^{\text{static}}], \qquad (4.1)$$

where c is the absolute, u the circumferential, and w the relative velocity and ρ the density. The geometric sum of the circumferential and relative velocity gives the absolute velocity, which defines the second form of Euler's fluid machine equation as

$$\Delta p_{\text{th}\infty} = \rho(u_2 \cdot c_{u2} - u_1 \cdot c_{u1}). \qquad (4.2)$$

For CFFs, the flow field is predominately two-dimensional, i.e. perpendicular to the impeller axis. It is described by the fluid entering the forward

curved blades tangentially on the suction side, passing through the interior part of the impeller and then exiting the blades tangentially on the discharge side. Hence, the rotating blades are passed twice by the fluid and an eccentric vortex is formed within the impeller.
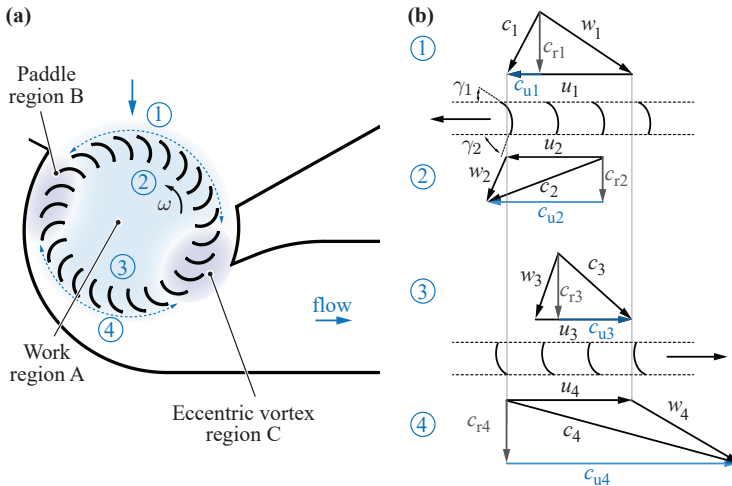

Fig. 4.2: **(a)** Flow regions of the CFF divided into the work region A, paddle region B and eccentric vortex region C adapted from [42]. **(b)** Velocity triangles in the two stages of the CFF.

To explain the fundamental kinematics and energy transfer processes for CFFs, **Fig. 4.2** is used. It is based on [42], describing in detail the through-flow and loss characteristics of the CFF by the mean streamline analysis. The analysis has the underlying assumption, that the flow within the fan can be divided into three regions (depicted as work region A, paddle region B and eccentric vortex region C in **Fig. 4.2 (a)**) and can be analyzed independently. However, the flow is strongly influenced by the operating conditions as well as the fan geometry, which can be difficult to parameterize.

The principal through-flow of the impeller is represented by region A, where the majority of the beneficial work is conducted and is described by the velocity triangles in **Fig. 4.2 (b)**. Using **Eq. (4.2)**, the ideal total pressure increase across the CFF impeller $\Delta p_{\text{th}\infty,14}$ is given by the sum of the first and second stage total pressure increase as

$$\Delta p_{\text{th}\infty,14} = \rho\Big((u_2 c_{u2} - u_1 c_{u1}) + (u_4 c_{u4} - u_3 c_{u3})\Big). \tag{4.3}$$

The actual total pressure increase $\Delta p_{\text{tot},14}$ is then given by

$$\Delta p_{\text{tot},14} = \Delta p_{\text{th}\infty,14} - \Delta p_{\text{loss}}, \tag{4.4}$$

where the pressure losses Δp_{loss} are an unknown parameter consisting of several different loss mechanisms. In [78], the most important loss models of the mean streamline analysis are summarized as skin friction, incidence expansion, enlargement and recirculation losses. As explained in [42], the CFF blades in region B act essentially like a paddle wheel, hence the energy transfer is comparatively low and inefficient. Region C represents the eccentric vortex, which consists of the recirculating flow and is primarily responsible for energy dissipation and the shaping of region A.
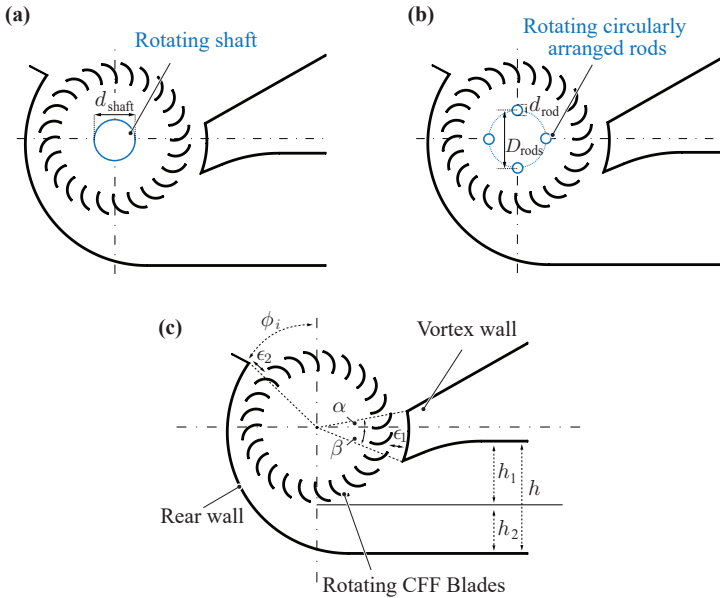

Fig. 4.3: CFFs for the CFD based performance analysis **(a)** with reinforcing rotating shafts, **(b)** with reinforcing circularly arranged rods and **(c)** parametrisation of the static casing walls including the rear and vortex wall.

From the CFFs operating principle described above, it becomes clear that introducing interior obstructions within the work region A, such as

mechanically reinforcing shafts, causes flow disturbances and additional losses. However, these stiffness increasing measures have a significant impact on the CFFs vibration behavior, especially its bending resonance frequency.

Various diameters of reinforcing shafts are studied, as depicted in **Fig. 4.3 (a)** for a single central shaft and in **Fig. 4.3 (b)** for circularly arranged rods. Regarding the casing wall optimization, its key geometric parameters are presented in **Fig. 4.3 (c)** and different variations are investigated.

4.2.2 Computational Fluid Dynamics

For the CFD analysis, planar 2D simulations are conducted, as the flow profile of the CFF remains predominantly uniform along its length. The numerical model utilized has been presented by the authors in [50]. It includes a convergence study involving mesh and time step parameters for the transient CFF CFD simulation, leading to a robust model with optimized mesh and time step settings.

Fig. 4.4 illustrates the velocity and pressure profiles resulting from the CFD simulation for the initial CFF geometry at 5500 rpm and 1633 m^3/h (high-flow point). The velocity vectors provide a visual representation of the key fluid dynamic features, highlighting the inflow and outflow regions, as well as the non-axisymmetric flow profile. Additionally, the pressure profile vividly illustrates the presence of the eccentric vortex.

For the forthcoming comparisons and performance evaluations, the dimensionless flow φ_{CFF} and pressure $\psi_{\text{stat,CFF}}$ coefficients are evaluated from the simulated physical flow Q and pressure values Δp_{stat} according to

$$\varphi_{\text{CFF}} = \frac{Q}{u \cdot d_{\text{CFF}} \cdot L_{\text{CFF}}}, \tag{4.5}$$

where d_{CFF} and L_{CFF} correspond to the CFF blades' diameter and length, and u to the circumferential velocity

$$u = \pi \cdot d_{\text{CFF}} \cdot n, \tag{4.6}$$

with n being the CFF's rotational speed and

$$\psi_{\text{stat,CFF}} = \frac{\Delta p_{\text{stat}}}{\rho_{\text{air}}/2 \cdot u^2}, \tag{4.7}$$

where ρ_{air} is the density of air. Introducing shafts within the CFF impeller changes its bending resonance frequency and can increase the rotational
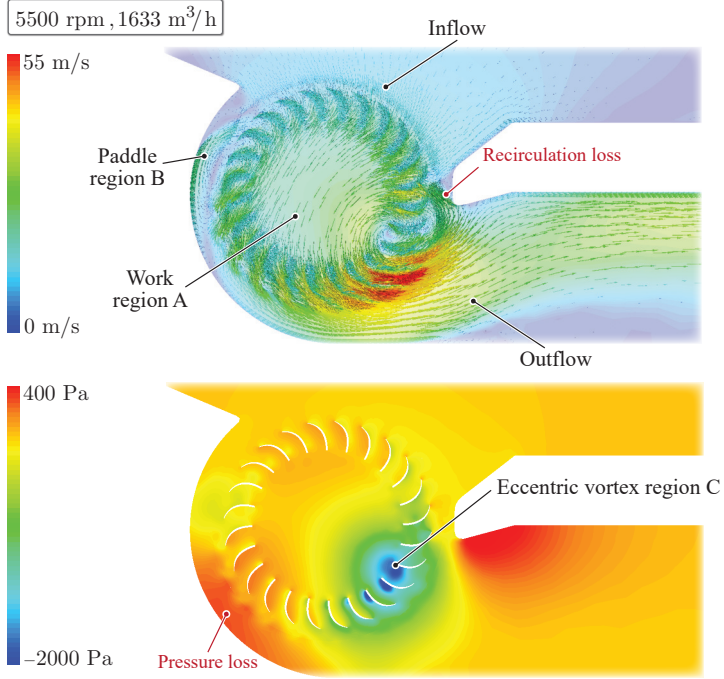
Fig. 4.4: CFD-simulated velocity (top) and pressure (bottom) profiles for the initial CFF geometry for a stable, high-flow operating point at 5500 rpm.

speed at which it can be operated. The dimensionless pressure and flow coefficients allow to extrapolate the physical pressure and flow for operating points at different rotational speeds according to

$$Q^* = \frac{n^*}{n} \cdot Q \tag{4.8}$$

and

$$\Delta p^*_{\text{stat}} = \left(\frac{n^*}{n}\right)^2 \cdot \Delta p_{\text{stat}} \tag{4.9}$$

with Q^* representing the extrapolated flow and Δp^*_{stat} the extrapolated pressure derived from the CFD results at different rotational speed n^*.

The CFD simulation is conducted for several high-flow operating points and compared to measured data points in **Fig. 4.5**. To derive the flow rate

65

from the 2D simulation, the inlet velocity is multiplied by the cross-sectional
area defined by the inlet channel's height and width. The dotted lines of the
simulated curve mark the pressure fluctuation in the CFD simulation during
the final turn, indicating convergence and a stable eccentric vortex region, i.e.
no pressure pulsations. As described in [50], an operation point converges
after approximately six turns, while one turn (a 360° rotation of the fan blades)
corresponds to 66.67 numerical time steps. It can be seen, that the simulated
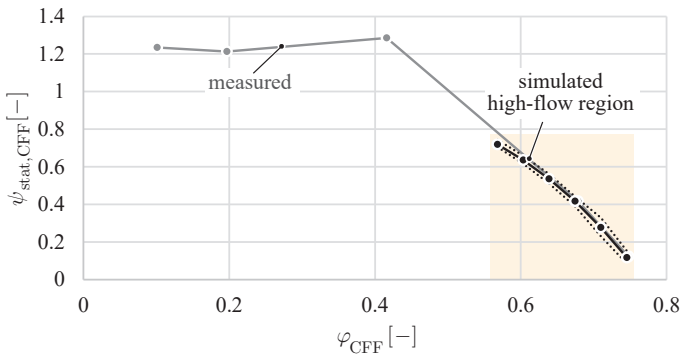and measured data points agree very well.

Fig. 4.5: Dimensionless pressure-flow curves of initial CFF geometry measured on
a test bench presented in [50] and simulated in the high-flow region. The pressure
$\psi_{\text{stat,CFF}}$ and flow φ_{CFF} coefficients are calculated according to **Eqs. (4.5)** and **(4.7)**.
The dotted lines mark the pressure fluctuation observed in the CFD simulation during
the final turn, indicating convergence and a stable eccentric vortex region.

For this study, the simulated operating points of the different design adap-
tations are focused on the high-flow regime. At low-flow operating points, the
implemented incompressible CFD model (justified with the expected subsonic
speeds of Mach numbers below 0.3) predicts strong pressure fluctuations,
which inadequately represent the physical conditions. In [45] it is observed,
that as the flow decreases, the eccentric vortex region C expands. Conse-
quently, it is more challenging for the inlet flow to efficiently penetrate work
region A of the CFF, which exacerbates the non-uniformity and amplifies the
pressure pulsations within region C. In [87] it is concluded as well, that the
dominant frequency responsible for the velocity and pressure fluctuations in
the CFF is mainly generated due to the unsteadiness of the eccentric vortex.
The flow in the low-flow region is described as strongly unsteady, unstable,
and three-dimensional in [77]. Therefore, the following simulations focus on

numerically stable, high-flow operating points, aligning with the typical CFF application for generating uniform flow patterns along their length.

To quantitatively compare the modified and initial CFF design, the simulated operating points at the same dimensionless static inlet pressure $\psi_{\text{stat,CFF}}$ are evaluated to determine the change in fluid flow as $\Delta\varphi_{\text{CFF,max}}$.

4.2.3   Simulated Modal Analysis

A modal analysis is performed on the CFF rotor modifications with various shafts to estimate the system's first bending resonance frequency, to draw conclusions about the maximum achievable rotational speed. It is described in more detail in [50]. This theoretical assessment of different shaft sizes and arrangements assists in determining which prototypes to commission.

4.2.4   Measurement Setup

The CFD simulations and experimental measurements are conducted for a CFF with $L_{\text{CFF}} = 600\,\text{mm}$ and $d_{\text{CFF}} = 60\,\text{mm}$. The pressure–flow measurements are performed with air under ambient pressure on a test rig presented in detail in [50]. It consists of an inlet ventilation duct equipped with a variable inlet grid for setting different operating points, along with a pressure and a flow sensor. Characteristic pressure-flow curves can be recorded for various design modifications.

For the rotor dynamic measurements, the displacements of the rotor magnet within the magnetic bearing are evaluated using built-in sensors in the bearingless motor. The bending resonance frequency is identified by the rapid increase in radial displacements as it is approached.

4.3   Results and Discussion

This section presents the results of the CFF analysis for different rotor and stator modifications. The quantitative results of the CFD analysis of the modified CFF rotor with reinforcing shafts (**Fig. 4.3 (a)**) and circularly arranged rods (**Fig. 4.3 (b)**) are summarized in **Tab. 4.1** and of the modified CFF static casing walls (**Fig. 4.3 (c)**) in **Tab. 4.2**, respectively.

Tab. 4.1: CFD results for the modified CFF rotor evaluated as change in fluid flow $\Delta\varphi_{\text{CFF,max}}$ compared to initial CFF geometry from **Fig. 4.4** and **Fig. 4.5**.

	Rotor modifications	Design properties	$\Delta\varphi_{\text{CFF,max}}$ (%)
(a1)	central shaft	$d_{\text{shaft}} = 12\,\text{mm}$	-44
(a2)	central shaft	$d_{\text{shaft}} = 15\,\text{mm}$	-51
(a3)	central shaft	$d_{\text{shaft}} = 20\,\text{mm}$	-61
(b1)	circularly arranged rods	$d_{\text{rod}} = 5\,\text{mm}, D_{\text{rods}} = 20\,\text{mm}$	-38
(b2)	circularly arranged rods	$d_{\text{rod}} = 5\,\text{mm}, D_{\text{rods}} = 30\,\text{mm}$	-29

Tab. 4.2: CFD results for modified CFF static casing wall evaluated as change in fluid flow $\Delta\varphi_{\text{CFF,max}}$ compared to initial CFF geometry from **Fig. 4.4** and **Fig. 4.5**.

	Static casing wall modifications	Design properties	$\Delta\varphi_{\text{CFF,max}}$ (%)
(c1)	increased inlet angle ϕ_i	$h = 43.5\,\text{mm}, h_2 = 13.5\,\text{mm},$ $\epsilon_2 = 8.6\,\text{mm}, \phi_i = 65°$	$+0$
(c2)	rear wall downward shift	$h = 48.5\,\text{mm}, h_2 = 18.5\,\text{mm},$ $\epsilon_2 = 5\,\text{mm}, \beta = 7.2°,$	$+10$
(c3)	rear & vortex wall downward shift	$h = 43.5\,\text{mm}, h_2 = 18.5\,\text{mm},$ $\epsilon_2 = 5\,\text{mm}, \beta = 14.9°$	$+15$
(c4)	optimized outlet side	$h = 47.8\,\text{mm}, h_1 = 29\,\text{mm},$ $\epsilon_2 = 5\,\text{mm}, \beta = 11.7°$	$+22$

It is shown that rotor modifications with shafts do not lead to an increase in CFF performance, whereas optimizing the casing wall results in a performance improvement of up to 22 %. A detailed analysis and discussion of the results is presented next.

4.3.1 Rotor Modifications

Reinforcing Central Shaft

For different sizes of reinforcing central shafts, denoted as designs **(a1)**, **(a2)** and **(a3)** in **Tab. 4.1**, the pressure-flow performance of the CFF significantly decreases, as depicted in **Fig. 4.6 (a)**. The evaluated change in dimensionless flow $\Delta\varphi_{\text{CFF,max}}$ corresponds to -44 %, -51 % and -61 % for shafts with diameter $d_{\text{shaft}} = 12\,\text{mm}$, $d_{\text{shaft}} = 15\,\text{mm}$ and $d_{\text{shaft}} = 20\,\text{mm}$. The simulations for the reinforcing shafts with diameters of 12 mm and 20 mm are additionally validated with pressure–flow measurements on the test bench.

Tab. 4.3: Simulated and measured resonance frequencies of CFF blades with reinforcing shafts.

$d_{shaft,out}$ / $d_{shaft,in}$ (mm)/(mm)	Material (−)	$\omega_{bend,sim}$ (rpm)	$\omega_{bend,meas}$ (rpm)
−	aluminum	7360	5800
12 / 0	stainless steel	7290	5100
15 / 11	stainless steel	8800	6300
20 / 14	aluminum	10,850	6800
20 / 16	stainless steel	11,310	8200

The velocity and pressure profiles for a shaft diameter of 12 mm are visualized in **Fig. 4.7**. It can be seen, that the presence of the shaft obstructs the flow field within the impeller, causing localized flow blockage and disrupting the formation of the eccentric vortex. Consequently, losses occur, which increase with the shaft diameter.

Furthermore, five distinct CFF prototypes featuring central reinforcing shafts are rotor dynamically analyzed. Various configurations of hollow and solid shafts, made from either stainless steel or aluminum, are tested. Their respective bending resonance frequencies are determined through modal simulation and, for the commissioned prototypes, tested on the test bench, as listed in **Tab. 4.3**. For all simulated CFF rotors, the simulation model overestimates the mechanical stiffness and consequently the first bending resonance frequency. This discrepancy arises from the multi-body nature of the prototype and the imperfect bonding between individual components, whereas in the simulation the CFF rotor is assumed as one single solid body. For a stainless steel shaft with a diameter of 12 mm, the resonance frequency $\omega_{crit,meas}$ is measured at 5100 rpm. This frequency is lower compared to the initial CFF resonance frequency of 5800 rpm, indicating that the overall increase in mass outweighs the increase in mechanical bending stiffness. The 15 mm hollow stainless steel shaft raises $\omega_{crit,meas}$ to 6300 rpm. Additionally, the 20 mm hollow aluminum and stainless steel shafts, increase $\omega_{crit,meas}$ to 6800 rpm and 8200 rpm, respectively.

With a safety margin of approximately 14 % from the critical resonance frequency as determined in [73], the dimensionless pressure–flow curves depicted in **Fig. 4.6 (a)** are extrapolated for the initial design to 5000 rpm, for
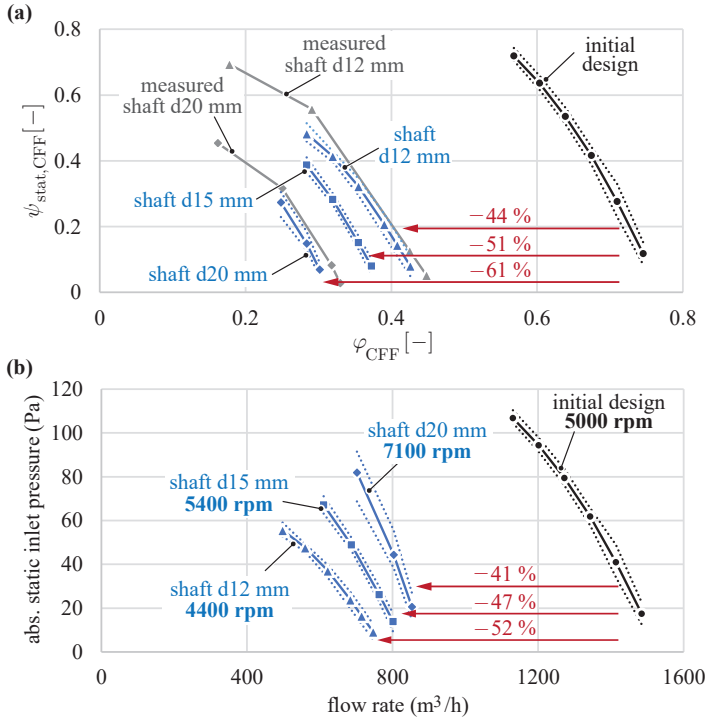
Fig. 4.6: (a) Dimensionless pressure–flow curves for the CFF rotor with reinforcing shafts simulated for shaft diameters d_{shaft} of 12 mm, 15 mm and 20 mm. The CFD results are validated for d_{shaft} of 12 mm and 20 mm with measurements on the test bench. **(b)** Extrapolated pressure–flow curves according to **Eqs. (4.8)** and **(4.9)** to the maximal possible rotational speed n^*, where n^* is determined by the resonance frequencies from **Tab. 4.3** with a safety margin of ca. 14 % as determined in [73].

a shaft diameter $d_{shaft} = 12$ mm to 4400 rpm, for $d_{shaft} = 15$ mm to 5400 rpm and for $d_{shaft} = 20$ mm to 7100 rpm according to **Eqs. (4.8)** and **(4.9)**.

It can be concluded, that even with the highest rotational speed increase of 42 % due to the enhanced stiffness of the CFF with $d_{shaft} = 20$ mm, the loss in fluid dynamic performance of -61 % outweighs the gain in rotational speed resulting in an overall performance decrease of -41 % as shown in **Fig. 4.6 (b)**.
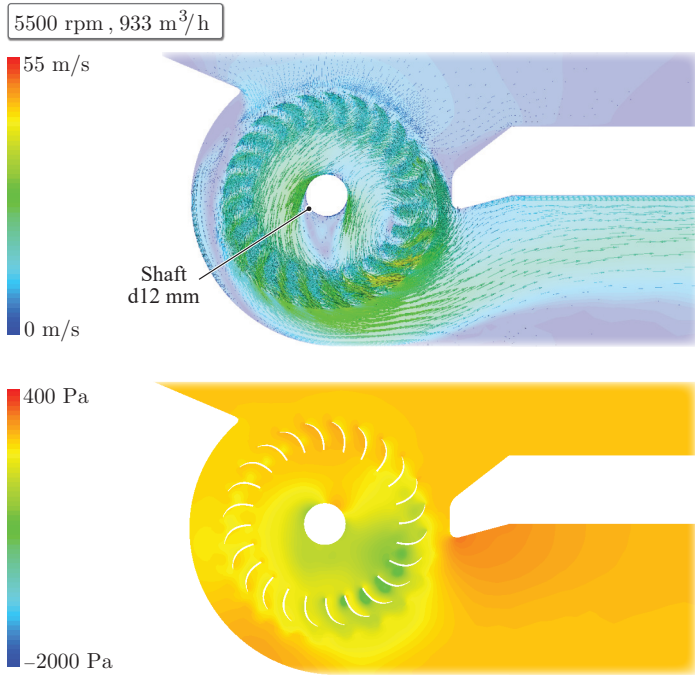

Fig. 4.7: CFD-simulated velocity (top) and pressure (bottom) profiles for the modified CFF rotor with central shaft with a diameter of 12 mm for a stable, high-flow operating point at 5500 rpm.

Reinforcing Circularly Arranged Rods

The CFD results of the dimensionless pressure–flow curves for CFFs with reinforcing circularly arranged rods are shown in **Fig. 4.8**. Similarly to the designs with central shafts, the performance decreases due to flow obstructions. The evaluated change in dimensionless flow $\Delta\varphi_{CFF,max}$ for rods of $d_{rod} = 5$ mm

corresponds to $-29\,\%$ and $-38\,\%$ arranged at diameter $D_{\mathrm{rods}} = 30\,\mathrm{mm}$ and $D_{\mathrm{rods}} = 20\,\mathrm{mm}$, respectively. Placing the rods at a larger diameter disrupts the formation of the eccentric vortex less.
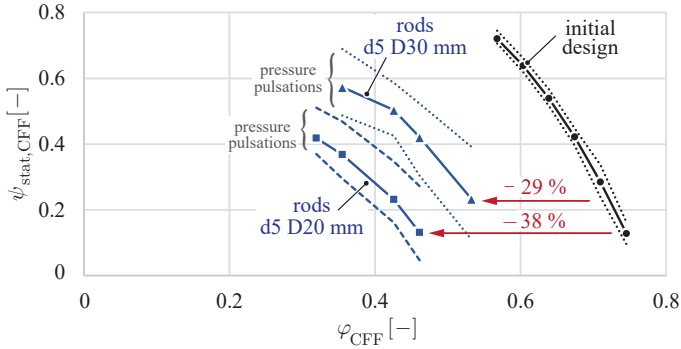

Fig. 4.8: Dimensionless pressure-flow curves for the CFF rotor with reinforcing circularly arranged rods simulated for a rod diameter $d_{\mathrm{rod}} = 5\,\mathrm{mm}$ and circle diameters $D_{\mathrm{rods}} = 20$ mm and $D_{\mathrm{rods}} = 30$ mm, respectively.

However, the rods interact with the eccentric vortex generated by the impeller blades, inducing significant pressure pulsations, as they penetrate it at a frequency four times the rotational frequency of the rotor. Consequently, the stability and uniformity of the flow distribution deteriorate. The velocity and pressure profiles for $D_{\mathrm{rods}} = 30\,\mathrm{mm}$ are visualized in **Fig. 4.9**.

Tab. 4.4: Simulated resonance frequencies of CFF blades with reinforcing circularly arranged rods.

d_{rod} / D_{rods} (mm)/(mm)	Material (−)	$\omega_{\mathrm{bend,sim}}$ (rpm)	$\omega_{\mathrm{bend,meas}}$ (rpm)
−	aluminum	7360	5800
5 / 20	stainless steel	7260	−
5 / 30	stainless steel	7530	−

The simulated bending resonance frequencies are listed in **Tab. 4.4**. The increase in mechanical stiffness and hence the shift to higher bending resonance frequency is below 3 %. Therefore, no prototypes have been commissioned.

In summary, neither the reinforcing central shafts nor the circularly arranged rods lead to an increase in CFF performance.
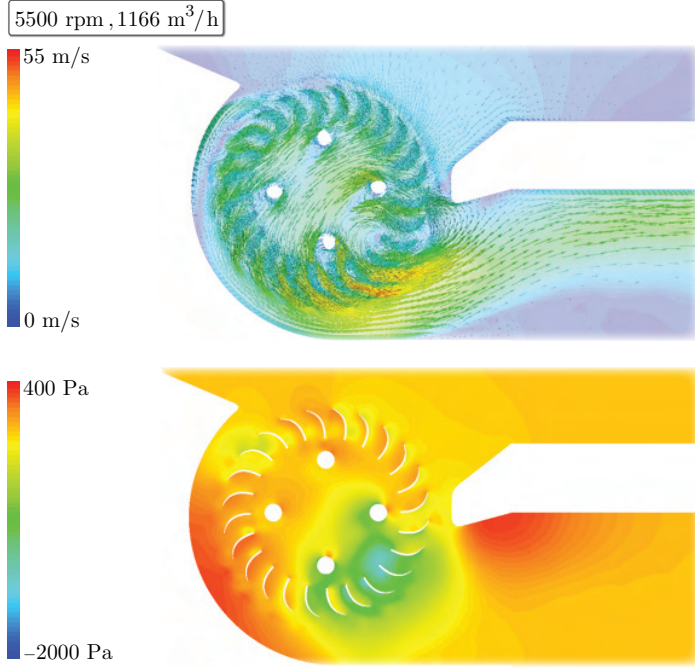
Fig. 4.9: CFD-simulated velocity (top) and pressure (bottom) profiles for the modified CFF rotor with circularly arranged rods (d_{rod} = 5 mm and D_{rods} = 30 mm) for a stable, high-flow operating point at 5500 rpm.

4.3.2 Static Casing Walls Modifications

For the CFD analysis of modifications to the static casing walls, the primary focus lies on the vortex wall, as CFFs are particularly prone to creating recirculation zones in this area. The CFD simulations are conducted for minor geometry changes allowing to track the specific effects of each modification, providing a clear understanding of their impact on the overall performance. It has to be ensured that any changes are comprehensible and can be implemented and validated through physical testing. Furthermore, the distance between the fan blades and the vortex wall, defined as ϵ_1 in **Fig. 4.3 (c)**, is kept constant to maintain the necessary safety distance required due to the use of magnetic bearings.

The following modifications include an increased inlet angle, a downward shift of the rear wall and adaptations of the vortex wall inlet and outlet side.

73

Increased Inlet Angle ϕ_i

To analyze the influence of paddle region B on fan performance, the inlet angle ϕ_i of the initial design is significantly increased from 40° to 65°.

The dimensionless pressure–flow curves resulting from the CFD analysis in the high-flow region are shown in **Fig. 4.10**. Comparing the initial design to the modified, it is observed that the dimensionless flow $\Delta\varphi_{CFF,max}$ remains almost unaffected by this change. This indicates that the inlet modification of ϕ_i has negligible impact on performance.

Comparing the velocity and pressure profiles from the initial design shown in **Fig. 4.4** to those of the design with changed inlet angle in **Fig. 4.11**, reveals that the size of paddle region B is reduced while work region A remains largely unchanged. This suggests that the impact of the rear wall inlet side modification on fan performance is negligible.
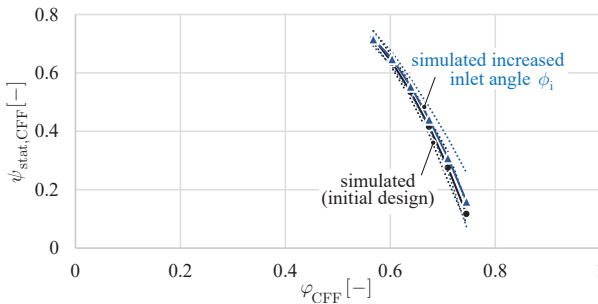

Fig. 4.10: Simulated dimensionless pressure–flow curve for the CFF with static casing wall with increased inlet angle ϕ_i from 40° to 65°. Compared to the initial design, the dimensionless flow $\Delta\varphi_{CFF,max}$ remains almost unaffected by this change, indicating that ϕ_i has minimal influence on performance.
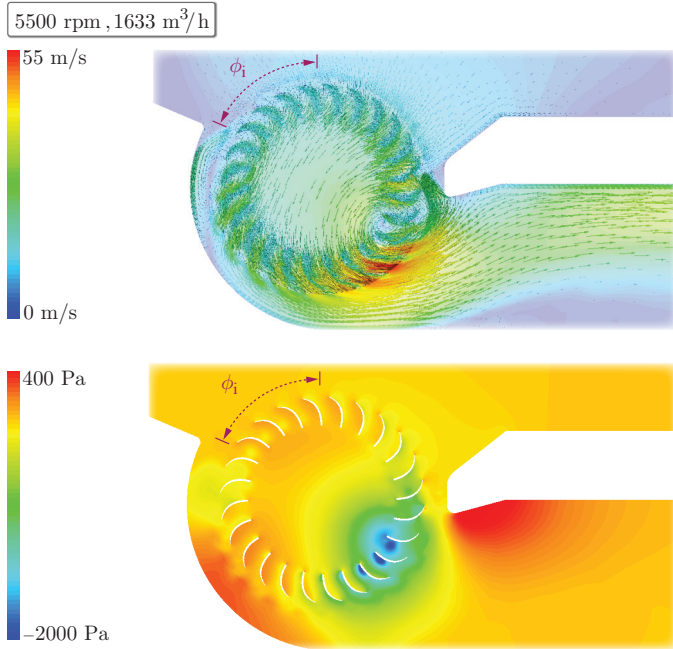
Fig. 4.11: CFD-simulated velocity (top) and pressure (bottom) profiles for the CFF with increased inlet angle ϕ_i, for a stable, high-flow operating point at 5500 rpm. This modification reduces the size of paddle region B, while work region A remains largely unaffected, hence there is minimal impact on fan performance.

Rear Wall Shift

This modification involves a downward shift of the rear wall. The adjustment changes the outlet parameters h and h_2 as well as the inlet distance from the rotor to the rear wall ϵ_2, as defined in **Fig. 4.3 (c)**, while the geometry of the vortex wall remains unchanged.

The CFD results of the dimensionless pressure-flow curves are shown in **Fig. 4.12**, indicating a 10 % increase in the maximum dimensionless flow $\Delta\varphi_{\text{CFF,max}}$. Comparing the pressure profiles between the resulting design shown in **Fig. 4.13** and the original configuration depicted in **Fig. 4.4**, a reduction in the high-pressure zone at the outlet side of work region A is achieved, leading to less pressure losses.
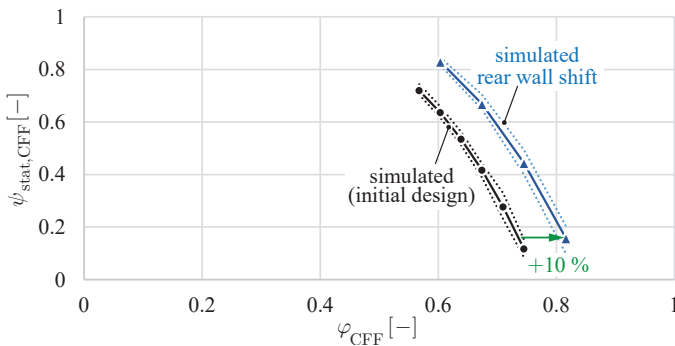

Fig. 4.12: Simulated dimensionless pressure–flow curve for the CFF with static casing wall modifications, featuring a 5 mm downward shift of the rear wall. Compared to the initial design, the maximum dimensionless flow $\Delta\varphi_{\text{CFF,max}}$ increases by 10 %.
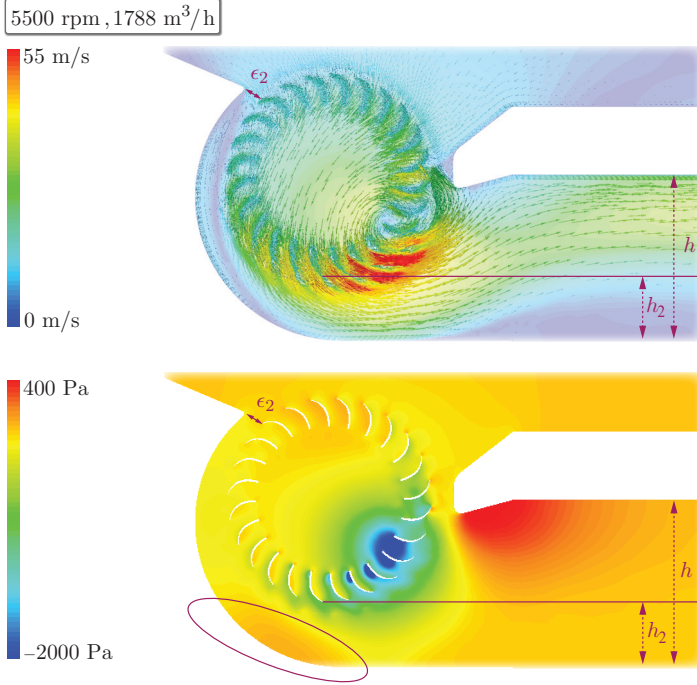
Fig. 4.13: CFD-simulated velocity (top) and pressure (bottom) profiles for the CFF with the rear wall shifted downward by 5 mm for a stable, high-flow operating point at 5500 rpm. The changes in outlet parameters h, h_2 and the inlet distance from the rotor to the rear wall ϵ_2, as defined in **Fig. 4.4**, are marked, while the geometry of the vortex wall remains unchanged. Compared to the initial design in **Fig. 4.4**, the high-pressure zone at the outlet side of work region A is reduced, leading to less pressure losses.

Rear and Vortex Wall Shift

In addition to the downward shift of the rear wall, the vortex wall is also shifted downward, altering the vortex wall inlet and outlet angles α and β, respectively. The new design is simulated for several high-flow operating points and the resulting dimensionless pressure-flow curve is shown in **Fig. 4.14**. Compared to the initial design, this modification enhances the dimensionless flow $\Delta\varphi_{\text{CFF,max}}$ by 15 %.

This casing wall modification has been commissioned and tested on the test bench and the resulting dimensionless curve is plotted in **Fig. 4.14**. The
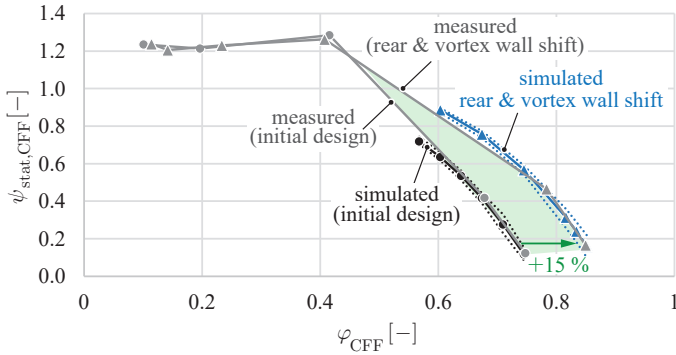
Fig. 4.14: Dimensionless pressure–flow curve for the CFF with static casing wall modifications, featuring a 5 mm downward shift of the rear and vortex walls. The curves are simulated in the high-flow region and measured on the test bench. Compared to the initial design, the maximum dimensionless flow $\Delta\varphi_{CFF,max}$ increases by 15 %. The green area highlights the newly measured performance gains.

casing wall adaptation validates the CFD simulation results very well in the high-flow region. Additionally it can be seen from the measurements (gray), that these changes did not effect the pressure $\psi_{stat,CFF}$ in the low-flow region.

The simulated velocity and pressure profiles for a stable, high-flow operating point at 5500 rpm are illustrated in **Fig. 4.15**. The downward shift of the vortex wall decreases its inlet angle α and increases its outlet angle β. When comparing the resulting pressure profile to the initial design shown in **Fig. 4.4**, a lower eccentric vortex pressure is evident (indicated by dark blue scaling). This reduction in eccentric vortex pressure indicates that the airflow through the fan is more streamlined and encounters less resistance, resulting in improved performance in the high-flow region.
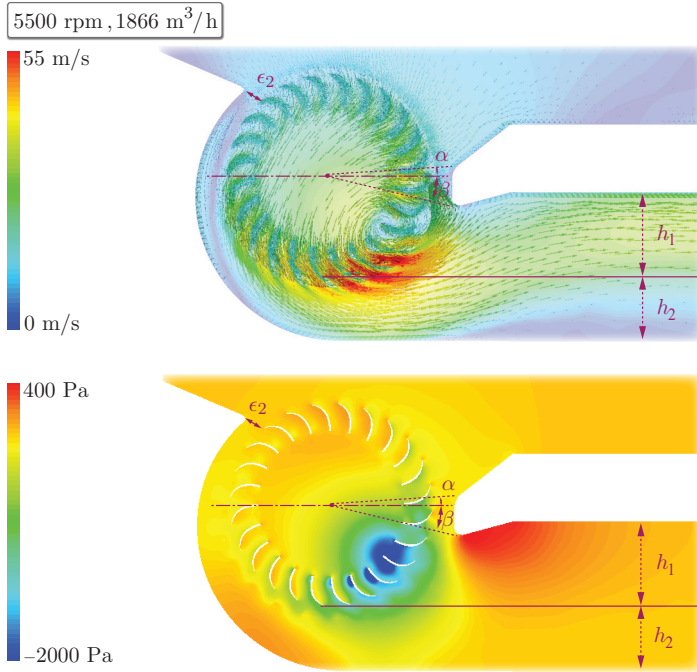
Fig. 4.15: CFD-simulated velocity (top) and pressure (bottom) profiles for the CFF with the rear and vortex wall shifted downward by 5 mm for a stable, high-flow operating point at 5500 rpm. The changes in outlet parameters h_1, h_2 and the vortex wall angles α and β are marked. Compared to the initial design shown in **Fig. 4.4**, the pressure profile reveals a lower eccentric vortex pressure (dark blue scaling). This indicates a more streamlined airflow with reduced resistance through the fan, enhancing the fan performance in the high-flow region.

Adaptations of Outlet Side

Furthermore, the vortex wall outlet side is modified by adjusting the outlet height h_1 and vortex wall outlet angle β. Four parameter sets are simulated at $\varphi_{\mathrm{CFF}} = 0.85$ (high-flow), and the resulting dimensionless pressure $\psi_{\mathrm{stat,CFF}}$ is evaluated, as shown in **Fig. 4.16 (a)**. The most optimal configuration is identified with $h_1 = 29\,\mathrm{mm}$ and $\beta = 11.8°$. Several additional points are simulated, as depicted in **Fig. 4.16 (b)**. Testing the new positioning of the vortex wall outlet on the test bench results in an increase of $\Delta\varphi_{\mathrm{CFF,max}}$ by 22 %.

The simulated velocity and pressure profiles are shown in **Fig. 4.17**. It
can be concluded, that varying h_1 and β results in a trade-off between outlet
resistance and recirculation. Increasing h_1 results in a larger outlet, hence
reduces the resistance encountered by the air as it leaves the CFF impeller
blades (outlet side of work region A). However, this modification decreases β,
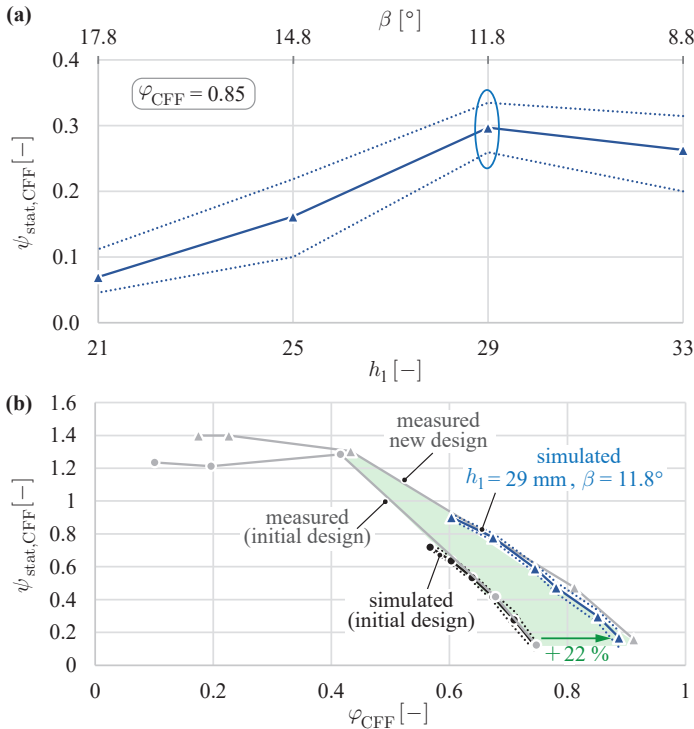allowing more recirculation in the eccentric vortex region C.

Fig. 4.16: (a) Simulated dimensionless pressure $\psi_{\text{stat,CFF}}$ for a high-flow operating
point with $\phi_{\text{CFF}} = 0.85$ is analyzed for different vortex wall outlet geometries, includ-
ing variations in the vortex wall outlet height h_1 and vortex wall outlet angle β. The
configuration with $h_1 = 29$ mm and $\beta = 11.8°$ is identified as optimal. **(b)** Dimension-
less pressure–flow curve for the CFF with $h_1 = 29$ mm and $\beta = 11.8°$. The curves are
simulated in the high-flow region and measured on the test bench. Compared to the
initial design, the maximum dimensionless flow $\Delta\varphi_{\text{CFF,max}}$ increases by 22 %. The
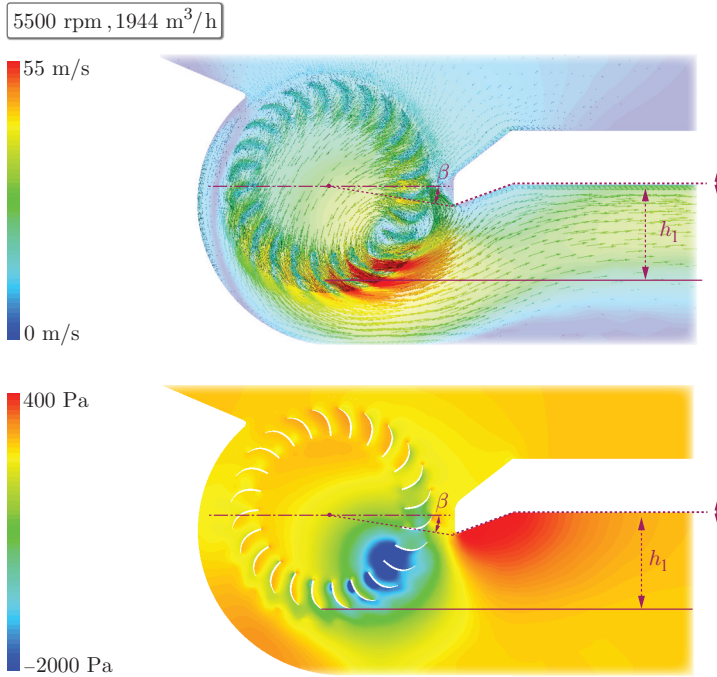green area highlights the newly measured performance gains.

Fig. 4.17: CFD-simulated velocity (left) and pressure (right) profiles for the CFF with $h_1 = 29$ mm and $\beta = 11.8°$ for a stable, high-flow operating point at 5500 rpm. Compared to the initial design shown in **Fig. 4.4**, an optimum is found between outlet resistance and recirculation.

In summary, the static casing wall modifications are shown to enhance the CFF's performance, achieving a maximum flow increase up to 22 %.

4.4 Summary

This chapter conducts a CFD-based optimization of measures to enhance the performance of bearingless CFFs, which is particularly important for certain industrial applications in the semiconductor industry. Modifications of the CFF rotor and static casing walls are investigated. Various prototypes are derived from the simulation results, then commissioned and tested.

It is concluded that to enhance CFF performance, the work region A must remain unobstructed for fluid flow, the eccentric vortex region C must be

81

stabilized through careful design of the vortex wall, while the paddle region B is largely irrelevant for CFF performance.

Regarding the rotor modifications, introducing different dimensions of central shafts and circularly arranged rods within the CFF impeller impacts both the rotor dynamic and fluid dynamic performance. Specifically, a stainless steel shaft with a diameter of 20 mm shifts the critical bending resonance frequency of the CFF blades 42 % higher. However, CFD simulations and experimental measurements showed that the flow drops by 61 %, hence the loss in fluid dynamic performance outweighs the gain in rotational speed for all tested reinforced CFF rotors. The CFD investigation of circularly arranged rods additionally revealed that the rods induce significant, undesired pressure pulsations within the eccentric vortex. These pulsations lead to unstable flow patterns, which are not desired for the application in gas circulation systems of excimer lasers.

Regarding the casing wall modifications, the CFF performance is highly sensitive to changes in geometric parameters, particularly the vortex wall, as the casing walls directly influence the airflow path through the fan. A successful simulated and measured performance increase of up to 22 % is achieved.

In summary, the chapter's results demonstrate that the performance of the bearingless CFF can be enhanced by modifying the geometry of the casing walls, without altering the rotor or the bearingless motor.

5

Conclusion and Outlook

THIS dissertation addressed the limitations of state-of-the-art magnetically levitated cross-flow fans, which are constrained by issues of compactness, complex hermetic encapsulation and magnetic air gap geometry, and performance due to one-sided drive torque generation. For cutting-edge applications such as gas circulation systems in DUV excimer lasers, these challenges aggravate adherence to safety standards, complicate costly maintenance work and installations, and reduce the lifespan of the fan system. The novel bearingless CFF is proposed and investigated to address these issues, and to overcome numerous challenges imposed by the stringent constraints and requirements of the target application on the drive system and CFF rotor.

5.1   Results of this Thesis

The content of this thesis is briefly summarized in the following, highlighting the most significant results.

▶ The operating principle of the bearingless CFF was discussed in **Chapter 2**, explaining the bearing force and drive torque generation. A control structure of the levitation and rotation of a CFF rotor via two bearingless motors was presented, where bearing forces are independently created and controlled, while the torque is generated by both motors through the passing of a reference drive current from the primary to the secondary motor. Thus, each motor contributes half of the required drive torque, ensuring an even load distribution.

Furthermore, two CFF rotor prototypes were designed, commissioned and compared with respect to rotor dynamics, fluid dynamics, and man-

ufacturability. Their impact on the magnetic bearing and operational limits were evaluated.

The theoretical analysis comprised an analytical description of key rotor dynamic effects and a Finite-Element Method (FEM) modal analysis of the expected resonance modes and frequencies for the two prototypes, excited by an unbalance force. This analysis revealed that rigid body, torsional and bending vibrations can be excited within the targeted speed range.

For the fluid dynamics assessment of the prototypes, a two-dimensional Computational Fluid Dynamics (CFD) model was developed. A thorough mesh and time step analysis was conducted, resulting in a robust simulation model, offering a good compromise between computational time and resolution. It served as a design tool for evaluating various CFF geometries at different speeds and operating points, as well as for visualizing flow profiles.

To conduct the experimental CFF analysis, a test bench was designed and commissioned. It allowed to validate the FEM simulations, to safely perform the rotor dynamic experiments and to determine the pressure–flow characteristics for different prototypes under various operating conditions.

The results of the experimental analysis revealed that the rigid body modes and torsional modes were not excited by the rotor unbalance. However, the bending resonance was excited, limiting the rotational speed for both CFF rotor prototypes. The two bearingless CFF prototypes were operated at speeds up to 12 000 rpm and 5500 rpm, respectively. The CFF operating at 12 000 rpm generated a maximum flow rate of 1450 m^3/h or a maximum pressure increase of 580 Pa, depending on the operating point. In contrast, the CFF operating at a maximum speed of 5500 rpm achieved a maximum fluid flow of 1600 m^3/h or pressure increase of 220 Pa. The comparison of the two designs showed that a robust design, while allowing for high rotational speeds, caused a reduction in fluid performance. This reduction was due to the thicker blades, which were designed to increase mechanical stiffness, and the straight blade profile, which was chosen to simplify manufacturability.

▶ A novel bearingless CFF rotor design was presented in **Chapter 3**. This design introduced additional mechanical elements with low bending stiffness between the CFF blades and rotor magnets. The vibration behavior was influenced such that an additional resonance frequency

occurred, however, the detrimental resonance for the CFF blades was shifted to higher frequencies. Since the unbalance forces primarily deformed the soft decoupling elements at the additional resonance, it could be successfully passed, enabling the CFF rotor to self-center without blade damage. It was demonstrated how stable operation at supercritical speed was achieved, thereby increasing the maximum achievable rotational speed and enhancing fluid dynamic performance.

A mass-spring-damper (*mkd-*)model was developed to theoretically investigate how the presence of decoupling elements affects the resonance modes and frequencies of the overall CFF rotor. It allowed to model several mass, stiffness and damping characteristics of the magnetic bearing, the decoupling elements and the CFF rotor, to then evaluate the unbalance responses in terms of resonance frequency and mode shape.

An experimental investigation was conducted to validate the *mkd-*model and evaluate the influence of various decoupling elements on the magnetic bearing. To prevent a possible collision between the CFF blades and the static casing walls when passing the resonance frequencies, auxiliary touch-down bearings were installed in the casing wall on each side of the rotor. Furthermore, laser distance sensor measurements and analyses of the bearing currents confirmed the expected mode shapes. An optimal stiffness ratio between the stiffness of the decoupling elements and the CFF blades of 0.47 was obtained, resulting in the highest achievable rotational speed among the seven prototypes tested. This ratio offered the best trade-off between a "soft" enough decoupling, to be able to penetrate the supercritical region and a "stiff" enough decoupling element, to shift the speed-limiting resonance to higher frequencies.

Finally, for the fluid dynamic assessment of the novel prototype's pressure–flow characteristics, stable operation was achieved up to 7000 rpm. This represented a 40 % increase in rotational speed, leading to a 28 % higher fluid flow and a 100 % increase in static pressure compared to the CFF rotor without decoupling elements. The fluid flow did not scale linearly with the increase in rotational speed due to the reduction in the active CFF fluid inlet length caused by the touch-down bearings. However, the theoretically expected quadratic increase in pressure was observed to align well with the experimental results.

▶ **Chapter 4** presented a CFD-based optimization of bearingless CFF designs to enhance performance. This chapter investigated modifications of the CFF rotor and static casing walls, resulting in the development of various prototypes derived from the CFD results.

Key findings regarding the fundamental CFF aerodynamics were that for optimal CFF performance, the work region inside the CFF rotor must remain unobstructed for fluid flow, the eccentric vortex region should be stabilized through careful design, and the paddle region is largely irrelevant.

Rotor modifications, such as varying the central shaft dimensions and incorporating circularly arranged rods, significantly impacted both rotor dynamics and fluid dynamics. A 20 mm stainless steel shaft increased the critical bending resonance frequency by 42 %, but resulted in a 61 % loss in maximum fluid flow, due to crucial flow obstructions within the work region. For all tested prototypes, the loss in fluid flow outweighed the gain in rotational speed. Additionally, circularly arranged rods caused undesirable pressure pulsations and unstable flow patterns.

Modifications to the casing walls significantly affected CFF performance, with the vortex wall being particularly crucial. The optimization of the rear wall position resulted in a measured 10 % increase in maximum fluid flow. Additionally, optimizations of the vortex wall position as well as its inlet and outlet angles aimed at reducing recirculation losses, led to a measured performance increase of up to 22 %, achieving a flow rate of 1800 m^3/h at 5000 rpm.

5.2   Outlook and Future Research

The obtained results highlight the potential of bearingless cross-flow fans for demanding industrial applications. The presented concept has the potential to serve as a foundation for future gas circulation systems in pulsed DUV excimer lasers. For future research and development, the following aspects could be considered:

▶ *Rotor up-scaling:* scaling up the lab-sized CFF to match the dimensions required for excimer lasers could further advance the adaptation of bearingless CFF technology to its target application. It could simplify the implementation of stiffness increasing measures.

▶ *Rotors with decoupling elements*: the findings from the study on decoupling elements between the rotor magnets and the CFF blades, could be extended to other potential applications where increasing rotational speed is beneficial.

▶ *Excimer laser operating conditions*: operating conditions within DUV excimer laser tubes are challenging due to the presence of corrosive and toxic gases in the pressurized laser chamber. Nevertheless, designing such a high-pressure chamber and conducting performance measurements could lead to advancements in material selection, performance optimization for high-pressure environments, and operational reliability.

▶ *Further applications*: exploring potential applications beyond DUV excimer lasers where bearingless CFFs could provide benefits, such as in other precision optical systems, clean room environments, or medical equipment.

Appendices

A

Design and Characterization of a Bearingless Cross-Flow Fan

This chapter summarizes the most relevant findings from the preliminary study on the design and characterization of the first bearingless cross-flow fan, as also published in:

▶ I. Bagaric, D. Steinert, F. Wassmer, T. Holenstein, T. Nussbaumer and J. W. Kolar, "Design and Characterization of a Bearingless Cross-Flow Fan," in *Proc. of the IEEE/ASME International Conference on Advanced Intelligent Mechatronics (AIM)*, Delft (virtual), Netherlands, July 2021. DOI: 10.1109/AIM46487.2021.9517520.

─── **Chapter Abstract** ───

This chapter presents a first prototype of the bearingless cross-flow fan particularly suited for applications in chemically demanding environments. In general, bearingless motors convince with a friction- and wear-free operation, nearly unlimited lifetime and a hermetically-sealed encapsulation of the rotor. For the proposed cross-flow fan, a double-sided use of such motors additionally leads to twice the available torque for the blade rotation as well as a highly compact and safe system design. In sophisticated applications (e.g., gas-circulation systems of excimer laser) those arguments are crucial. After a description of the motor topology, the novel bearingless cross-flow fan prototype is introduced and its performance characterized, by means of experimental measurements. It is operated up to 3500 rpm with bearingless motors with outer diameter of 75 mm and height of 70 mm, while the CFF blades feature a length of 420 mm and diameter of 61 mm.
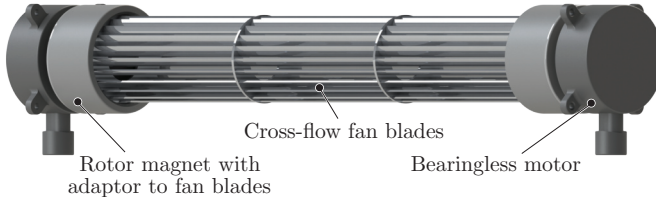
Rotor magnet with
adaptor to fan blades

Cross-flow fan blades

Bearingless motor

Fig. A.1: Introduced cross-flow fan composed of two bearingless motors, two magnets and cross-flow fan blades.

A.1 Introduction

Bearingless motors enable a fully contactless magnetic levitation of rotors because of their integrated bearing and drive functionality [30]. The various types of bearingless motors share the same convincing advantages of long lifetime and low maintenance costs, since they allow friction- and wear-free operation [88]. Moreover, a large air gap design between stator and rotor makes a hermetically-sealed encapsulation of the rotor possible. The stator can then operate the completely separated and isolated rotor in chemically demanding, high-purity or extreme temperature environments [89]. Those advantages of bearingless motors improve many demanding systems for example in the semiconductor, pharmaceutical or biomedical industry such as pumps [90], mixers [31] or fans [33].

Cross-flow fans are known for their large length-to-diameter ratios. Due to their rectangular inlet and outlet cross-sections, a uniformly distributed inflow and outflow is produced [42]. Together with a suitable fan housing design, cross-flow fans are implemented in numerous applications ranging from air conditioning devices [41] to sophisticated gas-circulation systems in excimer laser [12].

So far, magnetically levitated axial fans have been proposed by several authors. In [91], an axial fan is presented where two passive magnetic bearings stabilize four degrees of freedom (DOFs), radial and tilt directions. The control of the axial direction (5th DOF) is solved using an active magnetic bearing, while the rotational degree of freedom is actuated separately by a permanent magnet synchronous motor. A one-axis (z-direction) actively and four-axes passively positioned axial fan is realized by [92] and [93] as well. However, the axial force and the torque are independently regulated by the q- and d- currents of the single-drive bearingless motor with laminated stator cores. In [33], an axial fan application is suggested using a bearingless

axial-force/torque motor. Two radial permanent magnetic ring bearings stabilize radial and tilt deflections of the rotor passively, whereas axial force and drive torque are controlled actively. The proposed motor topology features a bell-shaped exterior rotor with an inner shaft.

The goal of this chapter is to introduce the novel bearingless cross-flow fan by means of a prototype. The focus lies on a compact motor that maintains chemical resistance and high purity standards as is desired in gas-circulation systems of excimer laser. **Sec. A.2** shows the conceptual design of the used motor topology and briefly explains its working principle. Based on two bearingless motors, the cross-flow fan prototype will then be described in **Sec. A.3**. The system is characterized with pressure-flow curves on an ISO 5801 based test rig in **Sec. A.4**.

A.2 Motor Topology

The focus of this chapter lies on a particularly compact and easily maintainable motor design for the demonstration of the bearingless cross-flow fan for industrial applications. To achieve such a system, a reasonable decision between an exterior or interior type of motor is necessary as a first step. **Fig. A.2** illustrates two possible concepts, where the left design shows an interior-rotor type (stator surrounding rotor) and the right design, an exterior-rotor type (rotor surrounding stator). As visualized, for an exterior-rotor type the stator together with all the sensors, control and power electronics barely exceeds the diameter of the fan blades, whereas the interior version has much larger dimensions. Therefore, the decision has been made in favor of the highly compact exterior-rotor type design.

In a second step, the number of stator teeth and the pole pair number has to be selected satisfying the compactness criteria as well. To get a functional bearingless motor a minimal stator slot number of four is necessary [94]. However, this topology shows disadvantageous single-phase behavior with large cogging torque [95]. The uneven stator teeth number of five has the drawback of permanently requiring high bearing currents to levitate the rotor [95]. Therefore, a slot number of six offers a promising trade-off between a compact design and a well functioning motor and was chosen for this study [95]. When selecting the rotor pole pair number p for the six-slot design, the condition has to be fulfilled

$$p = 2 + (n \cdot 6), \qquad n = 0, 1, 2, \ldots \qquad \text{(A.1)}$$
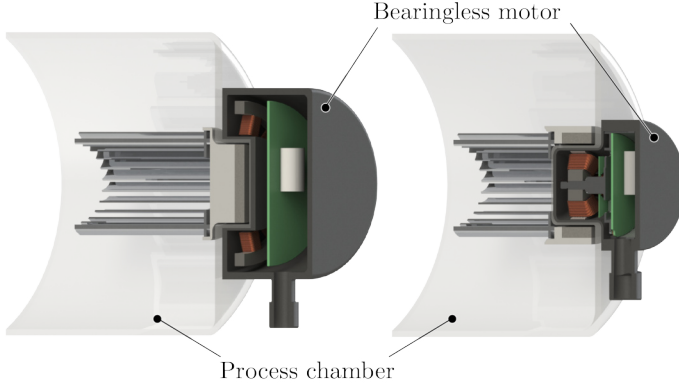
Fig. A.2: Conceptual design of a cross-flow fan in a process environment which is driven by bearingless motors. The interior-rotor type (left) requires much larger motor dimensions for all its components than the exterior-rotor design (right). Therefore, the latter is chosen for the first demonstration of the bearingless cross-flow fan.

as described in [95]. The presented rotor satisfies this condition by having four permanent magnets ($p = 2$) that are magnetized in alternating order in radial direction. Finally, **Fig. A.3** illustrates the selected motor topology. The stator includes six teeth made of laminated iron with six corresponding copper coils, while the rotor consists of a back iron ring and four permanent magnets. This motor setup can now generate both bearing forces and drive torque, thus stabilize the systems 6 DOFs.

A.2.1 Passive Bearing

The term *passive* implies that the generated bearing forces originate solely from the permanent magnets. For the presented topology, the attracting reluctance forces between the stator iron and the rotor magnets act in favor of axial (1 DOF) and tilting (2 DOFs) stability. This means that a distortion from the rotor's center position in axial or tilting direction is counteracted by restoring forces. The extent to which those forces react is defined by the axial force displacement factor

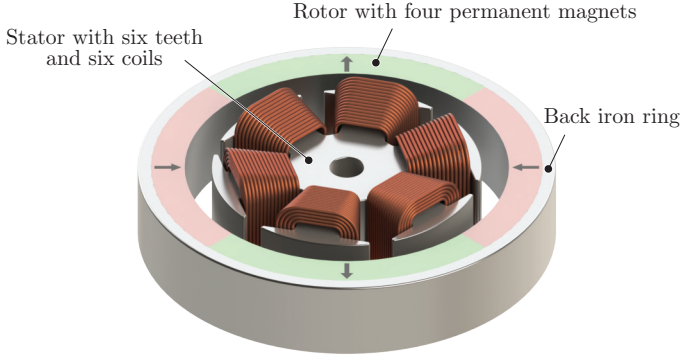$$k_z = \frac{\Delta F_z}{\Delta e_z} \tag{A.2}$$

Fig. A.3: Conceptual drawing of a bearingless motor with six stator teeth and six corresponding coils. The rotor consists of a back iron ring and four permanent magnets that are magnetized in alternating order.

and the torque factor

$$k_\varphi = \frac{\Delta M_\varphi}{\Delta \varphi}. \tag{A.3}$$

If those factors are sufficiently large, which is the case for this setup, the axial and tilting directions are fully stabilized by passive bearings. Using passive stabilization contributes to achieving a highly compact system as well. However, it is physically impossible to stabilize all DOFs purely passively (Earnshaw's theorem [96]).

A.2.2 Active Bearing

When dislocating the rotor from its center position in radial direction, the resulting reluctance force will support that movement until stator and rotor mechanically collide. This destabilizing force can be described by a radial force displacement factor

$$k_{x,y} = \frac{\Delta F_{x,y}}{\Delta e_{x,y}}. \tag{A.4}$$

Since no stable radial rotor position is possible, an active magnetic bearing has to counteract this destabilizing force in the two DOFs. Such a resulting suspension force can be generated by an air-gap flux-density distribution, having a frequency component of

$$f_{bng} = f_{mech} \cdot (p \pm 1), \tag{A.5}$$
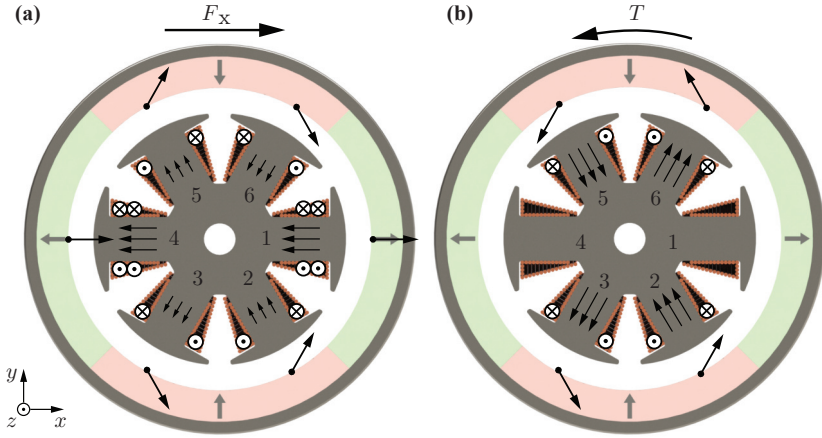
95

Fig. A.4: (a) Radial force generation in x-direction: two opposite coils have currents of same magnitude but opposite direction. Forces in y- direction cancel each other out, so a force F_x results. **(b)** Torque generation: two opposite coils have currents of same magnitude and same direction. Radial forces cancel each other out while tangential forces create a torque T.

as described in [97]. Combining a suitable harmonic wave coming from the winding scheme with the harmonics from the stator teeth, these flux-density components can be generated [97]. The resulting suspension forces include radial as well as tangential forces. As shown in **Fig. A.4 (a)**, a radial force F_x is created when two opposite stator teeth (e.g. coils 1 and 4) have currents of same magnitude but opposite direction. Following this principle, the rotor can be completely stabilized in the two radial DOFs.

A.2.3   Torque Generation

The last DOF is the motor torque, which can be created by an air-gap flux-density distribution of

$$f_{\text{drv}} = f_{\text{mech}} \cdot p, \tag{A.6}$$

as described in [97]. The resulting torque stems from tangential forces while the radial forces cancel each other out. **Fig. A.4 (b)** illustrates how a torque is created for the proposed system when two opposite stator teeth have currents of same magnitude and same direction.

A.2.4 Rotor Control

So far, the active bearing and drive torque have been described as separate entities. However, for combined windings (bearing and drive currents in one coil), these components need to be correctly taken into account within the control system. As can be seen in **Fig. A.4 (a)** and **Fig. A.4 (b)**, desired forces can be achieved by a corresponding summation or subtraction. When the sum of drive and bearing currents of the six coils is taken, it results in currents in three non-adjacent coils, whereas subtracting them leads to currents in the remaining three coils [95]. These mathematical operations allow to control bearing forces and drive torque within combined coils by superimposing bearing and drive currents.

A.2.5 Combining Two Bearingless Motors

For the proposed bearingless cross-flow fan, two such motors are responsible for the active bearing and torque generation of the long-shafted rotor blades. Theoretically, having a double-sided implementation offers twice the available torque for the blade rotation. As explained before, for a bearingless motor with combined windings the drive and bearing functions are handled separately then superimposed. When combining two such motors with a shared rotor, the control scheme has to be adapted. The introduced prototype features a control structure implemented for each motor independently.

A.3 Prototype

Fig. A.5(a) shows the final cross-flow fan prototype with its dimensions. For the two motors, each stator is cast into a 3D printed housing with a diameter of $d_M = 75$ mm. Additionally, a 3D printed adapter is mounted onto each magnet allowing to mechanically connect the fan blades and creating a common rotor. The fan blades have a length of $L = 420$ mm and a diameter of $d_B = 61$ mm. The CAD rendering in **Fig. A.5(b)** visualizes the internal components of the prototype including the stator iron, copper coils and the integrated power electronics while **Fig. A.5(c)** summarizes the technical data of a single motor prototype.
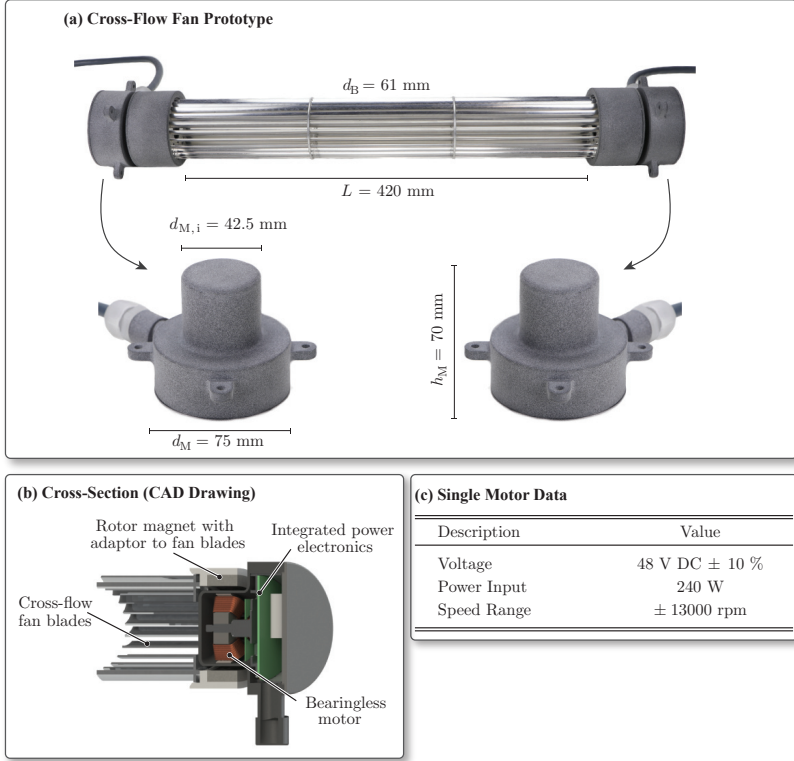
Fig. A.5: The bearingless cross-flow fan prototype where **(a)** specifies the dimensions, **(b)** illustrates the internal components with a CAD drawing of the cross section and **(c)** tabulates the technical data of a single motor prototype.

A.4   Measurements

A.4.1   Test Rig

The test rig is based on the ISO 5801 norm, which describes how performance measurements of industrial fans can be performed using standardized airways. As illustrated in **Fig. A.6(a)**, it consists of a ducted inlet and ducted outlet ($d_{\text{duct}} = 200$ mm) and incorporates different components. A *flow control valve* at the inlet side allows to regulate the flow of the incoming air stream. For

the fan characterization, the difference of the total pressures

$$\Delta p_{\text{tot}} = p_{\text{tot, out}} - p_{\text{tot, in}} \qquad (A.7)$$

has to be detected, where the total pressure is equal to the sum of static and dynamic pressure

$$p_{\text{tot}} = p_{\text{stat}} + p_{\text{dyn}}. \qquad (A.8)$$

Since the cross sections of the inlet and outlet duct are equal, the dynamic pressure does not change over the fan ($p_{\text{dyn, in}} = p_{\text{dyn, out}}$) and the total pressure difference becomes

$$\Delta p_{\text{tot}} = p_{\text{stat, out}} - p_{\text{stat, in}}. \qquad (A.9)$$

Therefore, it is possible to measure the static pressure before and after the fan with two *pressure sensors* to get the total pressure difference. The outgoing air stream is detected with a *flow sensor*, where a honeycomb *flow straightener* is required on the inlet side to straighten the air flow. The cross-section of the CFF blades and surrounding casing walls is shown in **Fig. A.6 (b)**, whereas the test rig's dimensions are summarized in **Fig. A.6 (c)** and the pressure and flow sensor data in **Fig. A.6 (d)**.

A.4.2 Fan Characterization

The pressure-flow curves of the presented cross-flow fan are shown in **Fig. A.7** and **Fig. A.8**, where the former illustrates the physical values (p and Q) and the latter the dimensionless parameters (φ and Ψ). The dimensionless flow number φ is defined as

$$\varphi = \frac{Q}{u \cdot d_B \cdot L}, \qquad (A.10)$$

where d_B and L are the blades' diameter and length and u is the velocity of circulation

$$u = \pi \cdot d_B \cdot n, \qquad (A.11)$$

with n being the rotor speed. The dimensionless pressure number Ψ is defined as

$$\Psi = \frac{\Delta p_{\text{tot}}}{\rho_{\text{air}}/2 \cdot u^2}, \qquad (A.12)$$

with a density of air being $\rho_{\text{air}} = 1.2041 \, \text{kg/m}^3$. The measurements have been conducted with rotor speeds of 2000 rpm, 2500 rpm, 3000 rpm and 3500 rpm. As expected, the pressure difference over the fan Δp_{tot} decreases with increasing flow rate Q (cf. **Fig. A.7**).

(a) Test Rig Components

(b) CFF Blades and Casing walls

Cross-flow fan blades

Casing walls

(c) Dimensions

$w_{\text{CFF, inlet}} = 0.42\text{m}$
$h_{\text{CFF, inlet}} = 0.08\text{m}$

1m   1m   1m   0.5m   1m   1m

$d_{\text{duct}} = 0.2\text{m}$

$w_{\text{CFF, outlet}} = 0.42\text{m}$
$h_{\text{CFF, outlet}} = 0.04\text{m}$

(d) Sensor Data

Description	Range	Accuracy
Differential pressure sensor	± 4000 Pa	$\pm 1\% + 1$ Pa
Thermal flow sensor	$0.2 \ldots 60$ m/s	$\pm 2\% + 0.02$ m/s
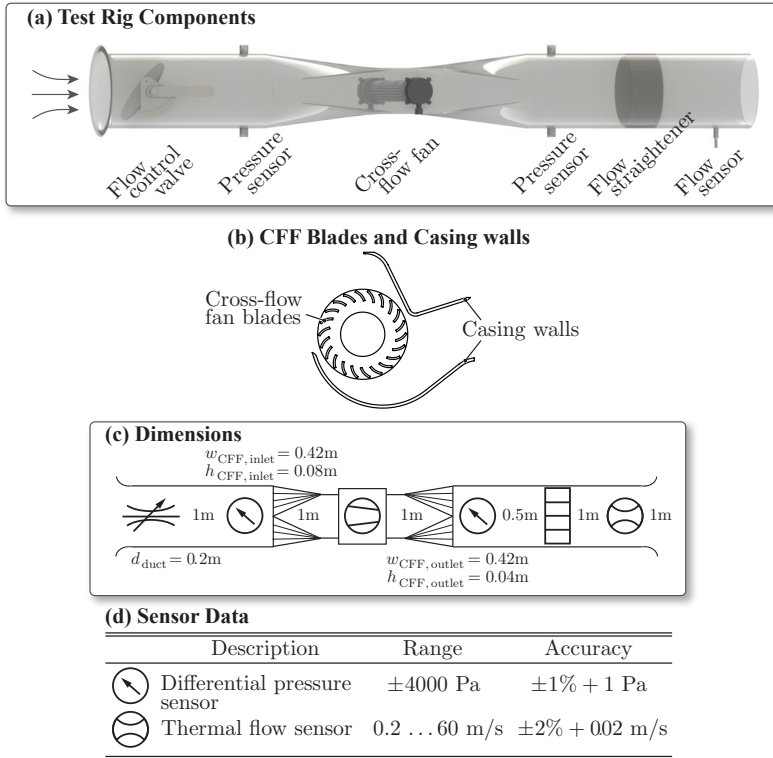
Fig. A.6: Conceptual drawing of the ISO 5801 based test rig where **(a)** visualizes its components including the cross-flow fan (CFF) prototype, a flow control valve, two pressure sensors, a flow straightener and a flow sensor, **(b)** shows a sketch of the CFF blades and casing walls, **(c)** the test rig's dimensions and **(d)** tabulates the technical data of the pressure and flow sensors.

The low pressure values are characteristic for cross-flow fans. Looking at the dimensionless parameters in **Fig. A.8**, an unexpected parallel shift between the different speeds is noticed. Although the curves should overlap in the dimensionless plot, the pressure and flow coefficients seem to decrease with increasing speeds. This might be explained by rotor dynamical effects that occur for long-shafted rotors. These vibrations start to aggravate the stabilization by means of magnetic bearings and lower the performance of
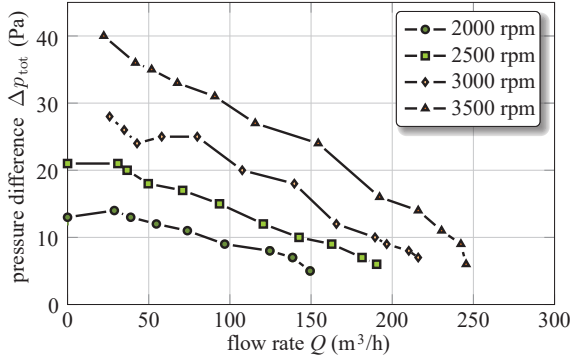
100

Fig. A.7: Pressure–flow characteristics of the proposed bearingless cross-flow fan prototype, where measurements are performed for different rotor speeds.
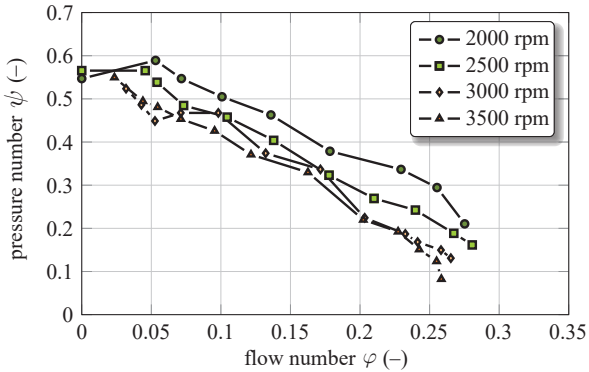

Fig. A.8: Dimensionless pressure-flow characteristics of the proposed bearingless cross-flow fan prototype, where the dimensionless parameters are calculated according to **Eqs. (A.10)** and **(A.12)**.

the fan in terms of pressure and flow. Appropriate measures will have to be studied in detail and correctly implemented.

A.5   Summary

The novel bearingless cross-flow fan has been introduced in this chapter. Based on two bearingless motors, its working principle has been described featuring unique performance in an ultra compact design. Rotor speeds of up to 3500 rpm have been reached and air flows up to ca. $250\,\mathrm{m^3/h}$ achieved.

B

Concept of a Novel Bearingless Three-Pole Motor for Two-Sided Driven Applications

This chapter summarizes the most relevant findings from the preliminary study on the concept of a novel bearingless three-pole motor topology for two sided-driven applications, as also published in:

▶ I. Bagaric, D. Steinert, T. Nussbaumer and J. W. Kolar, "Concept of a Novel Bearingless Three-Pole Motor for Two-Sided Driven Applications," in *Proc. of the 24th International Conference on Electrical Machines and Systems (ICEMS)*, Gyeongju (virtual), Korea, October 2021. DOI: 10.23919/ICEMS52562.2021.9634649.

Chapter Abstract

This chapter presents a novel bearingless three-pole motor for two-sided driven applications, i.e., two motors levitating and rotating a common rotor without any mechanical contact. When operating in chemically demanding environments its advantages are highly promising: the bearingless technology allows friction- and wear-free motion, unlimited lifetime and a hermetically sealed encapsulation of the rotor, while the novel motor convinces with its - in terms of hardware - minimalistic, compact and safe design. Using 3D FEM simulations, the new topology is evaluated focusing on maximal torque and sufficient bearing forces.

B.1   Introduction

By means of magnetic fields, bearingless motors levitate and spin rotors
without any mechanical contact while integrating the bearing and drive
functionality in one compact unit. This friction- and wear-free technology
enriches many demanding applications in the semiconductor, pharmaceutical
or biomedical industry such as pumps [98], mixers [94] or fans [93]. The
various bearingless systems convince with their long lifetime, low mainte-
nance costs and a hermetically sealed encapsulation of the rotor enabling
implementations in the harshest of environments. These so-called bearingless
slice motors are characterized by their much smaller stator and rotor lengths
compared to their rotor diameters ($L < d/2$). Attracting reluctance forces
between stator iron and rotor magnets act in favor of axial and tilting stability.
In order to control the remaining three degrees of freedom, the rotational
degree of freedom (DOF) and two radial DOFs have to be actively stabilized
by appropriate control currents. It holds that the force-current and torque-
current relations depend on the angular rotor position. To cover the whole
angular range and thereby enabling full motor performance, the selection of
stator teeth and rotor pole pair number is a crucial step.

The novel challenge tackled by this study is to achieve a stable levitation
and rotation of long shafts ($L_{shaft} >> d_{shaft}$) by bearingless motors. A possible
industry application could include a double-sided driven cross-flow fan for
gas circulation systems in excimer laser [12]. A previously introduced, fully
operational bearingless six-pole motor, i.e., the stator has six teeth and six
corresponding coils, is shown in **Fig. B.1 (a)** [35]. The commissioning of a
cross-flow fan has been successful and is described in [35] as well. It requires
two motors to levitate and rotate the common shaft.

The goal of this chapter is to introduce the novel three-pole motor topology
for two-sided driven applications (cf. **Fig. B.1 (b)**). Reducing the stator
topology from six to three teeth leads to an elegantly compact, simple design
featuring lower material and manufacturing costs as well as simplified power
electronics (from **Fig. B.1 (c)** to **Fig. B.1 (d)**). However, the three-pole motor
experiences single-phase drive characteristics, which has to be taken into
account carefully for double-sided driven applications. The focus of this study
lies on solving the single-phase drive deficit and designing an optimal motor
geometry such that maximal drive torque and sufficient bearing forces are
delivered from this highly compact entity. The drive torque behavior of a
single as well as coupled motor is analyses by means of 3D magnetostatic
simulations in **Sec. B.3**. Similarly, **Sec. B.4** evaluates its potential of generating
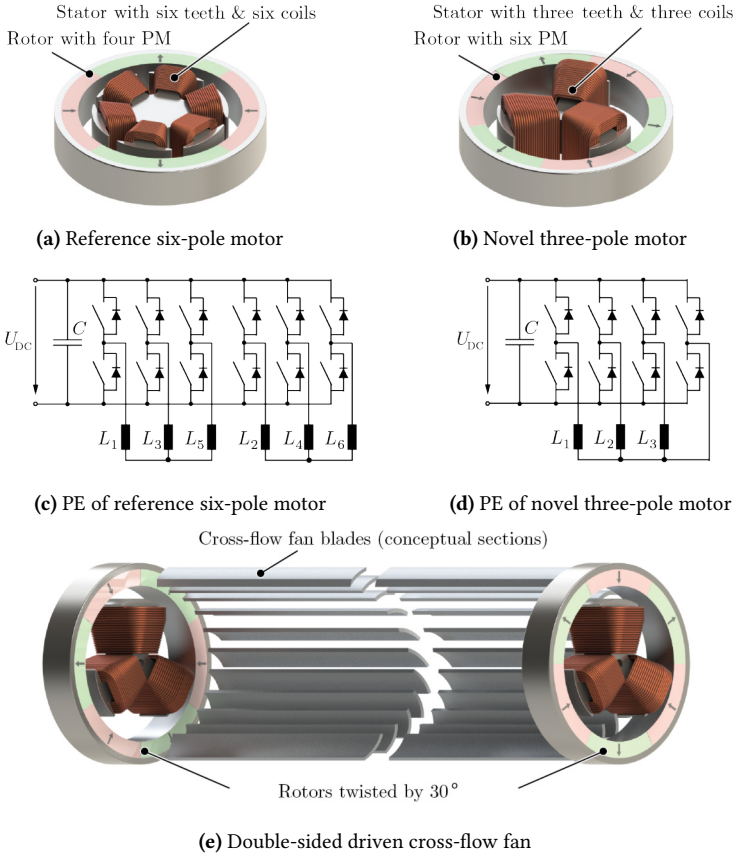
Stator with six teeth & six coils
Rotor with four PM

(a) Reference six-pole motor

Stator with three teeth & three coils
Rotor with six PM

(b) Novel three-pole motor

U_{DC} C L_1 L_3 L_5 L_2 L_4 L_6

(c) PE of reference six-pole motor

U_{DC} C L_1 L_2 L_3

(d) PE of novel three-pole motor

Cross-flow fan blades (conceptual sections)

Rotors twisted by $30°$

(e) Double-sided driven cross-flow fan

Fig. B.1: Conceptual drawing of **(a)** the six-pole reference motor, **(b)** the novel, highly compact three-pole motor, **(c)** the power electronics (PE) of the six-pole reference motor, where six half-bridges are required to control the six coil currents, **(d)** the reduced PE of the novel three-pole motor, where only four half-brides are necessary and **(e)** the bearingless cross-flow fan driven by two $30°$ shifted bearingless three-pole motors as an exemplary application.

active magnetic bearing forces. The influence of stator geometry parameters on the force-torque behavior is embedded in these sections as well. Finally, motor losses are studied in **Sec. B.5**.

B.2 The Three-Pole Bearingless Motor

This chapter aims to introduce a particularly compact and minimalistic novel motor topology. To minimize the motor's dimensions and maximize its power density compared to bearingless motors with separated windings, it is necessary to drastically reduce the number of stator teeth. **Fig. B.2** illustrates the proposed topology where three coils (with combined bearing and drive functionality) are each wound onto one of the three stator teeth, representing the most compact configuration possible.

B.2.1 Passive Bearing

For bearingless slice (or disc-type) motors axial and tilting deflections are passively stabilized. When dislocating the rotor in axial z-direction or tilting it around the x- or y-axis, reluctance forces counteract this movement. The extent to which they react is defined by the axial passive stiffness

$$c_z = \frac{\Delta F_z}{\Delta e_z} \tag{B.1}$$

and two tilting stiffnesses

$$c_\alpha = \frac{\Delta T_\alpha}{\Delta \alpha} \quad \text{and} \quad c_\beta = \frac{\Delta T_\beta}{\Delta \beta}. \tag{B.2}$$

Using the possibility of passive stabilization contributes to designing a highly compact mechatronical system, however, it is physically impossible to stabilize all DOF's purely passively (Earnshaw's theorem [96]).

B.2.2 Active Bearing and Drive

When the rotor is displaced from its center position in radial direction, resulting reluctance forces support this movement until mechanical collision occurs. This destabilizing behavior is described by the radial stiffness factors in x- and y-direction

$$c_x = \frac{\Delta F_x}{\Delta x} \quad \text{and} \quad c_y = \frac{\Delta F_y}{\Delta y}. \tag{B.3}$$
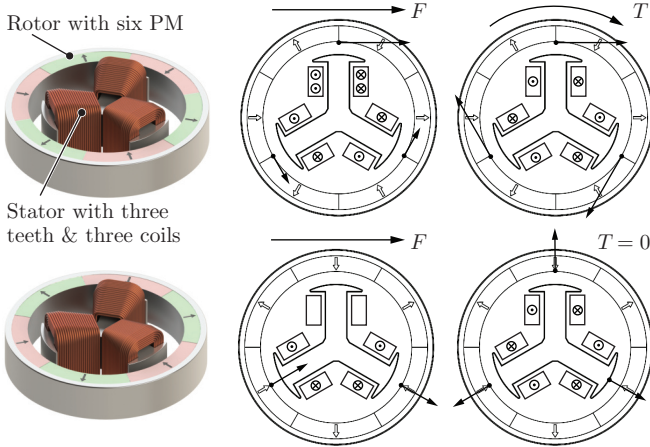
Fig. B.2: Conceptual drawing of the proposed three-pole bearingless motor. The rotor consists of six permanent magnets (PM) that are magnetized in alternating order. The sketches demonstrate its force and torque generation.

The purpose of the active magnetic bearing is to compensate the passive radial bearing stiffness and thereby making rotor levitation possible. The last DOF is the drive torque, which is created by a suitable harmonic wave that generates tangential forces. The harmonic wave is coming from the winding scheme in combination with harmonics from the stator teeth [97]. For the proposed three-pole motor, **Fig. B.2** demonstrates the radial force and torque generation visually. As shown, a bearing force can be arbitrarily created for every rotor angle, i.e., the two radial DOFs are fully stabilized. However, for a certain rotor angle the resulting torque is zero, hence the rotational DOF has not full range.

The necessary power electronics for the active bearing and drive control is depicted in **Fig. B.1 (d)**. Each of the three coils has to be connected to a half-bridge, while the other ends should be connected in star. A forth half-bridge is required to control the star point, since a symmetric star connection is not possible with this design. Employing this control concept, bearing forces can be arbitrarily created for every rotor angle, while the drive experiences single-phase characteristics. For comparison, the power electronics of the reference motor is shown in **Fig. B.1 (c)**, where six half-bridges are required to control the coil currents [35]. It can clearly be seen, that besides the minimalistic
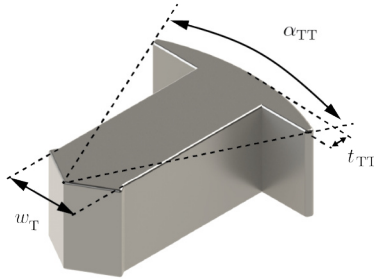
Fig. B.3: Single stator tooth of the three-pole motor with its main geometry parameters, i.e., tooth width w_T, tooth tip opening angle α_{TT} and tooth tip thickness t_{TT}.

stator design of the three-pole motor, the expense for the power electronics is reduced as well.

B.2.3 Coupling Two Three-Pole Motors

This study investigates the challenge of levitating and rotating long shafts by the most compact bearingless motor possible. Therefore, the single-phase drive deficit of the three-pole motor has to be solved. This is realized by a 30° twist between the two motors, which ensures that at no time both motors are in the no-torque position simultaneously. It is demonstrated in **Fig. B.1 (e)** for a cross-flow fan as an example.

B.2.4 Reference Motor

An already existing, fully operational bearingless motor will serve as a reference, which has been presented in [35] in great detail. It consists of six stator teeth, six corresponding copper coils and a rotor with four permanent magnets as visualized in **Fig. B.1 (a)**. This comparison serves to realistically investigate the novel three-pole motor's potential and to increase the success rate of a future prototype. The reference motors specific bearing and drive parameters, derived from 3D magnetostatic FEM simulations, are listed in **Tab. B.1**. For the sake of proper comparison between the reference and novel three-pole motors, some general geometry parameters have to be set as framework conditions. Therefore, the stator and rotor diameters, stator and rotor heights as well as magnet shapes of the proposed motor are set equal to the reference motor.

Using 3D magnetostatic FEM simulations the force-torque behavior of the proposed single as well as coupled three-pole motor will be evaluated next for various stator tooth geometries. Particularly, the influence of different tooth widths w_T, tooth tip opening angles α_{TT} and tooth tip thicknesses t_{TT}, as depicted in **Fig. B.3**, will be studied. The focus lies on delivering maximal torque, reducing cogging torque and generating sufficient bearing forces.

B.3   Drive

This section analyses the motors ability to generate drive torque as well as the topology's cogging torque for different rotor angles. As a first step, the behavior of a single three-pole motor is evaluated from 3D FEM simulations. From this analysis **Fig. B.4** results, which shows the torque for different levels of electrical excitation. The electrical excitation (or magnetomotive force) is represented in ampere-turns (At), since it is the product of applied current and number of windings of a coil. Additionally, simulation results of the reference motor from **Tab. B.1** are plotted in gray for visual comparison. From **Fig. B.4**, different conclusions about the three-pole motor can be drawn. This motor design produces a cogging torque, which will interfere with the active drive torque. The rotor positions marked in red represent stable points in terms of cogging torque. However, these positions coincide with the angles where active drive torque cannot be created. The rotor would stay in this position even if a drive current is applied. The positions marked in blue are unstable points, because any slight angular displacement leads to a cogging torque accelerating the rotor. In summary, this analysis confirms that the three-pole

Tab. B.1: Bearing and drive characteristics of the reference six-pole motor.

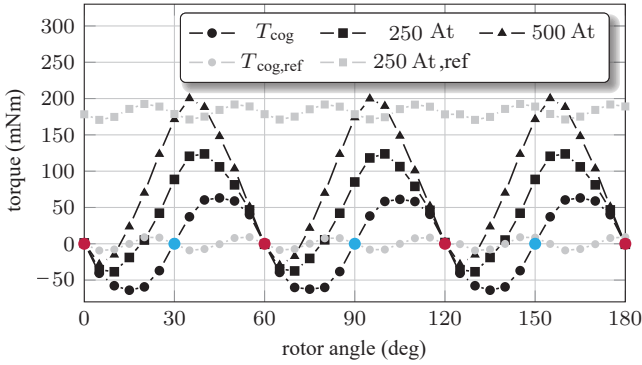| Parameter			
drive torque constant	k_{drv}	0.71	mNm/A
bearing force constant	k_{bng}	35.3	mN/A
radial stiffness	$c_{x,y}$	12.2	N/mm
tilting stiffness	$c_{\alpha,\beta}$	3.2	mNm/deg
axial stiffness	c_z	3.2	N/mm
drive ripple factor for 250 A·turns	γ	4.9	%

Fig. B.4: Cogging torque and active drive torque with respect to rotor angle of the
novel bearingless three-pole motor for excitations of $\hat{\Theta} = 0\,\text{At}$ (corresponding to the
cogging torque T_{cog}), $\hat{\Theta} = 250\,\text{At}$ and $\hat{\Theta} = 500\,\text{At}$. At the points marked in red, a drive
torque cannot be generated. The blue points represent the unstable working points.
Additionally, the cogging torque and drive torque for $\hat{\Theta} = 250\,\text{At}$ of the reference
motor are plotted in gray.

motor experiences single-phase characteristics for the drive and it would not
possible to start the rotation without special measures.

B.3.1 Coupling Two Three-Pole Motors

As described before, for double-sided driven applications the single-phase
drive characteristics of the three-pole motor can be overcome by coupling
them with a 30° shift. **Fig. B.5** depicts the simulation results to that. The
superimposed cogging torque T_{cog} shows to be much lower compared to the
single three-pole motor in **Fig. B.4** and angular positions where no drive
torque can be generated do not exist. Comparing the effective drive torque
that this setup can generate with the reference motor's torque, the simulations
clearly reveal that the coupled three-pole motors create less torque than a
single six-pole reference motor with the same peak magnetomotive force.
This will be addressed in more detail in **Sec. B.5**, when looking at the motor
losses.
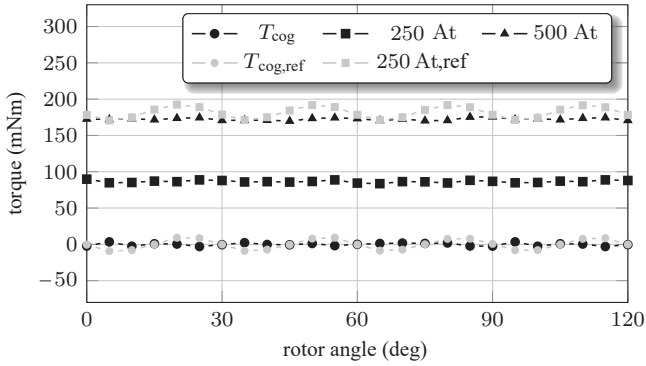
Fig. B.5: Cogging torque and drive torque with respect to rotor angle of two coupled, 30° shifted novel bearingless three-pole motors, including excitations of $\hat{\Theta} = 0$ At (corresponding to the cogging torque T_{cog}), $\hat{\Theta} = 250$ At and $\hat{\Theta} = 500$ At. The no-torque positions are overcome. Additionally, the cogging torque and drive torque for $\hat{\Theta} = 250$ At of the reference motor are plotted in gray.
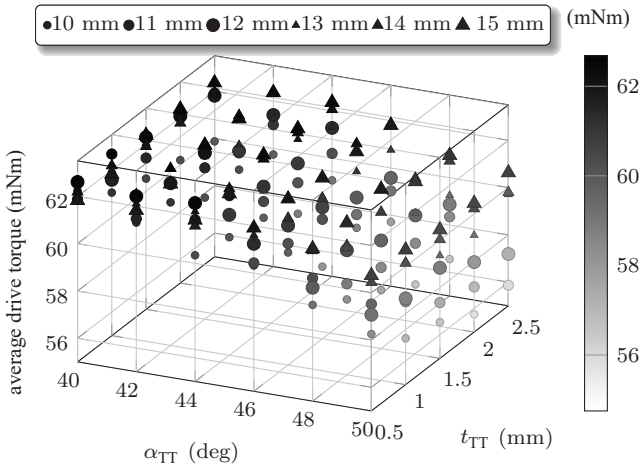

Fig. B.6: Average drive torque for different stator tooth designs, i.e., varying tooth width from $w_T = 10 \ldots 15$ mm, tooth tip opening angle α_{TT} and tooth tip thickness t_{TT} for $\hat{\Theta}_{\text{drv}} = 250$ At.

B.3.2 Stator Design and Optimization

To optimize the coupled three-pole motor for high torque and low torque ripple, simulations have been conducted on the influence of stator tooth geometry (see **Fig. B.3**) on the double-drive's behavior. **Fig. B.6** summarizes the results of the average drive torque that is created with an electrical excitation of $\hat{\Theta}_{drv}$ = 250 At (for each motor), when tooth width w_T and tooth tip form (α_{TT} and t_{TT}) are varied. Torque fluctuations over the angular range have been evaluated from these results as well. Furthermore, **Fig. B.7** shows the simulation results for cogging torque with respect to the different geometry parameters. Finally, the drive ripple factor for a magnetomotive force of $\hat{\Theta}_{drv}$ = 250 At is calculated from these results. After breaking all these simulation results down, different conclusions can be derived about the influence of tooth tip form and tooth width on the torque behavior.

Tooth Tip (α_{TT} & t_{TT})

Interpreting **Fig. B.6**, it can immediately be seen that an increase in tooth tip angle as well as thickness reduces the torque. Therefore, a design without a tooth tip acts in favor of achieving maximal torque. This can be explained by the effect of magnetic saturation. The main part of the permanent magnet flux trajectories tend to shortcut over the tip (instead of passing through the tooth itself) resulting in a torque reduction as explained in [99] in detail. Furthermore, the torque fluctuations have been evaluated. The simulations reveal that the larger the tooth tip, the stronger the fluctuations, i.e., the generated torque varies stronger with angular rotor position. Similarly, the cogging torque increases with larger tooth tip as depicted in **Fig. B.7**. To get an idea on how much the cogging torque affects the drive torque, the ripple factor has been calculated according to

$$\gamma_{drv} = \frac{T_{\hat{\Theta}=0At,max}}{\overline{T}_{\hat{\Theta}=250At}} = \frac{T_{cog,max}}{\overline{T}_{\hat{\Theta}=250At}}, \tag{B.4}$$

with $\overline{T}_{\hat{\Theta}=250\,At}$ being the average torque for an electrical excitation of $\hat{\Theta}_{drv}$ = 250 At and $T_{cog,max}$ the maximal cogging torque. It resulted in a γ_{drv} ranging from 4% (smallest tooth tip) up to 30% (for the largest simulated tooth tip). However, high ripple factors are not desired, since they require special measures within the control structure to ensure a smoothly running rotor. In summary, the drive simulations reveal that no tooth tip is recommended.
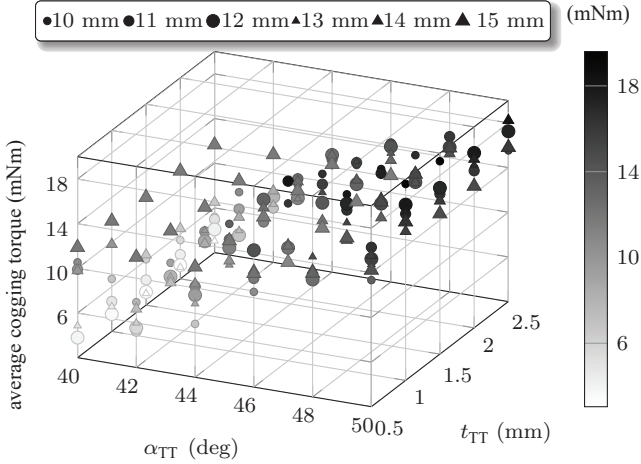
Fig. B.7: Average cogging torque for different stator tooth designs, i.e., varying tooth width from $w_T = 10 \ldots 15$ mm, tooth tip opening angle α_{TT} and tooth tip thickness t_{TT}.

Tooth Width (w_T)

The final, crucial stator parameter is the tooth width. Choosing a small w_T prevents magnetic shortcuts, however, tends to saturation due to the small cross-sectional area which in turn has a negative influence on the resulting torque [99]. A large w_T limits the space for the copper coils and increases the chance of magnetic shortcuts [99]. To analyze these saturation effects briefly, **Fig. B.8** depicts the simulation results for torque generation with respect to tooth width w_T. Tooth designs of $w_T = 6 \ldots 18$ mm without a tooth tip are considered and excitation levels of $\hat{\Theta} = 0$ At, $\hat{\Theta} = 200$ At, $\hat{\Theta} = 300$ At and $\hat{\Theta} = 400$ At are applied. It results that a lower limit of w_T exists at approximately 13 mm (due to magnetic saturation) and that the cogging torque varies over the w_T range with a minimum at 13 mm.

In summary, a stator geometry is preferred, where the tooth has no tooth tip and the tooth tip has the same width as the tooth itself. This design maximizes the effective drive torque and reduces the cogging torque. Regarding the tooth width, it can be concluded that saturation effects have to be taken into account thoroughly in the stator design procedure as is also described in [99].

113
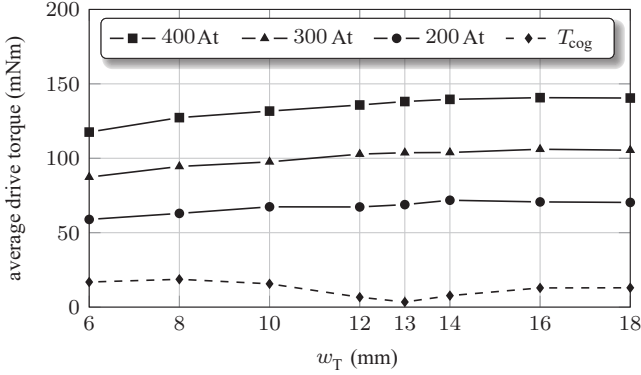
Fig. B.8: Average drive torque for different tooth widths w_T and different electrical
excitation levels of $\hat{\Theta} = 0$ At (corresponding to the cogging torque T_{cog}), $\hat{\Theta} = 200$ At,
$\hat{\Theta} = 300$ At and $\hat{\Theta} = 400$ At.

B.4   Active Magnetic Bearing

After the coupled three-pole motor's drive characteristics have been studied
in great detail, the bearing behavior is next. The passive reluctance forces
heavily depend on the tooth geometry, since for larger stator tooths the area
that the magnetic forces from the permanent magnets can act on, increases.
This section will particularly focus on reluctance forces for different tooth
widths w_T, but excluding stator designs with tooth tips due to the explicit
results from **Sec. B.3**. Moreover, to enable a conclusive comparison of the
active magnetic bearing between the reference motor and the novel three-pole
motor, the radial starting distance δ is compared. The bearing current
needed to start a bearingless motor from standstill (i.e. to detach the rotor from the
wall) is defined as

$$I_{start} = \frac{F_{start}}{k_{bng}} = \frac{c_{x,y} \cdot \delta}{k_{bng}} \tag{B.5}$$

with a required bearing force F_{start} and bearing force constant k_{bng}, whereas
F_{start} is the product of the radial stiffness $c_{x,y}$ and δ. Therefore, δ is defined as

$$\delta = \frac{F_{start}}{c_{x,y}}. \tag{B.6}$$

Fig. B.9 visualizes the simulation results for δ with respect to different
tooth widths $w_T = 6 \ldots 18$ mm, when a magnetomotive force of $\hat{\Theta}_{bng} = 375$

Tab. B.2: Optimal design parameters of the novel three-pole motor and its bearing and drive characteristics.

Parameter			
tooth tip opening angle	α_{TT}	–	deg
tooth tip thickness	t_{TT}	–	mm
tooth width	w_T	13	mm
drive torque constant (coupled)	k_{drv}	0.35	mNm/A
bearing force constant	k_{bng}	26.9	mN/A
radial stiffness	$c_{x,y}$	8.2	N/mm
drive ripple factor for 250 At (coupled)	γ	4.0	%

At is applied. As stated before, the wider the tooth the larger are the passive reluctance forces, hence, the smaller is the radial starting distance that the active bearing can handle for a certain electrical excitation level. This relation is seen in the simulation results in **Fig. B.9** as well. The achievable starting distance depends on the angular position of the rotor, i.e., how does a rotor magnet face the stator tooth. Therefore, **Fig. B.9** not only depicts the average value for the starting distance (δ_{avg}) but also the minimum and maximum possible distances (δ_{min} and δ_{max}), representing the worst and best rotor positions for the active magnetic bearing. Additionally, these three parameters are plotted for the reference motor in gray. The results reveal that for a tooth width of 13 mm, the minimal starting distance δ_{min} coincides with the one of the reference motor. This implies that the three-pole motor's active magnetic bearing, can handle at least the same starting distance (i.e. to detach the rotor from the wall) as the reference motor for the same applied magnetomotive force. This direct comparison is possible, because the stator and rotor diameters have been set equal at the beginning of this study, i.e., have the same split ratio.

To sum up the coupled three-pole motor's investigation, a stator design with $w_T = 13$ mm and no tooth tip offers a high drive torque, rather low cogging torque and bearing forces, that are comparable to the reference motor's active magnetic bearing. The optimal design parameters, bearing and drive characteristics are listed in **Tab. B.2** and its magnetostatic behavior obtained from 3D FEM simulations is depicted in **Fig. B.10**. It should be noted that a brief analysis of the tilting and axial stiffnesses confirmed, that unlike for slice motors, these passive stabilities are not critical for double-sided driven shafts.
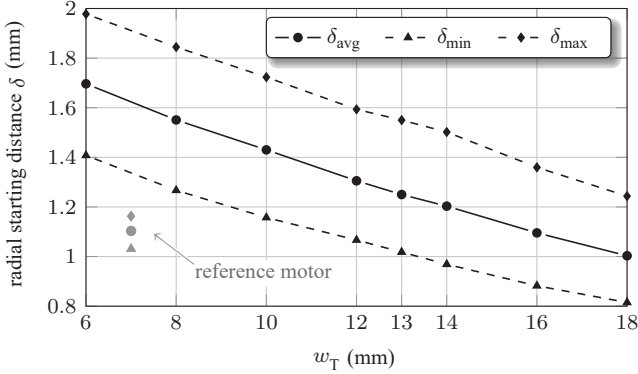
Fig. B.9: Average (δ_{avg}), minimal (δ_{min}) and maximal (δ_{max}) possible starting distances of the novel three-pole motor (depending on rotor's angular position) for an electrical excitation of $\hat{\Theta}_{\text{bng}} = 375\,\text{At}$ with respect to different stator tooth widths w_{T}. Additionally, the average, minimal and maximal starting distances of the reference motor are marked in gray.

B.5 Losses

This section covers a brief comparison of the novel three-pole and the reference motor's losses. This is particularly interesting for the future prototype. Generally, the largest share of the motor losses are the copper and iron losses. The copper losses P_{Cu} are defined as

$$P_{\text{Cu}} = m \cdot R \cdot I_{\text{rms}}^2, \tag{B.7}$$

where m is the tooth number, R the copper resistance and I_{rms} the effective value of the phase current. The resistance of the copper coils can further be calculated as

$$R = \rho_{\text{Cu}} \cdot \frac{l_{\text{coil}}}{A_{\text{wdg}}} \approx \rho_{\text{Cu}} \cdot \frac{l_{\text{wdg,avg}} \cdot N_{\text{coil}}^2}{A_{\text{coil}} \cdot k_{\text{coil}}}, \tag{B.8}$$

with the copper resistivity δ_{Cu}, slot filling factor k_{coil}, cross-sectional area of the coil A_{coil}, average winding length $l_{\text{wdg,avg}}$ and number of turns per coil N_{coil}. Furthermore, the phase current can be written as

$$I_{\text{rms}} = \frac{\hat{\Theta}/\sqrt{2}}{N_{\text{coil}}}, \tag{B.9}$$

where $\hat{\Theta}$ represents the magnetomotive force. Finally, plugging (B.8) and (B.9) into (B.7) and assuming the same slot filling factor k_{coil} for the three-pole motor as the reference motor has, following proportionality relation results

$$P_{\text{Cu}} \propto m \cdot \frac{l_{\text{wdg,avg}} \cdot \hat{\Theta}^2}{A_{\text{coil}}}. \tag{B.10}$$

The three-pole motor has a slot number of $m = 3$ (in contrast to the reference motor with $m_{\text{ref}} = 6$), much more space for bigger copper coils A_{coil}, however, a larger magnetomotive force $\hat{\Theta}$ is required to generate the same drive torque.

The stator iron is permeated by an oscillating magnetic field, so the field related hysteresis losses P_{hy} and eddy current losses P_{ed} make up the iron losses. P_{hy} per volume can be characterized as

$$P_{\text{hy}} = f(A_{\text{h}}, \omega), \tag{B.11}$$

where A_{h} represents the area enclosed by the hysteresis curve and ω the angular frequency of the field harmonic [100]. For P_{ed} per volume it holds that

$$P_{\text{ed}} = f(\sigma, B^2, \omega^2), \tag{B.12}$$

with σ being the electric conductivity and B the magnetic flux density [100]. A straight forward iron loss comparison for the three-pole and six-pole reference motor with relations (B.11) and (B.12) is not possible at this point. The motors have different frequencies of the harmonic field, different flux densities due to different stator geometries and the application specific operating point has not been defined yet.

After this brief loss discussion, it can be concluded that an operating point for the target application has to be defined followed by a detailed loss analysis and copper coil design. Only then, a direct comparison of the maximal achievable drive torque between the six-pole and coupled three-pole motors is reasonable.

0 T ▬▬▬▬▬▬▬▬▬ 1.8 T
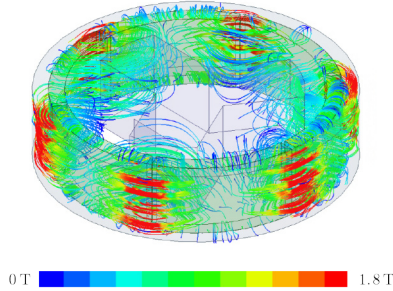
Fig. B.10: Concept of the novel three-pole motor analyzed by 3D magnotostatic FEM simulations.

B.6 Summary

The novel three-pole bearingless motor has been introduced, which is intended for double-sided driven applications. The motor combines an elegantly simple and minimalistic design (hardware-wise), while allowing a rotor operation in chemically challenging, high-purity or extreme temperature environments due to the hermetically-sealed encapsulation of the rotor. By means of 3D magnetostatic FEM simulations, the drive and bearing behavior of two coupled three-pole motors has been investigated. The results reveal that it is theoretically possible to generate drive torque and bearing forces with the novel, coupled bearingless motor topology, however, its ability to generate drive torque is significantly lower compared to the reference motor.

Bibliography

[1] C. A. Mack, "Fifty years of Moore's law," *IEEE Transactions on Semiconductor Manufacturing*, vol. 24, no. 2, pp. 202–207, 2011, DOI: 10.1109/TSM.2010.2096437.

[2] T. Znotins, T. McKee, S. Gutz, K. Tan, and W. Norris, "The design of excimer lasers for use in microlithography," in *Optical/Laser Microlithography*, vol. 922. SPIE, 1988, pp. 454–460, DOI: 10.1117/12.968445.

[3] R. Paetzel, H. S. Albrecht, P. Lokai, W. Zschocke, T. Schmidt, I. Bragin, T. Schroeder, C. Reusch, and S. Spratte, "Excimer lasers for superhigh NA 193 nm lithography," in *Optical Microlithography XVI*, vol. 5040. SPIE, 2003, pp. 1665–1671, DOI: 10.1117/12.485344.

[4] J. Junger and K. Schmidt, "Excimer lasers – Reliability and higher power are key product trends," *Laser Technik Journal*, vol. 4, no. 3, pp. 31–33, 2007, DOI: 10.1002/latj.200790162.

[5] R. Delmdahl and R. Pätzel, "Excimer laser technology trends," *Journal of Physics D: Applied Physics*, vol. 47, no. 3, p. 034004, 2013, DOI: 10.1088/0022-3727/47/3/034004.

[6] P. Das and R. L. Sandstrom, "Advances in excimer laser technology for sub-0.25 μm lithography," *Proceedings of the IEEE*, vol. 90, no. 10, pp. 1637–1652, 2002, DOI: 10.1109/JPROC.2002.803665.

[7] D. Basting and G. Marowsky, *Excimer Laser Technology*. Springer Science & Business Media, 2005.

[8] K. Kakizaki, Y. Sasaki, T. Inoue, and Y. Sakai, "High-repetition-rate (6 kHz) and long-pulse-duration (50 ns) ArF excimer laser for sub-65 nm lithography," *Review of Scientific Instruments*, vol. 77, no. 3, 2006, DOI: 10.1063/1.2182744.

[9] M. Igarashi, H. Miyamoto, M. Katou, H. Tsushima, M. Moriya, A. Kurosu, H. Tanaka, S. Tanaka, T. Ohta, S. Bushida *et al.*, "Imaging performance enhancement by improvements of spectral performance stability and controllability on the cutting-edge," in *Optical Microlithography XXXIII*, vol. 11327. SPIE, 2020, pp. 300–306, DOI: 10.1117/12.2551845.

[10] J. P. Strock, L. Jordan, Y. Minegishi, S. Tanaka, K. Isomoto, T. Asayama, T. Tomonaga, Y. Kawagoe, and Y. Sakou, "The development of a machine learning-based excimer laser performance simulator for engineering maintenance decisions," in *Metrology, Inspection, and Process Control XXXVII*, vol. 12496. SPIE, 2023, pp. 740–753, DOI: 10.1117/12.2658043.

[11] R. L. Sandstrom, R. P. Akins, U. K. Sengupta, C. Reiser, D. G. Larson, and S. L. Anderson, "Krypton fluoride excimer laser for microlithography," in *Optical/Laser Microlithography II*, vol. 1088. SPIE, 1989, pp. 407–415, DOI: 10.1117/12.953169.

[12] J. Ewing, "Excimer laser technology development," *IEEE Journal of Selected Topics in Quantum Electronics*, vol. 6, no. 6, pp. 1061–1071, 2000, DOI: 10.1109/2944.902155.

[13] D. Basting, K. D. Pippert, and U. Stamm, "History and future prospects of excimer lasers," in *2nd International Symposium on Laser Precision Microfabrication*, vol. 4426. SPIE, 2002, pp. 25–34, DOI: 10.1117/12.456812.

[14] A. V. Andramanov, S. A. Kabaev, B. V. Lazhintsev, V. A. Nor-Arevyan, A. V. Pisetskaya, and V. D. Selemir, "Multisectional KrF laser with a pulse repetition rate of 4 kHz and inductive-capacitive discharge stabilisation," *Quantum Electronics*, vol. 36, no. 2, p. 101, 2006, DOI: 10.1070/QE2006v036n02ABEH013109.

[15] H. Mizoguchi, T. Oga, K. Kakizaki, J. Fujimoto, and B. Fechner, *Excimer Lasers for Lithography and Annealing*. Springer, 2021.

[16] V. M. Borisov, A. Y. Vinokhodov, V. A. Vodchits, A. I. Demin, A. V. El'tsov, D. Basting, U. Stamm, and F. Voss, "Compact 600 W KrF laser," *Quantum Electronics*, vol. 28, no. 2, p. 119, 1998, DOI: 10.1070/QE1998v028n02ABEH001148.

[17] V. M. Borisov, A. Y. Vinokhodov, V. A. Vodchits, A. V. El'tsov, and A. S. Ivanov, "Development of high-power KrF lasers with a pulse repetition rate up to 5 kHz," *Quantum Electronics*, vol. 30, no. 9, p. 783, 2000, DOI: 10.1070/QE2000v030n09ABEH001811.

[18] V. M. Borisov, A. V. El'tsov, and O. B. Khristoforov, "High-power, highly stable KrF laser with a 4 kHz pulse repetition rate," *Quantum Electronics*, vol. 45, no. 8, p. 691, 2015, DOI: 10.1070/QE2015v045n08ABEH015658.

[19] H. Tsushima, Y. Fujimaki, Y. Kiyota, M. Tanaka, T. Itou, T. Asayama, A. Kurosu, S. Tanaka, T. Ohta, S. Bushida *et al.*, "Extremely long life excimer laser chamber technology for multi-patterning lithography," in *Optical Microlithography XXXII*, vol. 10961. SPIE, 2019, pp. 201–208, DOI: 10.1117/12.2515667.

[20] H. Tsushima, H. Katsuumi, H. Ikeda, T. Asayama, T. Kumazaki, A. Kurosu, T. Ohta, K. Kakizaki, T. Matsunaga, and H. Mizoguchi, "Extremely long life and low-cost 193 nm excimer laser chamber technology for 450 mm wafer multipatterning lithography," in *Optical Microlithography XXVII*, vol. 9052. SPIE, 2014, pp. 411–418, DOI: 10.1117/12.2046189.

[21] A. Görtler and C. Strowitzki, "Excimer lasers–the powerful light source in the UV and VUV," *Laser Technik Journal*, vol. 2, no. 2, pp. 46–50, 2005, DOI: 10.1002/latj.200790037.

[22] T. Matsunaga, T. Enami, K. Kakizaki, T. Saito, S. Tanaka, H. Nakarai, T. Inoue, and T. Igarashi, "Extremely high-NA high-throughput-scanner-compatible 4 kHz KrF excimer laser for DUV lithography," in *Optical Microlithography XIV*, vol. 4346. SPIE, 2001, pp. 1617–1626, DOI: 10.1117/12.435703.

[23] V. M. Borisov, A. Y. Vinokhodov, V. A. Vodchits, and A. V. El'tsov, "On ultimate pulse repetition rates of an XeF laser," *Quantum Electronics*, vol. 30, no. 10, p. 881, 2000, DOI: 10.1070/QE2000v030n10ABEH001834.

[24] K. Sarkar, R. C. Ujazdowski, P. P. Das, and D. G. Larson, "Excimer laser with magnetic bearings supporting fan," Patent, Dec. 8, 1998, US 5,848,089.

[25] H. Nara, K. Nakao, H. Mizoguchi, T. Nishisaka, and T. Enami, "Once through fan for excimer laser apparatus," Patent, Jan. 8, 2002, US 6,337,872.

[26] H. Fukuyama, K. Toma, and M. Arai, "Excimer laser apparatus," Patent, Mar. 11, 2003, US 6,532,246.

[27] S. Sekiguchi, H. Shinozaki, S. Aiyoshizawa, T. Barada, and A. Ooyama, "Magnetic bearing and circulation fan apparatus," Patent, Feb. 11, 2003, US 6,519,273.

[28] Y. Yada, "Gas circulation fan for excimer laser apparatus," Patent, May 24, 2005, US 6,898,229.

[29] M. Miki and O. Wakabayashi, "Gas laser apparatus and magnetic bearing control method," Patent, Nov. 2, 2021, US 11,162,530.

[30] X. Sun, L. Chen, and Z. Yang, "Overview of bearingless permanent-magnet synchronous motors," *IEEE Transactions on Industrial Electronics*, vol. 60, no. 12, pp. 5528–5538, 2012, DOI: 10.1109/TIE.2012.2232253.

[31] B. Warberger, R. Kaelin, T. Nussbaumer, and J. W. Kolar, "50 Nm/2500 W bearingless motor for high-purity pharmaceutical mixing," *IEEE Transactions on Industrial Electronics*, vol. 59, no. 5, pp. 2236–2247, 2011, DOI: 10.1109/TIE.2011.2161657.

[32] J. Chen, J. Zhu, and E. L. Severson, "Review of bearingless motor technology for significant power applications," *IEEE Transactions on Industry Applications*, vol. 56, no. 2, pp. 1377–1388, 2019, DOI: 10.1109/TIA.2019.2963381.

[33] W. Gruber, W. Bauer, D. Wetsch, B. Wex, and N. Kurita, "Implementation of a bearingless axial-force/torque motor fan with flex-PCB windings," in *IEEE International Electric Machines & Drives Conference (IEMDC)*, 2019, pp. 179–184, DOI: 10.1109/IEMDC.2019.8785266.

[34] M. Osa, T. Masuzawa, K. Yamaguchi, and E. Tatsumi, "Double stator axial gap type ultra-compact 5-DOF controlled self-bearing motor for rotary pediatric ventricular assist device," *IEEE Transactions on Industry Applications*, vol. 57, no. 6, pp. 6744–6753, 2021, DOI: 10.1109/TIA.2021.3105034.

[35] I. Bagaric, D. Steinert, F. Wassmer, T. Holenstein, T. Nussbaumer, and J. W. Kolar, "Design and characterization of a bearingless cross-flow fan," in *IEEE/ASME International Conference on Advanced Intelligent Mechatronics (AIM)*, 2021, pp. 1195–1200, DOI: 10.1109/AIM46487.2021.9517520.

[36] D. Steinert, T. Nussbaumer, and J. W. Kolar, "Slotless bearingless disk drive for high-speed and high-purity applications," *IEEE Transactions on Industrial Electronics*, vol. 61, no. 11, pp. 5974–5986, 2014, DOI: 10.1109/TIE.2014.2311379.

[37] R. Gasch, R. Nordmann, and H. Pfützner, *Rotordynamik*. Springer-Verlag, 2006.

[38] E. H. Maslen, G. Schweitzer, H. Bleuler, and M. Cole, *Magnetic Bearings: Theory, Design, and Application to Rotating Machinery*. Springer, 2009.

[39] A. Toffolo, "On the theoretical link between design parameters and performance in cross-flow fans: A numerical and experimental study," *Computers & Fluids*, vol. 34, no. 1, pp. 49–66, 2005, DOI: 10.1016/j.compfluid.2004.04.002.

[40] A. Toffolo, "On cross-flow fan theoretical performance and efficiency curves: An energy loss analysis on experimental data," *J. Fluids Eng.*, vol. 126, no. 5, pp. 743–751, 2004, DOI: 10.1115/1.1792268.

[41] Y.-C. Shih, H.-C. Hou, and H. Chiang, "On similitude of the cross flow fan in a split-type air-conditioner," *Applied Thermal Engineering*, vol. 28, no. 14-15, pp. 1853–1864, 2008, DOI: 10.1016/j.applthermaleng.2007.11.022.

[42] T. Q. Dang and P. R. Bushnell, "Aerodynamics of cross-flow fans and their application to aircraft propulsion and flow control," *Progress in Aerospace Sciences*, vol. 45, no. 1-3, pp. 1–29, 2009, DOI: 10.1016/j.paerosci.2008.10.002.

[43] Y. Li, H. Ouyang, J. Tian, Z. Du, and Z. Zheng, "Experimental and numerical studies on the discrete noise about the cross-flow fan with block-shifted impellers," *Applied Acoustics*, vol. 71, no. 12, pp. 1142–1155, 2010, DOI: 10.1016/j.apacoust.2010.07.002.

[44] H. Ouyang, J. Tian, Y. Li, Z. Zheng, and Z. Du, "Internal flow and noise investigations about the cross-flow fan with different blade angles," *Journal of Turbomachinery*, vol. 134, no. 5, 2012, DOI: 10.1115/1.4004485.

[45] W. Zhang, J. Yuan, Q. Si, and Y. Fu, "Investigating the in-flow characteristics of multi-operation conditions of cross-flow fan in air conditioning systems," *Processes*, vol. 7, no. 12, p. 959, 2019, DOI: 10.3390/pr7120959.

[46] B. Eck, *Ventilatoren*. Springer, 1972, vol. 5.

[47] L. Lazzarotto, A. Lazzaretto, A. Martegani, and A. Macor, "On cross-flow fan similarity: Effects of casing shape," *J. Fluids Eng.*, vol. 123, no. 3, pp. 523–531, 2001, DOI: 10.1115/1.1379033.

[48] S. Dornstetter, "Numerische und experimentelle Untersuchungen an Querstromventilatoren (in German)," Ph.D. dissertation, 2002.

[49] A. Lazzaretto, "A criterion to define cross-flow fan design parameters," *J. Fluids Eng.*, vol. 125, no. 4, pp. 680–683, 2003, DOI: 10.1115/1.1593709.

[50] I. Bagaric, R. Hu, D. Steinert, T. Nussbaumer, and J. W. Kolar, "Comparative evaluation of high-speed bearingless cross-flow fan designs for lithography excimer lasers," *Machines*, vol. 11, no. 6, p. 611, 2023, DOI: 10.3390/machines11060611.

[51] T. Zou, D. Zhan, X. Hu, S. Hu, and Y. Li, "Experimental and numerical study of cross-flow fan in air-conditioner indoor unit," *International Journal of Refrigeration*, vol. 141, pp. 102–111, 2022, DOI: 10.1016/j.ijrefrig.2022.05.020.

[52] X. Cai, C. Zhang, and B. Wang, "Numerical study on fluid dynamic characteristics of a cross-flow fan," *Journal of Marine Science and Engineering*, vol. 11, no. 4, p. 846, 2023, DOI: 10.3390/jmse11040846.

[53] S. Zheng, B. Han, Y. Wang, and J. Zhou, "Optimization of damping compensation for a flexible rotor system with active magnetic bearing considering gyroscopic effect," *IEEE/ASME Transactions on Mechatronics*, vol. 20, no. 3, pp. 1130–1137, 2014, DOI: 10.1109/TMECH.2014.2344664.

[54] E. Tang, J. Fang, S. Zheng, and D. Jiang, "Active vibration control of the flexible rotor to pass the first bending critical speed in high energy density magnetically suspended motor," *Journal of Engineering for Gas Turbines and Power*, vol. 137, no. 11, p. 112501, 2015, DOI: 10.1115/1.4030264.

[55] E. Tang, B. Han, and Y. Zhang, "Optimum compensator design for the flexible rotor in magnetically suspended motor to pass the first bending critical speed," *IEEE Transactions on Industrial Electronics*, vol. 63, no. 1, pp. 343–354, 2015, DOI: 10.1109/TIE.2015.2472534.

[56] S. Heindel, F. Becker, and S. Rinderknecht, "Unbalance and resonance elimination with active bearings on a Jeffcott rotor," *Mechanical Systems and Signal Processing*, vol. 85, pp. 339–353, 2017, DOI: 10.1016/j.ymssp.2016.08.016.

[57] S. Ran, Y. Hu, and H. Wu, "Design, modeling, and robust control of the flexible rotor to pass the first bending critical speed with active magnetic bearing," *Advances in Mechanical Engineering*, vol. 10, no. 2, p. 1687814018757536, 2018, DOI: 10.1177/1687814018757536.

[58] S. Ran, Y. Hu, H. Wu, and X. Cheng, "Active vibration control of the flexible high-speed rotor with magnetic bearings via phase compensation to pass critical speed," *Journal of Low Frequency Noise, Vibration and Active Control*, vol. 38, no. 2, pp. 633–646, 2019, DOI: 10.1177/1461348418819404.

[59] Y. Zheng, N. Mo, Y. Zhou, and Z. Shi, "Unbalance compensation and automatic balance of active magnetic bearing rotor system by using iterative learning control," *IEEE Access*, vol. 7, pp. 122 613–122 625, 2019, DOI: 10.1109/ACCESS.2019.2938222.

[60] S. K. Kuppa and M. Lal, "Dynamic behaviour analysis of coupled rotor active magnetic bearing system in the supercritical frequency range," *Mechanism and Machine Theory*, vol. 152, p. 103915, 2020, DOI: 10.1016/j.mechmachtheory.2020.103915.

[61] L. Gong and C. Zhu, "Vibration suppression for magnetically levitated high-speed motors based on polarity switching tracking filter and disturbance observer," *IEEE Transactions on Industrial Electronics*, vol. 68, no. 6, pp. 4667–4678, 2020, DOI: 10.1109/TIE.2020.2989710.

[62] P. Cui, L. Du, X. Zhou, J. Li, Y. Li, and Y. Wu, "Harmonic vibration control of MSCMG based on multisynchronous rotating frame transformation," *IEEE Transactions on Industrial Electronics*, vol. 69, no. 2, pp. 1717–1727, 2021, DOI: 10.1109/TIE.2021.3059555.

[63] S. Zheng and C. Wang, "Rotor balancing for magnetically levitated TMPs integrated with vibration self-sensing of magnetic bearings," *IEEE/ASME Transactions on Mechatronics*, vol. 26, no. 6, pp. 3031–3039, 2021, DOI: 10.1109/TMECH.2021.3051372.

[64] G. B. Gallego, L. Rossini, T. Achtnich, D. M. Araujo, and Y. Perriard, "Novel generalized notch filter for harmonic vibration suppression in magnetic bearing systems," *IEEE Transactions on Industry Applications*, vol. 57, no. 6, pp. 6977–6987, 2021, DOI: 10.1109/TIA.2021.3062587.

[65] R. Alcorta, B. Chouvion, and O. Montagnier, "Dynamics of a nonlinear Jeffcott rotor in supercritical regime," *International Journal of Non-Linear Mechanics*, vol. 148, p. 104272, 2023, DOI: 10.1016/j.ijnonlinmec.2022.104272.

[66] H. Xu, J. Li, Y. Lu, and H. Li, "Unbalance control for high-speed active magnetic bearing systems without speed sensors," *IEEE Transactions on Transportation Electrification*, 2024, DOI: 10.1109/TTE.2024.3366551.

[67] J. Li, P. Chen, J. Liu, M. Pan, Q. Chen, and P. Cui, "Dynamic modeling and self-centering effect analysis of magnetically suspended rotor system," *IEEE Sensors Journal*, 2023, DOI: 10.1109/JSEN.2023.3307356.

[68] W. Kliem, C. Pommer, and J. Stoustrup, "Stability of rotor systems: A complex modelling approach," *Zeitschrift für angewandte Mathematik und Physik (ZAMP)*, vol. 49, no. 4, pp. 644–655, 1998, DOI: 10.1007/s000000050113.

[69] T. Baumgartner and J. W. Kolar, "Multivariable state feedback control of a 500 000 r/min self-bearing permanent-magnet motor," *IEEE/ASME Transactions on Mechatronics*, vol. 20, no. 3, pp. 1149–1159, 2014, DOI: 10.1109/TMECH.2014.2323944.

[70] A. Ruggiero, R. D'Amato, E. Magliano, and D. Kozak, "Dynamical simulations of a flexible rotor in cylindrical uncavitated and cavitated lubricated journal bearings," *Lubricants*, vol. 6, no. 2, p. 40, 2018, DOI: 10.3390/lubricants6020040.

[71] M. Hutterer and M. Schroedl, "Stabilization of active magnetic bearing systems in the case of defective sensors," *IEEE/ASME Transactions on Mechatronics*, vol. 27, no. 5, pp. 3672–3682, 2021, DOI: 10.1109/TMECH.2021.3131224.

[72] E. J. Hubmann, F. Weissofner, D. Steinert, T. Nussbaumer, and J. W. Kolar, "Novel acoustic failure prediction method for active magnetic bearing systems," *IEEE/ASME Transactions on Mechatronics*, 2023, DOI: 10.1109/TMECH.2023.3301815.

[73] I. Bagaric, D. Steinert, T. Nussbaumer, and J. W. Kolar, "Supercritical operation of bearingless cross-flow fan," *Machines*, vol. 12, no. 4, p. 223, 2024, DOI: 10.3390/machines12040223.

[74] Y. Hu, K. Yang, H. Wu, X. Guo, and N. Wang, "Critical vibration and control of the maglev high-speed motor based on μ–synthesis control," *Sensors*, vol. 22, no. 22, p. 8692, 2022, DOI: 10.3390/s22228692.

[75] S. Ran, Y. Hu, H. Wu, and X. Cheng, "Resonance vibration control for AMB flexible rotor system based on μ-synthesis controller," *Mathematical Problems in Engineering*, vol. 2018, no. 1, p. 4362101, 2018, DOI: 10.1155/2018/4362101.

[76] P. Wang and C. Zhu, "Active vibration control of a non-collocated AMBs flexible rotor system to pass the first bending critical speed," in *IEEE 22nd International Conference on Electrical Machines and Systems (ICEMS)*, 2019, pp. 1–6, DOI: 10.1109/ICEMS.2019.8922473.

[77] J.-W. Kim, E. Y. Ahn, and H. W. Oh, "Performance prediction of cross-flow fans using mean streamline analysis," *International Journal of Rotating Machinery*, vol. 2005, no. 1, pp. 112–116, 2005, DOI: 10.1155/IJRM.2005.112.

[78] R. M. Himeur, S. Khelladi, M. A. Ait Chikh, H. R. Vanaei, I. Belaidi, and F. Bakir, "Towards an accurate aerodynamic performance analysis methodology of cross-flow fans," *Energies*, vol. 15, no. 14, p. 5134, 2022, DOI: 10.3390/en15145134.

[79] D. Adanta, R. Hindami, A. I. Siswantara *et al.*, "Blade depth investigation on cross-flow turbine by numerical method," in *IEEE 4th International Conference on Science and Technology (ICST)*, 2018, pp. 1–6, DOI: 10.1109/ICSTC.2018.8528291.

[80] D. L. Sampat and M. Govardhan, "Computational studies of flow through cross flow fan: Effect of casing parameters," *International Journal of Fluid Mechanics Research*, vol. 39, no. 1, 2012, DOI: 10.1615/InterJFluidMechRes.v39.i1.40.

[81] J. Li, Y. Hou, J. Liu, Z. Wang, and F. Li, "Window purifying ventilator using a cross-flow fan: Simulation and optimization," in *Building Simulation*, vol. 9. Springer, 2016, pp. 481–488, DOI: 10.1007/s12273-016-0281-8.

[82] A. Ciocănea, A. Marin, and D. L. Burețea, "The influence of housing on the internal flow of a cross flow fan impeller," in *IEEE International Conference on Energy and Environment (CIEM)*, 2019, pp. 464–468, DOI: 10.1109/CIEM46456.2019.8937593.

[83] Y.-C. Shih, S. Tamilarasan, P.-H. Chen, C.-C. Tsao, and C.-H. Lin, "Optimal thermohydraulic design of the indoor unit of a split-type air conditioner," *Applied Thermal Engineering*, vol. 211, p. 118502, 2022, DOI: 10.1016/j.applthermaleng.2022.118502.

[84] K. Sun, H. Ouyang, J. Tian, Y. Wu, and Z. Du, "Experimental and numerical investigations on the eccentric vortex of the cross flow fan,"

International Journal of Refrigeration, vol. 50, pp. 146–155, 2015, DOI: 10.1016/j.ijrefrig.2014.10.005.

[85] Ö. Özer and D. Kumlutaş, "Experimental investigation on cross flow fan's casing parameters inside of a split air conditioner indoor unit by stereo particle image velocimetry," *Applied Thermal Engineering*, vol. 124, pp. 1233–1246, 2017, DOI: 10.1016/j.applthermaleng.2017.06.053.

[86] H. R. Vanaei, S. Khelladi, I. Dobrev, F. Bakir, R. M. Himeur, A. Mammeri, and K. Azzouz, "Performance and efficiency of cross-flow fans – A review," *Energies*, vol. 16, no. 23, p. 7798, 2023, DOI: 10.3390/en16237798.

[87] J. Gan, F. Liu, M. Liu, and K. Wu, "The unsteady fluctuating pressure and velocity in a cross flow fan," *Journal of Thermal Science*, vol. 17, pp. 349–355, 2008, DOI: 10.1007/s11630-008-0349-6.

[88] T. Nussbaumer, P. Karutz, F. Zurcher, and J. W. Kolar, "Magnetically levitated slice motors – An overview," *IEEE Transactions on Industry Applications*, vol. 47, no. 2, pp. 754–766, 2010, DOI: 10.1109/TIA.2010.2102731.

[89] T. Holenstein, T. Nussbaumer, and J. W. Kolar, "A bearingless synchronous reluctance slice motor with rotor flux barriers," in *IEEE International Power Electronics Conference (IPEC – ECCE Asia)*, Niigata, 2018, pp. 3619–3626, DOI: 10.23919/IPEC.2018.8507444.

[90] T. Nussbaumer, K. Raggl, P. Boesch, and J. W. Kolar, "Trends in integration for magnetically levitated pump systems," in *IEEE Power Conversion Conference (PCC)*, Nagoya, 2007, pp. 1551–1558, DOI: 10.1109/PCCON.2007.373170.

[91] G. Jungmayr, E. Marth, M. Panholzer, W. Amrhein, F. Jeske, and M. Reisinger, "Design of a highly reliable fan with magnetic bearings," *Proceedings of the Institution of Mechanical Engineers, Part I: Journal of Systems and Control Engineering*, vol. 230, no. 4, pp. 361–369, 2016, DOI: 10.1177/0959651815602829.

[92] H. Sugimoto, I. Shimura, and A. Chiba, "A novel stator structure for active axial force improvement in a one-axis actively positioned single-drive bearingless motor," *IEEE Transactions on Industry Applications*, vol. 53, no. 5, pp. 4414–4421, 2017, DOI: 10.1109/TIA.2017.2712567.

[93] H. Sugimoto, I. Shimura, and A. Chiba, "Principle and test results of energy-saving effect of a single-drive bearingless motor in cooling fan

applications," *IEEJ Journal of Industry Applications*, vol. 6, no. 6, pp. 456–462, 2017, DOI: 10.1541/ieejjia.6.456.

[94] T. Reichert, T. Nussbaumer, W. Gruber, and J. W. Kolar, "Bearingless permanent-magnet motor with 4/12 slot-pole ratio for bioreactor stirring applications," *IEEE/ASME Transactions on Mechatronics*, vol. 16, no. 3, pp. 431–439, 2011, DOI: 10.1109/TMECH.2011.2122340.

[95] T. Reichert, T. Nussbaumer, and J. W. Kolar, "Bearingless 300 W PMSM for bioreactor mixing," *IEEE Transactions on Industrial Electronics*, vol. 59, no. 3, pp. 1376–1388, 2011, DOI: 10.1109/TIE.2011.2126532.

[96] S. Earnshaw, "On the nature of the molecular forces which regulate the constitution of the luminiferous ether," *Transactions of the Cambridge Philosophical Society*, vol. 7, p. 97, 1848.

[97] F. Zürcher, T. Nussbaumer, and J. W. Kolar, "Principles of magnetic levitation force and motor torque generation by superposition of harmonics in bearingless brushless motors," in *35th Annual Conference of IEEE Industrial Electronics (IECON)*, 2009, pp. 1246–1251, DOI: 10.1109/IECON.2009.5414638.

[98] S.-M. Yang and M.-S. Huang, "Design and implementation of a magnetically levitated single-axis controlled axial blood pump," *IEEE Transactions on Industrial Electronics*, vol. 56, no. 6, pp. 2213–2219, 2009, DOI: 10.1109/TIE.2009.2017095.

[99] P. Karutz, T. Nussbaumer, W. Gruber, and J. W. Kolar, "Saturation effects in high acceleration bearingless motors," in *IEEE International Symposium on Industrial Electronics (ISIE)*, 2008, pp. 472–477, DOI: 10.1109/ISIE.2008.4676990.

[100] H. Mitterhofer and W. Amrhein, "Design aspects and test results of a high speed bearingless drive," in *IEEE 9th International Conference on Power Electronics and Drive Systems*, 2011, pp. 705–710, DOI: 10.1109/PEDS.2011.6147329.

Curriculum Vitae

Personal Information

Name	Ivana Bagaric
Date of birth	June 16$^{\text{th}}$, 1995
Nationality	Swiss
Citizen of	Zurich, Switzerland
Contact	bagaric@lem.ee.ethz.ch

Education

2020 – 2024	Doctorate, ETH Zurich
	Power Electronic Systems Laboratory (PES)
2017 – 2020	MSc ETH, ETH Zurich
	Mechanical Engineering
2019 – 2020	Master Thesis, University of California, Santa Barbara
2014 – 2017	BSc ETH, ETH Zurich
	Mechanical Engineering
2010 – 2014	High School, Zurich
	Physics and Applied Mathematics

Work Experience

2020 – 2024	Research Assistant, ETH Zurich
	Power Electronic Systems Laboratory (PES)
2020 – 2020	Internship at Levitronix, Zurich
2018 – 2019	Internship & Working Student at Abbott, Zurich